

Numerical Simulation of Turbulent Flames based on Reaction-Diffusion Manifolds (REDIM) Reduced Chemistry

INSTITUT FÜR TECHNISCHE THERMODYNAMIK

Zur Erlangung des akademischen Grades eines Doktors der
Ingenieurwissenschaften von der KIT-Fakultät für Maschinenbau des Karlsruher
Instituts für Technologie genehmigte Dissertation von
M.Sc. Chunkan Yu

Hauptreferent: Prof. Dr. rer. nat. habil. Ulrich Maas
Korreferent: Prof. Dr.-Ing. Andreas Class

Tag der mündlichen Prüfung: 23.09.2020

Acknowledgments

It would not have been possible for me to accomplish this dissertation without guidance and help from my supervisors, colleagues and family. Accomplishing a PhD dissertation is not an individual experience; rather it takes place in a social context and includes several persons, whom I would like to thank sincerely.

I would like to express my greatest gratitude to my advisor, Prof. Dr. rer. nat. habil. Ulrich Maas, for his input and advices during the time I completed this thesis. His skillful guidance, innovative ideas and patience are greatly appreciated. He has put a tremendous amount of trust in me. His experienced knowledges in combustion and numerical simulation have been a great resource during my PhD time. His constructive comments and warming encouragement help me improving the quality of my work.

I would also like to thank to my co-advisor, Prof. Dr.-Ing. Andreas Class, patiently reading my thesis, asking inspiring questions and assisted me with his great skills. Moreover, he has spent large amount of time after classes to answer my questions. The good advice and support from him has been invaluable on both academic and personal level, for which I am extremely grateful.

I would also like to thank the other faculty members from ITT KIT, particularly PD. Dr. Viatcheslav Bykov and Dr.-Ing. Robert Schiessl, for their general encouragement and discussion. Many thanks to Dr.-Ing. Balasz Pritz from ITS KIT and Dr.-Ing. Gerd Steinhilber for their greatful help in the SPARC and PDF codes. Additionally, I would like to thank Dr. Felipe Minuzzi for valuable discussion and together works on many publications. Moreover, I would like to thank Prof. Dr. rer. nat. Michael Pfitzner and M. Sc. Paola Breda from Universitaet der Bundeswehr Muenchen for invaluable together working and discussion.

This work would no materialized without the financial support by the German Research Foundation (DFG) within the projects DFG/MOST project MA 1205/26, FOR 1993 and SFB/TR 150.

I owe my deepest gratitude to my wife Jie Song, who has been very supportive and helpful and encourage me every step of the way. I would

not have been accomplished this work without her patient support and encouragement.

I would also like to thank my parents for their moral and material assistance.

Abstract

The simulation of reactive flows involves a complex modeling of the interaction of thermodynamics, chemical kinetics, molecular transport and fluid dynamics. In most engineering applications, combustion occurs under turbulent flow conditions, and an understanding of the underlying processes is crucial for the physical description of the phenomenon. Direct numerical simulations (DNS) solve the Navier Stokes equations in a fully resolved way without modeling, leading to a high computational cost. Furthermore, modeling of combustion is a complex phenomenon, since the fuel oxidation mechanisms can have thousands of elementary reactions and hundreds or thousands of chemical species. Turbulence can also enhance the complexity and dimension of the system. Therefore, using detailed kinetic mechanisms is in most cases computationally prohibitive.

Because of the high computational cost using DNS and detailed chemistry, the Probability Density Function (PDF) for the statistical description of turbulence and Reaction-Diffusion Manifolds (REDIM) for the simplification of chemical kinetics are applied in this dissertation. In the PDF method, diffusion processes are modeled by a turbulent mixing model, which is developed without considering the influence of reduced chemistry on it. Although turbulent mixing models in PDF method and methods for chemical reduction are intensively studied and developed separately, their coupling is less intensive investigated. However, coupling of turbulent mixing models and reduced chemical kinetics plays an important role for model prediction, and an over-simplification of coupling between both processes can result in large quantitative and even qualitative errors.

The main contribution of this dissertation is to study the coupling of reduced chemistry with turbulent mixing models. A so-called projection process is used to couple both processes. Different projection strategies are introduced mathematically and investigated according to their physical meanings. The proposed coupling strategies are applied in simulations of the well-known methane/air piloted turbulent non-premixed jet flames, Sandia Flame D - F. While the results for Sandia Flame D and E agree with experiments very well, there are discrepancies for Sandia Flame F due to under-estimation of local extinction. Therefore improvements are suggested and developed.

Kurzfassung

Die Simulation reagierender Strömungen beinhaltet komplexe Wechselwirkungen zwischen Thermodynamik, chemischen Reaktionen, molekularem Transport und Fluidodynamik. Für die meisten technischen Anwendungsbereiche liegen turbulente reagierende Strömungen vor, und ein Verständnis aller zugrundeliegenden Prozesse spielt eine wichtige Rolle für die Beschreibung der zugrundeliegenden Phänomene. Direkte Numerische Simulationen (DNS, engl. „direct numerical simulations“) lösen die Erhaltungsgleichungen für reagierende Strömungen in Raum und Zeit ohne Modellierung der Turbulenz vollständig auf, was höchste Anforderungen an die zur Verfügung stehende Rechenleistung stellt. Zusätzlich erfordert die Modellierung von Verbrennungsprozessen chemische Reaktionsmechanismen mit mehr als tausend Elementarreaktionen und chemischen Spezies. Turbulenz erhöht die Komplexität und die Dimension des Systems, so dass sich anwendungsnahe reagierende Strömungen (z. B. turbulente Verbrennungsprozesse) auch heute nicht unter Verwendung detaillierter Kinetik und direkten numerischen Simulationen simulieren lassen.

Vor diesem Hintergrund erfolgt in der Dissertation die Modellierung turbulenter reagierender Strömungen durch eine statistische Beschreibung der Turbulenz mit Wahrscheinlichkeitsdichtefunktionen (engl. Probability Density Function, PDF) und eine Vereinfachung der chemischen Reaktionen auf Basis von Reaktions-Diffusions-Mannigfaltigkeiten (engl. Reaction-Diffusion Manifolds, REDIM). In der PDF-Methode müssen die Diffusionsprozesse durch ein Mischungsmodell modelliert werden. Obwohl Mischungsmodelle und Methoden für die Modellreduktion für die Chemie bereits untersucht und unabhängig voneinander entwickelt wurden, wurde deren Kopplung bisher nicht umfassend untersucht. Die Koppelung zwischen Mischungsmodellen und reduzierter Chemie spielt jedoch eine zentrale Rolle für die Genauigkeit der Modellierung. Eine nicht optimale Kopplung zwischen beiden Prozessen kann zu erheblichen qualitativen und quantitativen Fehlern führen.

Der Hauptbeitrag der vorliegenden Arbeit ist die Untersuchung der Kopplung zwischen Mischungsmodellen und reduzierter Chemie für turbulente reagierende Strömungen. In der Arbeit wird ein Modell basierend auf einer Projektion der Mischungsmodelle auf die reduzierte Kinetik für die Kop-

plung vorgeschlagen. Unterschiedliche Projektionsstrategien auf Basis von physikalischen Betrachtungen werden motiviert, mathematisch formuliert und untersucht. Die vorgeschlagenen Kopplungsstrategien werden anhand der Modellierung von nicht-vorgemischten pilot-stabilisierten turbulenten Flammen („Sandia Flame D, E und F“) validiert. Der Vergleich der Simulationsergebnisse mit experimentellen Ergebnissen aus der Literatur belegt die Qualität der entwickelten Modelle. Die vorgestellten und validierten Konzepte lassen sich zur Modellierung technisch relevanter Verbrennungsprozesse (Verbrennung in Motoren, Gasturbinen) - aber auch für andere technisch relevante turbulente reagierende Strömungen (chemische Energiespeicherung) verwenden.

Contents

1	Introduction	1
2	Governing Equations for Reacting Flows	7
3	Numerical simulation of turbulent reacting flows	11
3.1	Turbulent flames	11
3.1.1	Phenomenological Description	11
3.1.2	Length scales in turbulent reacting flows	12
3.2	Large Eddy Simulation	16
3.3	Reynolds-averaged Navier Stokes (RANS) Equation model . .	16
3.3.1	Favre-averaging of flow quantities	17
3.3.2	RANS Equation	18
3.3.3	Modeling the Averaged Reynolds stresses	19
3.3.4	Modeling the Averaged Reaction Rate	20
4	Transported-PDF Equation Method	23
4.1	Statistical Definition	24
4.2	Transported-PDF equation	26
4.3	Particle method for the solution of transported-PDF equation	28
4.3.1	Main idea for the particle method	28
4.3.2	Modeling of particle velocity	29
4.3.3	Modeling of particle turbulent frequency	30
4.3.4	Modeling of molecular mixing	31
4.3.5	Evolution of particle thermo-kinetic state due to source	37
5	Model reduction for chemical kinetics	39
5.1	Dynamical behavior of chemical reaction systems	40
5.2	Global Quasi-linearization (GQL) for the model reduction without physical transport	43
5.2.1	Mathematical Model for the Global Quasi-linearization (GQL) Approach	44
5.2.2	Implementation of GQL approach	47
5.2.3	Some comments on GQL implementation	50

CONTENTS

5.2.4	GQL approach for a CH ₄ /Air Auto-Ignition	51
5.2.5	Summary on the GQL approach	53
5.3	Reaction-diffusion manifolds (REDIM) for the model reduction with physical transport	55
5.3.1	REDIM theory and evolution equation	56
5.3.2	Generation of REDIM reduced chemistry	57
5.3.3	Governing equations based on REDIM reduced chemistry	59
5.3.4	Projection process	63
5.3.5	2D REDIM approach for a counterflow diffusion flame CH ₄ -Air system	66
5.3.6	Summary on the REDIM approach	71
6	Hybrid Finite-Volume/ Transported-PDF Method Based on REDIM Reduced Chemistry	73
6.1	Outline of hybrid algorithm	73
6.2	Coupling of reduced chemistry with mixing processes in PDF method	75
6.2.1	Coupling based on projection perpendicular to slow subspaces	77
6.2.2	Coupling based on projection perpendicular to tangen- tial subspace of manifold	79
7	Numerical Implementation of Hybrid Finite-Volume/ Transported- PDF Method Based on REDIM Reduced Chemistry	81
7.1	Finite Volume Method (FVM) for RANS equations	81
7.2	Numerical integration of the system of stochastic particle equa- tions	83
7.2.1	Integration of particle position	83
7.2.2	Integration of particle velocity fluctuation	84
7.2.3	Integration of particle turbulent frequency	85
7.2.4	Integration of particle mixing and reaction	86
7.3	Some numerical issues in the PDF particle method	86
7.3.1	Control of particle number	86
7.3.2	Time-averaging technique	88
7.3.3	Some issues in REDIM storage and application coupled with PDF	88
8	Study of turbulent non-premixed CH₄-air flames	91
8.1	Experimental configuration	91

8.2	Numerical set-up	93
8.2.1	Boundary conditions for the flow field	93
8.2.2	Boundary condition for thermo-kinetic state	95
8.2.3	Computational domain and numerical parameters	96
8.2.4	Progress variables and parametrization coordinates	97
8.2.5	Slow subspaces for CH ₄ combustion system	97
8.3	Simulation of Sandia Flame series based on GRI 3.0 and unity Lewis number assumption for molecular transport	101
8.3.1	Sandia Flame D	107
8.3.2	Sandia Flame E	111
8.3.3	Sandia Flame F	115
8.3.4	Discussion of the simulation results	120
8.4	The influence of different detailed chemical mechanisms	124
8.5	The influence of molecular transport	130
8.6	The influence of dimension of REDIM reduced chemistry	135
9	Conclusion and Outline	139
	Bibliography	141
	List of Acronyms	155

1 Introduction

Combustion processes still play an important role. In practical devices that involve flowing fluids, turbulent flows are more frequently encountered. This is especially true for combustion devices such as internal combustion engines, gas turbines, rocket engines etc [96]. In addition to traditional experimental investigations, numerical methods are increasingly being used today [16, 70]. Modeling and simulation provide an important contribution to the further development of combustion processes, especially of turbulent flows [16, 70].

The simulation of reactive flows involves a broad range of disciplines [16, 70, 96]. The fluid mechanics properties such as velocity, turbulent frequency must be well resolved to describe transport phenomena (e.g. molecular diffusion, convection, turbulent transport) in turbulent flows [70, 72]. Besides the fluid properties, chemical kinetics is also necessary for the numerical simulation to evaluate the consumption rate of reactants and the formation rate of products [16, 70, 104]. Chemical kinetics is a complex subject. At present, the oxidation mechanisms of many fuels such as hydrogen and hydrocarbon can be considered to be reasonably well understood to predict important behaviors such as ignition and burning velocity for a laminar flame [48, 70, 95]. Both fluid mechanics and chemical kinetics are major topics by themselves, and the simulation of turbulent reacting flows couples both topics and therefore increase the complexity significantly, because additional problems concerning interaction between turbulence and chemical kinetics enhances the modeling difficulty [16, 70].

Numerical simulation of turbulent flows can be organized in three groups [70, 72]: Direct Numerical Simulation (DNS), Large Eddy Simulation (LES) and Reynolds-averaged Navier Stokes (RANS) simulations. Direct numerical simulation (DNS) is the most fundamental approach to solve the Navier-Stokes (N-S) equations. It resolves all turbulent length scales with initial and boundary conditions appropriate for the flow considered [70, 72]. Conceptually DNS is the simplest approach without introducing any models. However, its computational cost increases rapidly with increasing Reynolds number, so that its applicability is restricted at low to moderate Reynolds numbers [72]. Due to this limitation of DNS, several techniques for turbulent reacting flows, which involve modelling are developed and their computational requirements

1 INTRODUCTION

are much less than DNS. One technique is Large-eddy simulation (LES) which resolves the relatively large turbulent length scales and the smaller-scale motions are treated by applying models [70, 72]. Another technique is solving Reynolds-averaged Navier Stokes equations (RANS) [70, 72], a technique with acceptable computational cost in which the governing conservation equations are averaged e.g. in time, and closure models are used to deal with turbulence.

Although RANS has a reasonable computational cost and acceptable accuracy, its closure problem is the most challenging part. Its unclosed terms, the so-called averaged Reynolds stresses, lead to modeling problems and a general modeling for this term is still difficult to find [70, 72, 104]. Furthermore, because turbulence and chemistry have a strong interaction, the averaged chemical source term is difficult to be modeled, since it is influenced by turbulent mixing, molecular transport and chemical kinetics [96, 104]. Most of the earlier developed models such as Eddy Break-up (EBU) model [86], Partially Stirred Reactor (PaSR) model [27] and Equilibrium-chemistry-assumption model [104] are based on certain assumptions such as infinite fast reaction rate. Hence, models for average chemical source term in a general way are difficult to find, and these conventional models cannot predict complicated reacting flows with ignition, extinction and problems with slow reactions (e.g. NO_x) or complex chemistry (e.g. soot formation).

The Probability Density Function (PDF) model [73] can overcome the limitations of conventional models for averaged Reynolds stresses and averaged chemical source terms. An important property of the PDF method is that any fluid or thermo-kinetic quantity can be expressed as integrals of the PDF over its sample space and, consequently, their average values and statistical moments of any order can be obtained. Therefore, the averaged Reynolds stresses and chemical source term can be recovered with the help of the PDF [27, 73].

Although the closure problem for the chemical kinetic is resolved by using the PDF method, another problem concerning chemical kinetics arises: Modeling of combustion is a complex phenomenon, since the fuel oxidation mechanisms can have thousands of elementary reactions and hundreds or thousands of chemical species [35, 95]. Therefore, more than hundred governing equations for species must be solved. Furthermore, due to non-linearity of elementary reaction rates, the stiffness of the system of governing equation is typically high, which enormously complicates the numerical integration [35, 57, 95]. In this sense, using detailed kinetic mechanisms is in most cases computationally prohibitive, and techniques for chemical reduction are necessary in order to develop reduced models with less variables and moderate

stiffness [35, 95], while maintaining the accuracy and comprehensiveness of the detailed model.

In [55] it is shown that not the whole composition space is accessed, and the system dynamics is confined to low-dimensional manifolds in composition space, which can be observed from results of direct numerical simulation (DNS). In other words, the original state space can be described by a much smaller number of reduced variables or progress variables. Such low-dimensional manifolds have the advantage that they represent invariant manifolds and represent the overall slow dynamics [35]. There exist many methods for manifold based reduction methods such as Intrinsic Low-Dimensional Manifolds (ILDM) [51], Flame Prolongation ILDM (FPI) [32], Method of Invariant Manifold (MIM) [36], Reaction-Diffusion Manifolds [10], Flamelet-generated Manifolds (FGM) [97], Steady Laminar Flamelet Model (SLFM) [65], Flamelet/progress variable (FPV) [40], etc. Of course there are many other advanced reduction methods such as Directed Relation Graph (DRG) [50] or *In-situ* adaptive tabulation (ISAT) [71] which are based on other ideas. In the present work, the Reaction-Diffusion Manifolds (REDIM) method [10], one of the manifold based reduction methods, is used. Unlike ILDM [51] or MIM [36] which are designed from systems of ordinary differential equations (ODEs), REDIM takes into account both chemical kinetics and physical transport process. REDIM technique has been developed and applied for different cases such as laminar pre-mixed flames [10, 33], steady and transient counterflow diffusion flames [14, 112] and turbulent flames [23, 61, 103].

Although the dimension of the governing equations can be reduced through the use of manifold based simplified chemistry, the reduced description of inhomogeneous reacting flows is complicated by the transport processes (convection, diffusion, mixing processes etc.) and the coupling between reduced chemistry and these transport processes [7, 111, 115]. While coupling of reduced chemistry and physical transport processes have been intensively studied in the laminar case such as in [53, 85, 115], little attempts have been made for the turbulent case, except in [7] which ILDM has been used as an example for manifold based simplified chemistry to investigate the coupling of reduced chemistry with turbulent mixing. They showed that an oversimplification of coupling between both processes can result in large quantitative and even qualitative errors. Hence, it is necessarily to investigate the problem of coupling the simplified chemistry with mixing processes. The main contribution of this work is to study the coupling of manifold based simplified chemistry with mixing processes, in order to answer the following questions:

1 INTRODUCTION

- How does the mixing process affect the manifold based simplified chemistry and vice versa?
- Is it valid to apply mixing models directly to manifold based simplified chemistry?
- If the coupling between both processes is important, how significant is the effect of different coupling strategies on the system and on the results?

Figure 1.1 summarizes this work. This work begins with the FVM part, discussing the Reynolds-averaged Navier-Stokes (RANS) method in Chapter 3. The closure problem in RANS method is overcome by using the Probability Density Function (PDF) method described in Chapter 4. For the solution of the transported-PDF equation, particle method is applied and modeling of particle velocity, turbulent frequency, molecular mixing and evolution of thermo-kinetic state due to source are discussed. In order to reduce the computational cost due to chemical kinetics, model reduction for chemical kinetics is discussed in Chapter 5. Two reduction methods for the chemical kinetics are discussed: the Global Quasi-linearization (GQL) and the Reaction-Diffusion Manifolds (REDIM). The main focus of Chapter 5 involves theory, numerical implementation, and their application for CH_4 as example. In Chapter 6 a hybrid algorithm which is a combination of a Finite-Volume Method (FVM), PDF method, and REDIM as reduced chemistry is discussed. The most important novelty of this work concerns the coupling strategies between manifold based simplified chemistry and mixing processes in PDF method in Section 6.2. Afterwards, in Chapter 7 the numerical implementation for the whole hybrid algorithm is discussed. Finally, the whole proposed algorithm is tested for a well-known turbulent non-premixed CH_4 -air flames, Sandia Flame D - F.

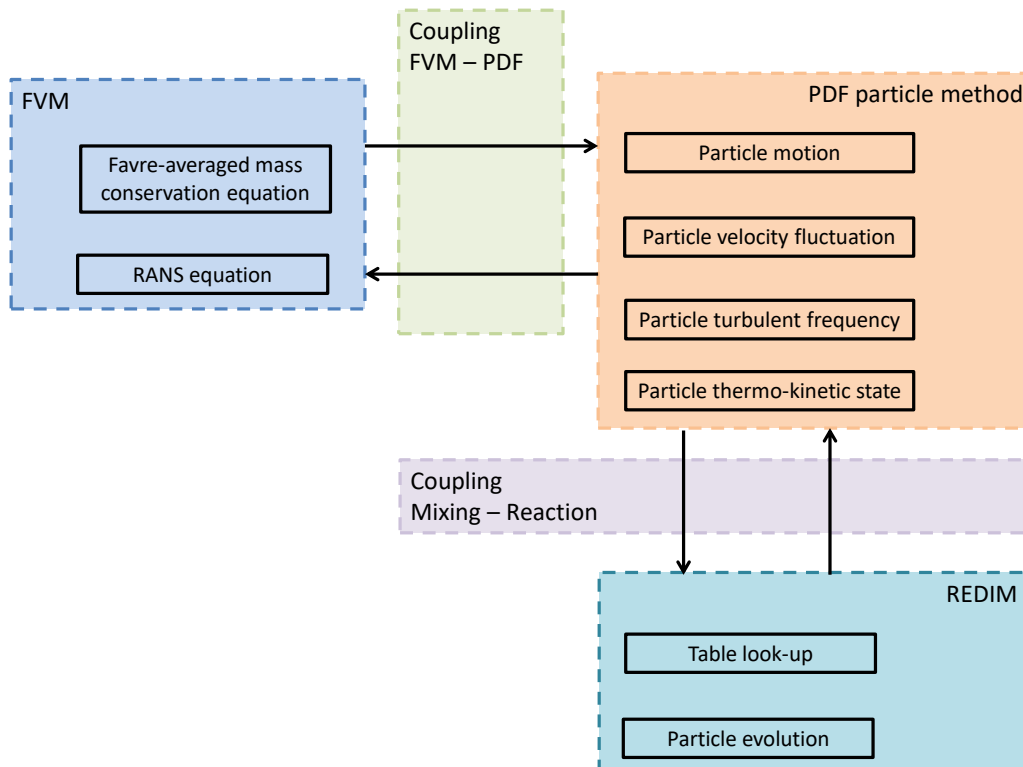


Figure 1.1: Schematic summary of numerical algorithm.

2 Governing Equations for Reacting Flows

Combustion processes involve a broad range of phenomena such as transport processes (e.g. convection process, molecular diffusion process) and chemical reaction. In order to understand the combustion process of reacting flows, all involved processes must be taken into consideration. A mathematical description in terms of conservation equations for mass, momentum, species and energy allows to study the combustion process in time and space [16, 27, 70, 104]. These equations describe the hydrodynamic and thermodynamic relationships among state variables (e.g. species concentration, enthalpy) and physical variables (e.g. pressure, density, velocity). The mass conservation equation relates the density and velocity. The momentum conservation equation relates the velocity and pressure. The species conservation equation describes the evolution of each species due to transport processes and chemical reaction. And the energy conservation equation relates internal energy and kinetic energy of the flow. The governing conservation equations are expressed in terms of partial differential equation (PDE) as (a full derivation for these governing equations can be found in e.g. [70, 104]):

Mass conservation equation:

$$\frac{\partial \rho}{\partial t} + \frac{\partial \rho u_j}{\partial x_j} = 0, \quad (2.1)$$

Momentum conservation equation:

$$\frac{\partial \rho u_i}{\partial t} + \frac{\partial}{\partial x_j} (\rho u_i u_j + p \cdot \delta_{ij}) = \frac{\partial \tau_{ij}}{\partial x_j} + \rho g_i, \quad (2.2)$$

Species conservation equation:

$$\frac{\partial \rho w_k}{\partial t} + \frac{\partial}{\partial x_j} (\rho u_j w_k) = \frac{\partial}{\partial x_j} \left(\rho D_k \frac{\partial w_k}{\partial x_j} \right) + M_k \cdot \dot{\omega}_k, \quad (2.3)$$

Energy conservation equation:

$$\frac{\partial \rho h}{\partial t} + \frac{\partial \rho u_j h}{\partial x_j} = \frac{\partial \rho p}{\partial t} + \frac{\partial \rho u_j p}{\partial x_j} + \tau_{ij} \cdot \frac{\partial u_j}{\partial x_i} + \frac{\partial}{\partial x_j} \left(\rho D_e \frac{\partial h}{\partial x_j} \right) + \dot{q}_s. \quad (2.4)$$

2 GOVERNING EQUATIONS FOR REACTING FLOWS

For index, $i = 1, 2, 3$, $j = 1, 2, 3$ and $k = 1, 2, \dots, n_{sp}$. And the Einstein summation convention is applied for notational brevity.

In these equations, n_{sp} is the number of involving species, t the time, ρ the mixture density, p the pressure, h the mixture specific enthalpy and \dot{q}_s the energy source. $\mathbf{u} = (u_1, u_2, u_3)^T$ is the flow velocity. g_i the gravitational acceleration in i -th direction. For k -th species, w_k is its mass fraction, M_k its molar mass, D_k its diffusion transport coefficient and D_e its heat transfer coefficient.

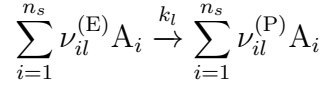
τ_{ij} is the stress tensor which is symmetric ($\tau_{ij} = \tau_{ji}$) and is defined as:

$$\tau_{ij} = 2\mu \left(S_{ij} - \frac{1}{3} \frac{\partial u_k}{\partial x_k} \delta_{ij} \right), \quad (2.5)$$

where μ is the dynamic viscosity and S_{ij} the strain rate tensor:

$$S_{ij} = \frac{1}{2} \left(\frac{\partial u_i}{\partial x_j} + \frac{\partial u_j}{\partial x_i} \right). \quad (2.6)$$

The term $\dot{\omega}$ in Eq.2.3 is the reaction rate. If the chemical mechanism consists of $i = 1, 2, \dots, n_{sp}$ chemical species written as A_1, A_2, \dots, A_{n_s} participating in $l = 1, 2, \dots, n_r$ elementary chemical reactions, then the l -th chemical reaction with stoichiometric coefficients of educts $\nu_{il}^{(E)}$ and of products $\nu_{il}^{(P)}$ can be represented symbolically as:



where k_l is the rate coefficient of the l -th reaction. According to the rate law describing an empirical formulation of the reaction rate, the rate of chemical species j in the l -th elementary reaction reads [104]:

$$\left(\frac{\partial c_j}{\partial t} \right)_l = k_l \left(\nu_{jl}^{(P)} - \nu_{jl}^{(E)} \right) \prod_{i=1}^{n_s} c_i^{\nu_{il}^{(E)}}, \quad (2.7)$$

where c_j is the concentration of chemical species j . Therefore the molar rate for the formation $\dot{\omega}_i$ of a chemical species i describes the sum of formation rates of all n_r reactions, which reads:

$$\dot{\omega}_i = \sum_{l=1}^{n_r} \left(\frac{\partial c_j}{\partial t} \right)_l = \sum_{l=1}^{n_r} k_l \left(\nu_{il}^{(P)} - \nu_{il}^{(E)} \right) \prod_{i=1}^{n_s} c_i^{\nu_{il}^{(E)}}. \quad (2.8)$$

The rate coefficient k_l depends strongly on the temperatures, which can be described by Arrhenius formulation [104]:

$$k_l = A_l \left(\frac{T}{\text{K}} \right)^{\beta_l} \cdot \exp \left(-\frac{E_{al}}{RT} \right). \quad (2.9)$$

where A_l is the pre-exponential factor, β_l the temperature-exponent and E_{al} the activation energy. For each elementary reaction, there exists a backward elementary reaction with rate coefficient k_l^b which is determined from the rate coefficient of forward elementary reaction k_l^f and the equilibrium constant $K_{C,l}$ as[104]:

$$\frac{k_l^f}{k_l^b} = K_{C,l} \quad (2.10)$$

and the equilibrium constant $K_{C,l}$ is determined through the change of free enthalpy of the l -th reaction [104]:

$$K_{C,l} = \left(\frac{P_{\text{atm}}}{RT} \right)^{\sum_i^{n_s} \nu_{jl}^{(P)} - \nu_{ji}^{(E)}} \exp \left(-\frac{\Delta G_l^0}{RT} \right) \quad (2.11)$$

where ΔG_l^0 is the change of free enthalpy under 1 atm, P_{atm} the atmospheric pressure and R the gas constant.

However, there are $(6 + k)$ -unknown parameters (density, enthalpy, pressure, 3 velocities and k species concentrations), which are determined by $(5 + k)$ -governing conservation equations (Eq.2.1, 2.2, 2.3, 2.4). Therefore, one needs additionally the ideal gas law:

$$p = \rho R_g T, \quad (2.12)$$

with the specific gas constant R_g of the mixture.

In this work, the species concentration will be quantified in terms of specific mole numbers $\phi_k = w_k/M_k$ ¹. Furthermore, if one introduces a $(n = 2 + n_{sp})$ -dimensional state vector:

$$\Psi = (h, p, \phi_1, \phi_2, \dots, \phi_{n_{sp}})^T, \quad (2.13)$$

the conservation equations for the thermo-kinetic scalars (Eq. 2.3 and 2.4) can be re-written in vector notation in a general form:

$$\frac{\partial \Psi}{\partial t} = \mathbf{S}(\Psi) - \mathbf{u} \cdot \text{grad}(\Psi) + \frac{1}{\rho} \text{div}(\mathbf{D} \cdot \text{grad}(\Psi)). \quad (2.14)$$

¹The definition $\phi_k = w_k/M_k = x_k/M_{\text{mean}}$, where x_k is the molar fraction and M_{mean} the mean molar mass. This representation has an advantage due to reasonable scale in the results.

2 GOVERNING EQUATIONS FOR REACTING FLOWS

Here, \mathbf{S} is the n -dimensional thermo-chemical source term. \mathbf{D} is the $n \times n$ -dimensional quadratic transport matrix including molecular transport and heat transfer.

3 Numerical simulation of turbulent reacting flows

The governing conservation equations for mass Eq.2.1, momentum Eq.2.2 and thermo-kinetic state Eq.2.14 in Chapter 2 are generally applicable for any reacting flows. Numerical simulations solving these governing equations directly, the so-called Direct Numerical Simulations (DNS), provides the most accurate results, because it does not require any additional closure equations (as in the case of the RANS and LES methods) [70, 72]¹. However, the accurate results using DNS come at the expense of an enormous computational effort [70, 72] due to structure of turbulent flows, which will be discussed in Sec.3.1. The Reynolds-averaged Navier-Stokes (RANS) model reduces computational cost largely compared to DNS. In Sec.3.3 RANS method is outlined and its resulted closure problem will be discussed.

3.1 Turbulent flames

3.1.1 Phenomenological Description

The most important non-dimensional parameter characterizing the tendency of a flow to become turbulent is the Reynolds number, which describes the ratio of inertial forces to viscous forces in the flow [72]:

$$Re = \frac{\rho u L}{\mu}, \quad (3.1)$$

where ρ is the flow density, u the characteristic flow velocity, L the characteristic length and μ the dynamic viscosity. If the Reynolds number of a flow is low, it means that the viscous forces are sufficiently large such that disturbances in the flows are damped and hence the flow is stable and

¹The direct numerical simulation is, as a matter of fact, also a model. The accuracy of DNS results largely depends on the applied numerical techniques such as time advancement or spatial discretization. Usually, the DNS method requires very fine grids and extremely small time steps, in order to obtain accurate solutions [70, 72].

keeps laminar. However, flows can become turbulent if Reynolds number is large, because damping is not strong enough to render flow in a stable way. Furthermore, turbulence of a flow will be promoted by large Reynolds number because of the cascade phenomenon of turbulent flows [72]: a large amount of kinetic energy is required to generate large eddies. However, these large eddies are unstable and break up, transferring their energy to smaller eddies. These eddies undergo a similar break-up processes, and transfer their energy to even smaller eddies, until Reynolds number is sufficiently small so that the eddy motion is small and viscous is effective in dissipating the kinetic energy.

Such complex behavior (energy cascade) in turbulent flows results in a high computational effort using DNS, since the smallest length scales (size of smallest eddies) must be considered to retain high resolution. And this smallest length scales become smaller with increasing Reynolds number (see Sec.3.1.2).

3.1.2 Length scales in turbulent reacting flows

Length scales related to turbulence

As mentioned in Sec.3.1.1, the energy cascade phenomenon - in which energy is transferred to successively smaller and smaller eddies until molecular viscosity is effective in dissipating kinetic energy - leads to the fact that a turbulent flow consists of a wide range of length scales of eddies. The eddy size varies in a range from largest eddies of size l_0 (called integral length scales, comparable to the macro-scale of flows) to the smallest eddies of size l_K (called Kolmogorov scale) [70, 72]. Based on both length scales (l_0 and l_K) and the velocity fluctuation u' as characteristic velocity, one can define the corresponding Reynolds number in turbulent flow [72]:

$$\text{Turbulent Reynolds number: } Re_{l_0} = \frac{\rho u' l_0}{\mu}, \quad (3.2)$$

$$\text{Kolmogorov Reynolds number: } Re_{l_K} = \frac{\rho u' l_K}{\mu}. \quad (3.3)$$

As derived in [27, 72], the ratio of the smallest to largest length scales can be approximated as:

$$\frac{l_K}{l_0} \sim Re_{l_0}^{-3/4} \quad (3.4)$$

This equation (together with Fig.3.1) shows that at high Reynolds number, the smallest eddies with size l_K are much smaller than those of largest eddies with size l_0 .

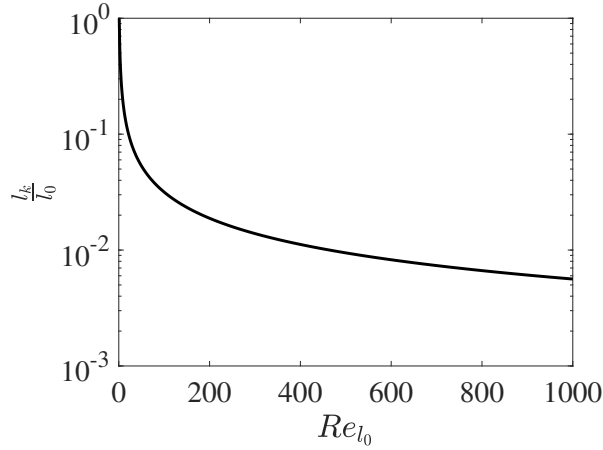


Figure 3.1: Ratio of the smallest to largest length scales over turbulent Reynolds number Re_{l_0} .

Due to wide range of turbulence length scales, the DNS must ensure that [70, 72]:

- The computational domain must be large enough to resolve the macroscopic scale of flows (e.g. diameter of pipe);
- The mesh size must be fine enough such that the smallest length scales (typically the Kolmogorov length scale l_K) can be resolved.

In the following, the computational cost using DNS is discussed based on both requirements, showing that for turbulent reacting flows DNS costs extremely high computational effort.

Suppose a computational domain with size L in one direction and number of mesh grid N , one has then the grid size $\Delta x = L/N$. The computational domain must be at least of the order of largest eddy size l_0 : $L \geq l_0$ [70, 72]. Furthermore, the grid size must be smaller than the smallest eddy size in turbulence: $\Delta x \leq l_K$ [70, 72]. Therefore, one obtains the minimal required grid number (together with Eq.3.4):

$$\frac{l_0}{l_K} \leq N, \text{ and thus: } N \geq Re_{l_0}^{3/4} \quad (3.5)$$

in one direction. Accordingly, the minimal total grid number for a three-dimensional (3D) simulation is:

$$N_{\text{total}} = N^3 \geq Re_{l_0}^{9/4}. \quad (3.6)$$

3 NUMERICAL SIMULATION OF TURBULENT REACTING FLOWS

It is observed clearly from Fig.3.2 that with increasing Reynolds number, the required minimum total grid number increases significantly. For a turbine, the order of magnitude of the Reynolds number can vary from $\mathbf{O}(10^4)$ to $\mathbf{O}(10^5)$ [3, 58], corresponding to the required minimum grid number in order of magnitude from $\mathbf{O}(10^9)$ to $\mathbf{O}(10^{11})$, which exceeds the capacity of the most powerful high performance computer currently available.

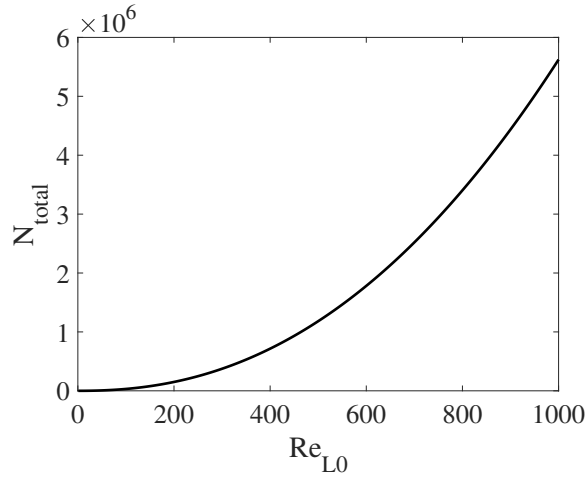


Figure 3.2: Estimated minimal total grid number for a 3D DNS with turbulent Reynolds number Re_{l_0} .

Length scales related to flames

In non-premixed flames, not only the length scales related to the turbulence such as Kolmogorov length scale must be considered, two important other length scales related to flames must be identified as shown in Fig.3.3, which makes the numerical simulation more difficult:

- δ_d denotes the diffusion thickness; This is the layer for diffusion process that fuel and oxidizer diffuse towards each other and mix with each other. The grid size must be sufficient small to describe this diffusion layer so that diffusion process can be appropriately described.
- δ_r denotes the reaction zone thickness, in which reaction can take place and temperature increases rapidly, and is usually $\delta_r \ll \delta_d$. The grid size must be sufficient small so that the reaction zone can also be well numerically calculated.

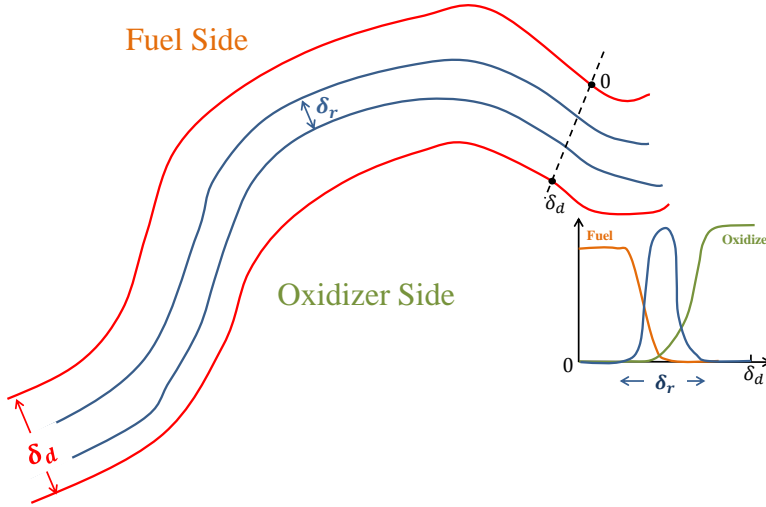


Figure 3.3: Schematic illustration of length scales in non-premixed flame.

As analytically discussed in [70], in flows with high Reynolds number, the diffusion thickness is controlled by the Kolmogorov length scales:

$$\delta_d \approx l_K \gg \delta_r. \quad (3.7)$$

Therefore, the computational demand using DNS is further increased in the presence of chemical reaction, since flame reaction zones are much smaller than the Kolmogorov length scales [70]. For such situations, resolutions finer than those mentioned in Eq.3.6 are required.

To summarize, due to high computational requirements using DNS, it is still not applicable to most practical engineering simulations, and some compromises in resolution must be made. One of the alternative, the Reynolds-averaged Navier Stokes (RANS) Equation model, will be discussed in the following section 3.3. However, the RANS approach has its limitation that the solution is a statistical mean and not sufficient to capture highly transient phenomena or detailed structures of the turbulent flows [70, 72].

Large Eddy Simulation (LES), in which the turbulent large scales are explicitly calculated whereas the effects of small scales are modeled by using subgrid models [70, 72], is a compromise between RANS and DNS. LES has attracted significant interest in recent years and has been intensively applied for turbulent combustion simulation such as in [67, 68, 76, 84, 103, 113].

3.2 Large Eddy Simulation

In order to reduce the computational cost, in the LES the smallest length scales are ignored via low-pass filtering of the Navier-Stokes equation [72]. A low-pass LES filter is applied to any quantity $q(\mathbf{x})$ in the flow field and perform a spatial filtering operation. Those structures with spectral frequencies larger than a cut-off filter are modeled [70, 72]. By apply the LES filter $\mathcal{G}(\mathbf{x} - \mathbf{x}')$, variable q becomes [70, 72]:

$$\bar{q}(\mathbf{x}) = \int g(\mathbf{x}') \cdot \mathcal{G}(\mathbf{x} - \mathbf{x}') d\mathbf{x}', \quad (3.8)$$

where $\mathcal{G}(\mathbf{x} - \mathbf{x}')$ corresponds to the process of averaging over a box, evaluated from the computational cell size $\Delta = \sqrt[3]{V_{\text{cell}}}$.

Then a mass-weighted Favre filtering is applied on the quantity $q(\mathbf{x})$ as [70]:

$$\tilde{q} = \frac{\bar{\rho} \cdot \bar{q}}{\bar{\rho}}. \quad (3.9)$$

With this, the filtered transported equations can be formulated [72], and the unclosed subgrid stresses can be modeled using e.g. Smagorinsky-Lilly model or Germano dynamic model [70, 72]. More details about the theory and implementation of LES can be found in e.g. [70, 72].

Although LES can describe turbulent structures accurately with low computational cost compared to the DNS, the LES also has its drawbacks such as the requirement of 3D computational domain and relative high computational costs compared to the RANS, which will be discussed in the following.

3.3 Reynolds-averaged Navier Stokes (RANS) Equation model

Although DNS provides the most detailed information about the turbulent reacting flows, due to its prohibitive computational cost it is still not feasible to most practical engineering simulations [16, 70]. Furthermore, in most cases, engineers are interested only in averaged quantities of the turbulent reacting flow [16, 96]. Therefore, such a detailed information available from DNS is of less interest for practical reason. In a Reynolds-averaged Navier-Stokes (RANS) simulations all governing conservation equations are solved for averages of turbulent flow quantities. RANS simulation, compared to DNS, has noticeable advantages that its computational cost is much lower and it has less requirement on computational grid size and geometry [70, 72].

3.3 REYNOLDS-AVERAGED NAVIER STOKES (RANS) EQUATION MODEL

In this part, the RANS method is outlined, and its resulted closure problem will be discussed.

3.3.1 Favre-averaging of flow quantities

In turbulent flows, if instabilities are not sufficiently damped by viscosity, flow quantities such as velocity, temperature and species concentrations at each point in the flow exhibits random fluctuations, which is illustrated in Fig.3.4 as a typical example, which shows the random unsteadiness of one quantity q in a turbulent flow. One useful way to characterize a turbulent flow is to define averaged and fluctuating quantities. An averaged quantity is defined by taking a time-average of this quantity in the flow over a sufficiently large time interval (e.g. $\Delta t = t_2 - t_1$) [96, 104]:

$$\overline{q(\mathbf{x})} = \frac{1}{\Delta t} \int_{t_1}^{t_2} q(\mathbf{x}, t) dt, \quad (3.10)$$

where $q(\mathbf{x}, t)$ is any flow quantities such as velocity, temperature and species concentrations at one point. Once the averaged value is defined, we can split the instantaneous quantity $q(\mathbf{x}, t)$ into its averaged value $\overline{q(\mathbf{x})}$ and fluctuation $q'(\mathbf{x}, t)$, which is referred to as the Reynolds decomposition [72]:

$$q(\mathbf{x}, t) = \overline{q(\mathbf{x})} + q'(\mathbf{x}, t), \quad (3.11)$$

with the property that $\overline{q'(\mathbf{x}, t)} = 0$. Figure 3.4 illustrates the fluctuation component $q'(\mathbf{x}, t)$ at a specific time t_0 .

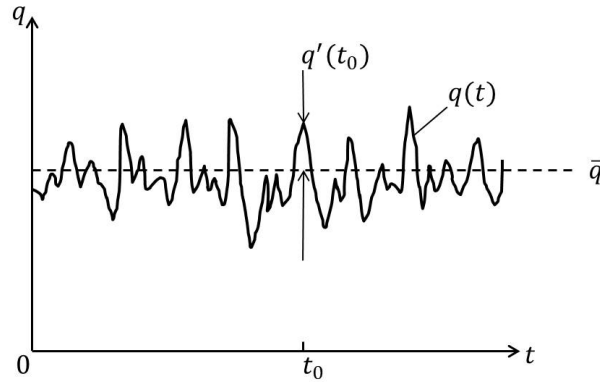


Figure 3.4: Quantity as a function of time at a fixed point in a turbulent flow.

For turbulent reacting flows, since density changes significantly, it is convenient to introduce a density-weighted average $\tilde{q}(\mathbf{x})$, which is called the

3 NUMERICAL SIMULATION OF TURBULENT REACTING FLOWS

Favre-average, such that all quantities except the pressure are density weighted [70, 104]:

$$\tilde{q}(\mathbf{x}) = \frac{\overline{\rho \cdot q(\mathbf{x}, t)}}{\bar{\rho}}. \quad (3.12)$$

Thus, similar to Reynolds averaging, a quantity $a(\vec{x}, t)$ is split into a Favre-averaged quantity $\tilde{q}(\mathbf{x})$ and the corresponding Favre fluctuation $q''(\mathbf{x}, t)$:

$$q(\mathbf{x}, t) = \frac{\overline{\rho \cdot q(\mathbf{x}, t)}}{\bar{\rho}} + q''(\mathbf{x}, t) = \tilde{q}(\mathbf{x}) + q''(\mathbf{x}, t), \quad (3.13)$$

3.3.2 RANS Equation

Based on favre-averaging the governing conservation equations Eq.2.1 - 2.4 can be formulated into [70, 72, 104]:

Favre-averaged mass conservation equation:

$$\frac{\partial \bar{\rho}}{\partial t} + \frac{\partial \bar{\rho} \tilde{u}_j}{\partial x_j} = 0 \quad (3.14)$$

Favre-averaged momentum conservation equation:

$$\frac{\partial \bar{\rho} \tilde{u}_i}{\partial t} + \frac{\partial}{\partial x_j} (\bar{\rho} \tilde{u}_i \tilde{u}_j + \bar{p} \cdot \delta_{ij}) = \frac{\partial}{\partial x_j} (\bar{\tau}_{ij} - \overline{\rho u_i'' u_j''}) \quad (3.15)$$

Favre-averaged species conservation equation:

$$\frac{\partial \bar{\rho} \tilde{w}_k}{\partial t} + \frac{\partial}{\partial x_j} (\bar{\rho} \tilde{u}_j \tilde{w}_k) = \frac{\partial}{\partial x_j} \left(\bar{\rho} D_k \frac{\partial \tilde{w}_k}{\partial x_j} \right) + \bar{\rho} \tilde{\omega}_k - \frac{\partial}{\partial x_j} (\overline{\rho u_j'' w_k''}) \quad (3.16)$$

These governing equations are time-averaged, and hence the obtained quantities are also time averaged. In statistically stationary turbulent flows,

3.3 REYNOLDS-AVERAGED NAVIER STOKES (RANS) EQUATION MODEL

the time derivative term disappears from the equation and averaged quantities do not change with time [72, 108]²:

$$\begin{aligned}\frac{\partial \bar{\rho}}{\partial t} &= 0 \\ \frac{\partial \bar{\rho} \tilde{u}_i}{\partial t} &= 0 \\ \frac{\partial \bar{\rho} \tilde{w}_k}{\partial t} &= 0\end{aligned}\tag{3.17}$$

We notice that the averaged Reynolds stresses, $\widetilde{\bar{\rho} u_i'' u_j''}$ in Eq.3.15 and $\widetilde{\bar{\rho} u_j'' w_k''}$ in Eq.3.16, and the averaged reaction rate, $\tilde{\omega}_k$ in Eq.3.16, are unknown *a priori*. Therefore, the number of unknowns, consequently, is more than the number of equations. This constitutes the closure problem in RANS modeling, which means a sufficient number of equations for the unknown terms has to be established.

3.3.3 Modeling the Averaged Reynolds stresses

Many models for the averaged Reynolds stress have been developed during the last decades. The most popular modeling approach is the so-called turbulent viscosity model given by [72]:

$$\widetilde{\bar{\rho} u_i'' u_j''} = -2\mu_T \left(\tilde{S}_{ij} - \frac{1}{3} \frac{\partial \tilde{u}_k}{\partial x_k} \right) + \frac{2}{3} \bar{\rho} k \delta_{ij}\tag{3.18}$$

with μ_T as turbulent viscosity and k as the specific turbulent kinetic energy defined by:

$$k = \frac{1}{2} \widetilde{u_i'' u_j''}\tag{3.19}$$

and \tilde{S}_{ij} the mean strain rate tensor:

$$\tilde{S}_{ij} = \frac{1}{2} \left(\frac{\partial \tilde{u}_i}{\partial x_j} + \frac{\partial \tilde{u}_j}{\partial x_i} \right)\tag{3.20}$$

In analogy to the term for velocity, unclosed term for species mass fractions can also be modelled using this gradient approach as [70, 104]

$$\widetilde{\bar{\rho} u_i'' w_k''} = -\mu_T \frac{\partial \tilde{w}_k''}{\partial x_i}\tag{3.21}$$

²Note that if the unsteadiness behavior is deterministic, then the governing unsteady RANS is suitable. However, a small time step is required to capture unsteady development of the turbulent flow.

Given the turbulent viscosity μ_T , Eq.3.18 and 3.21 provide a convenient and simple closure for the averaged Reynolds stresses. The remaining task is to provide an expression for μ_T . Mostly, there are three groups for the determination of μ_T [72, 104]. The first group solves the μ_T by using an algebraic or zero-equation model. Example of this model is the Prandtl's mixing length model, which relates μ_T with mixing length [72]. The second group solves the μ_T by using an one-equation model. The turbulent-kinetic-energy model is one candidate for this group, which solves a transport equation for turbulent kinetic energy k for the determination of μ_T [72]. The third group solves the μ_T by using a two-equation model, in which the $k - \epsilon$ or $k - \omega$ models are two prime candidates. In the $k - \epsilon$ model, for example, one transport model for turbulent kinetic energy k and one transport model for turbulent dissipation ϵ must be solved. And μ_T is expressed in terms of k and ϵ [16, 70, 72, 104].

As discussed, the averaged Reynolds stresses are modeled related to the mean value gradient [70, 72], which has been validated for many cases. However, it was found in homogeneous shear flow that the direction of the scalar flux is significantly different than that of the mean gradient. For example, such model is not valid in a general way for turbulent premixed flames, in which the countergradient transport may occur [94].

3.3.4 Modeling the Averaged Reaction Rate

The most critical closure problem arises from modeling the averaged reaction rate $\tilde{\omega}$, since it is highly non-linear [104]:

$$\widetilde{\dot{\omega}(\Psi)} \neq \dot{\omega}(\tilde{\Psi}) \quad (3.22)$$

This inequality is attributed to two facts: non-linearity due to species concentrations and non-linearity due to the highly strong temperature-dependence of the rate coefficient (c.f. Eq. 2.7 and 2.9). Over the last decades, several simple algebraic closure modeling for $\tilde{\omega}$ have been developed due to their low computational cost.

One simple but popular modeling for $\tilde{\omega}$ is the Eddy Break-up (EBU) approach [86]. The underlying idea is that the chemistry is fast and therefore averaged reaction rate is governed by the rate at which turbulent mixing processes can bring reactants and products together. In the RANS method, the rate of mixing processes is taken to be inversely proportional to the turbulent time-scale $\tilde{k}/\tilde{\epsilon}$, leading to a reaction rate model of the form [86]:

$$\tilde{\omega} = C_{\text{EBU}} \cdot \frac{\tilde{\epsilon}}{\tilde{k}} \cdot \tilde{\rho} \tilde{c}'' c'' \quad (3.23)$$

3.3 REYNOLDS-AVERAGED NAVIER STOKES (RANS) EQUATION MODEL

where c is the progress variable describing the chemical reaction and c'' the progress variable variance used as a measurement of the scalar fluctuation magnitude. Despite of the simple expression for modeling the averaged reaction rate in EBU model, it has some disadvantages like producing unphysical solutions to walls or a reasonable value of constant C_{EBU} for each individual case [88].

Of course there are many other models such as Eddy Dissipation Concept (EDC), $k - \epsilon - g$ model [87] and Equilibrium-chemistry-assumption model [104] that are developed for specific application cases, most of them are based on certain assumptions such as infinite fast reaction rate. Hence these models have some fundamental drawbacks such as deficient in predicting complicated reacting flows with ignition, extinction and problems with slow reactions such as NOx chemistry [16, 38, 70]. A more general way to model the averaged reaction rate is based on the Probability Density Function (PDF) method, which is the main topic of the next chapter.

4 Transported-PDF Equation Method

The RANS method discussed in Sec.3.3 uses models for the unclosed averaged Reynolds stresses and averaged chemical source term which are mostly not universal [70, 72]. Especially concerning the models for the averaged chemical source term, most models are based on the assumption of e.g. fast chemistry, where the flames thickness is below the turbulent length scales [16, 70, 96]. Such an assumption makes the prediction of extinction, ignition and slow chemistry effect more difficult. Therefore, it is necessary to develop some methods that can model both unclosed terms in a more universal way.

Recall that in a turbulent flow, quantities $q(\mathbf{x}, t)$ such as velocity, temperature and species concentrations are random. Such randomness in the flow field is attributed to unavoidable perturbations in initial conditions and boundary conditions [72]. And its chaotic behavior is due to sensitivity to such perturbations¹ [72]. Therefore, values of random quantity $q(\mathbf{x}, t)$ in turbulent flows are inherently unpredictable. In order to characterize a random quantity, the concept of *Probability Density Function* (PDF) is an useful tool, describing the probability for this random variable to take on a given value (precise definition see Sec.4.1).

To illustrate this point, a schematic presentation of statistical description for fuel mass fraction as an example in turbulent reacting flows is shown in Fig.4.1. The fuel jet flows into ambient, which is at rest, and flame front forms after fuel and air are mixed and ignited. If we measure mass fractions of fuel at two different locations where one is near the center-line of round jet and the other one is near the flame front, we observe that the probability density functions of fuel mass fractions are different from each other. However, if we know the PDF at each position, it is convenient for us to calculate the averaged values or higher order moments [27, 38, 72, 73].

¹Note that such perturbations are also present in laminar flows. However, in turbulent flows the evolution of flow field is extremely sensitive to small changes in initial conditions and boundary conditions.

4 TRANSPORTED-PDF EQUATION METHOD

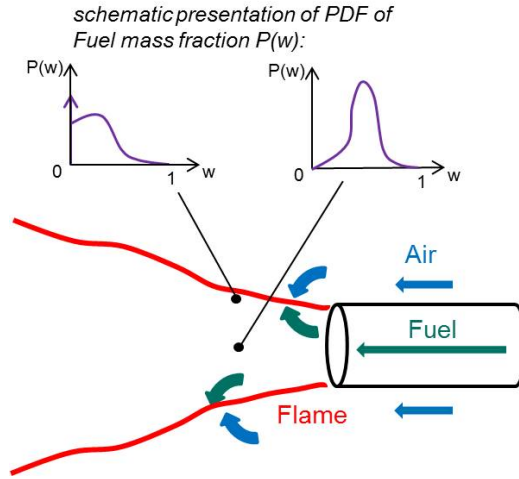


Figure 4.1: Schematic presentation of probability concept for fuel mass fraction $P(w)$.

In this chapter, Sec.4.1 firstly reviews important statistic definitions in probability theory . Then transported-PDF equation method is discussed with the primary motivation to obtain the PDF in a general way in Sec.4.2. The particle method for the solution of transported-PDF equation with corresponding models is outlined in Sec.4.3

4.1 Statistical Definition

For a given point in space \mathbf{x} and a given time t , the random velocity field $\mathbf{V}(\mathbf{x}, t)$, the thermo-kinetic scalar field $\Phi(\mathbf{x}, t)$ and the turbulent frequency $\Theta(\mathbf{x}, t)$ can be characterized by a one-point joint probability density function (PDF) $f_{\mathbf{u}\Psi\omega}(\mathbf{V}, \Phi, \Theta; \mathbf{x}, t)$ defined by [72]:

$$\begin{aligned} & f_{\mathbf{u}\Psi\omega}(\mathbf{V}, \Phi, \Theta; \mathbf{x}, t) d\mathbf{V} d\Phi d\Theta \\ & = P\{\mathbf{V} \leq \mathbf{u}(\mathbf{x}, t) \leq \mathbf{V} + d\mathbf{V}, \Phi \leq \Psi \leq \Phi + d\Phi, \Theta \leq \omega \leq \Theta + d\Theta\}. \end{aligned} \quad (4.1)$$

Here \mathbf{V}, Φ, Θ are the sample-space variables of velocity, thermo-kinetic scalar and turbulent frequency corresponding to \mathbf{u}, Ψ, ω . This PDF contains all one-point statistical information about the velocity, thermo-kinetic scalar and turbulent frequency at all locations \mathbf{x} and time t . For any PDF the following conditions are satisfied [72]:

$$f_{\mathbf{u}\Psi\omega}(\mathbf{V}, \Phi, \Theta; \mathbf{x}, t) \geq 0, \quad (4.2)$$

4.1 STATISTICAL DEFINITION

$$\int_{-\infty}^{+\infty} \int_{-\infty}^{+\infty} \int_{-\infty}^{+\infty} f_{\mathbf{u}\Psi\omega}(\mathbf{V}, \Phi, \Theta; \mathbf{x}, t) d\mathbf{V} d\Phi d\Theta = 1. \quad (4.3)$$

Given $f_{\mathbf{u}\Psi\omega}(\mathbf{V}, \Phi, \Theta; \mathbf{x}, t)$, if $q(\mathbf{u}, \Psi, \omega; \mathbf{x}, t)$ is a function of any random quantity in flows (e.g. velocity, temperature, thermo-kinetic scalar), its averaged value can be obtained by:

$$\overline{q(\mathbf{x}, t)} = \int_{-\infty}^{+\infty} \int_{-\infty}^{+\infty} \int_{-\infty}^{+\infty} q(\mathbf{V}, \Phi, \Theta; \mathbf{x}, t) \cdot f_{\mathbf{u}\Psi\omega}(\mathbf{V}, \Phi, \Theta; \mathbf{x}, t) d\mathbf{V} d\Phi d\Theta \quad (4.4)$$

When dealing with reacting flows where density changes, it is more often to use the favre-averaged PDF formulated as:

$$\tilde{f}_{\mathbf{u}\Psi\omega}(\mathbf{V}, \Phi, \Theta; \mathbf{x}, t) = \frac{\rho(\Psi; \mathbf{x}, t)}{\overline{\rho(\Psi; \mathbf{x})}} \cdot f_{\mathbf{u}\Psi\omega}(\mathbf{V}, \Phi, \Theta; \mathbf{x}, t). \quad (4.5)$$

And the favre-averaged quantity is given by:

$$\widetilde{q(\mathbf{x}, t)} = \int_{-\infty}^{+\infty} \int_{-\infty}^{+\infty} \int_{-\infty}^{+\infty} q(\mathbf{V}, \Phi, \Theta; \mathbf{x}, t) \tilde{f}_{\mathbf{u}\Psi\omega}(\mathbf{V}, \Phi, \Theta; \mathbf{x}, t) d\mathbf{V} d\Phi d\Theta. \quad (4.6)$$

Besides that, the conditional expectations play an important role in the PDF methods. A conditional PDF expressed as [72, 73]:

$$f_{\mathbf{u}\omega|\Psi}(\mathbf{V}, \Theta|\Phi) d\mathbf{V} d\Theta \quad (4.7)$$

has the significance of probability that \mathbf{u} and ω is in the infinitesimal range $\mathbf{V} \leq \mathbf{u}(\mathbf{x}, t) \leq \mathbf{V} + d\mathbf{V}$ and $\Theta \leq \omega \leq \Theta + d\Theta$, given that Ψ is equal to Φ ($\Psi = \Phi$). The conditional PDF $f_{\mathbf{u}\omega|\Psi}$ is the derivative of the conditional distribution function with respect to \mathbf{V} and Θ [73]:

$$f_{\mathbf{u}\omega|\Psi}(\mathbf{V}, \Theta|\Phi) = \frac{f_{\mathbf{u}\Psi\omega}(\mathbf{V}, \Phi, \Theta)}{f_{\Psi}(\Phi)}. \quad (4.8)$$

If, again, $q(\mathbf{u}, \Psi, \omega; \mathbf{x}, t)$ is a function of any random quantity in flows as in Eq.4.4, the conditional expectation of q , given $\Psi = \Phi$, is defined by [72, 73]:

$$\overline{q(\mathbf{u}, \omega, \Psi)|\Psi = \Phi} = \int_{-\infty}^{+\infty} f_{\mathbf{u}\omega|\Psi}(\mathbf{V}, \Theta|\Phi) \cdot q(\mathbf{V}, \Phi, \Theta) d\mathbf{V} d\Theta. \quad (4.9)$$

4.2 Transported-PDF equation

The primary motivation for obtaining the probability density function (PDF) is that any one-point statistical moment such as average, variance and covariance can be recovered [73]. This is especially important and advantageous that the averaged Reynolds stresses and averaged chemical source terms can be obtained in a statistical way, without any modeling [38, 73]. For example, if one knows the one-point velocity-composition-frequency PDF given by $\tilde{f}_{\mathbf{u}\Psi\omega}(\mathbf{V}, \Phi, \Theta; \mathbf{x}, t)$, the unclosed averaged Reynolds stresses and source term for α -th thermo-kinetic scalar (\widetilde{S}_α) can also be determined by using the PDF according to definition in Sec.4.1.:

$$\widetilde{u_i'' u_j''} = \int_{-\infty}^{+\infty} \int_{-\infty}^{+\infty} \int_{-\infty}^{+\infty} (V_i - \bar{u}_i) \cdot (V_j - \bar{u}_j) \cdot \tilde{f}_{\mathbf{u}\Psi\omega}(\mathbf{V}, \Phi, \Theta) d\mathbf{V} d\Phi d\Theta. \quad (4.10)$$

$$\widetilde{S}_\alpha = \int_{-\infty}^{+\infty} \int_{-\infty}^{+\infty} \int_{-\infty}^{+\infty} S_\alpha(\Phi) \cdot \tilde{f}_{\mathbf{u}\Psi\omega}(\mathbf{V}, \Phi, \Theta) d\mathbf{V} d\Phi d\Theta. \quad (4.11)$$

We observe that the closure problem that arises from averaging high nonlinear terms is solved and hence no modeling is needed. Especially for averaged source term, any arbitrarily complex chemical mechanism can be solved in an exact way. However, generally the PDF of a flow is *a priori* unknown. A possible approach to determine the PDF is the so-called presumed-PDF approach, supposing that the PDF has a fixed shape which can be parametrized with only one or two parameters (e.g. β -function) [27]. Furthermore, when more than one variable is needed, it is assumed that thermo-kinetic scalars are supposed to be statistically independent to split the joint PDF as a product of single variable PDFs [27, 38]: $\tilde{f}(\Psi_1, \Psi_2, \dots, \Psi_n) \approx \tilde{f}(\Psi_1) \cdot \tilde{f}(\Psi_2) \cdot \dots \cdot \tilde{f}(\Psi_n)$. However, such assumption is not physically valid, because thermo-kinetic states are closely related in flames and, accordingly, are not statistically independent [27, 38].

A more general way is to solve the so called transported-PDF equation to obtain the instantaneous PDF $\tilde{f}_{\mathbf{u}\Psi\omega}(\mathbf{V}, \Phi, \Theta; \mathbf{x}, t)$ at every position in flow field. In this approach, an exact PDF evolution can be obtained by solving a transport equation for PDF derived from the Navier-Stokes Eq.2.2 and scalar

4.2 TRANSPORTED-PDF EQUATION

conservation equation Eq.2.14. Following the derivation in e.g. [27, 38, 72, 73], the transported-PDF equation for $\tilde{f}_{\mathbf{u}\Psi\omega}(\mathbf{V}, \Phi, \Theta; \mathbf{x}, t)$ is given by^{2 3}:

$$\begin{aligned}
 \frac{\partial \bar{\rho} \tilde{f}}{\partial t} &+ \frac{\partial \bar{\rho} V_i \tilde{f}}{\partial x_i} - \overline{\left(\frac{\partial \bar{\tau}_{ij}}{\partial x_j} + \frac{\partial \bar{p}}{\partial x_i} \right) \frac{\partial \tilde{f}}{\partial V_i}} + \frac{\partial \bar{\rho} S_\alpha \tilde{f}}{\partial \Phi_\alpha} \\
 &= - \frac{\partial}{\partial V_i} \left\{ \overline{\left(\frac{\partial \tau'_{ij}}{\partial x_j} - \frac{\partial p'}{\partial x_i} \right) \Big|_{\Theta, \mathbf{V}, \Phi}} \cdot \tilde{f} \right\} \\
 &+ \frac{\partial}{\partial \Phi_\alpha} \left\{ \overline{\left(\frac{\partial}{\partial x_j} (D_\alpha \rho \frac{\partial \phi_\alpha}{\partial x_j}) \right) \Big|_{\Theta, \mathbf{V}, \Phi}} \cdot \tilde{f} \right\} \\
 &- \frac{\partial}{\partial \Theta} \left\{ \overline{\left(\frac{D\omega}{Dt} \right) \Big|_{\Theta, \mathbf{V}, \Phi}} \cdot \tilde{f} \right\}, \tag{4.12}
 \end{aligned}$$

where $\mathbf{x} = (x_1, x_2, x_3)^T$ is the spatial position and t the time. \bar{p} is the averaged pressure and p' the pressure fluctuation. S_α denotes the source term of α -th thermo-kinetic scalar. D/Dt denotes the material derivative, $\bar{\tau}_{ij}$ the averaged viscous stress, \bar{p} the mean pressure and ρ the density.

In this transported-PDF equation, terms treated exactly appear on the left-hand side, and conditional terms which must be modeled appear on the right-hand side. The most important observation in Eq.4.12 is that the thermo-kinetic source term appears in a closed form because of the relation:

$$S_\alpha(\Psi) = \overline{(S(\Phi) | \Phi = \Psi)}. \tag{4.13}$$

Accordingly, the transported-PDF equation is able to handle any complex chemical kinetics (e.g. NOx slow chemistry or soot formation) in an exact way.

²the subscripts and arguments to the PDF have been dropped for brevity.

³There are also other PDF models such as velocity-composition PDF and velocity-composition-dissipation-rate PDF [38, 72, 73]. In a transported-PDF equation for velocity-composition PDF, turbulent frequency is not carried as flow property. Then turbulent time-scale information must be specified externally [72]. Various PDFs provide different statistical description of the flow quantities considered. However, for some flows, an over-complete description may provide little benefit [72].

4.3 Particle method for the solution of transported-PDF equation

The transported-PDF equation for joint velocity - turbulent frequency - composition PDF $\tilde{f}_{\mathbf{u}\Psi\omega}(\mathbf{V}, \Phi, \Theta; \mathbf{x}, t)$ (Eq.4.12) is an integral-differential equation in up to $n + 8$ independent variables (n thermo-kinetic state variables in Ψ , 3 spatial coordinates, 3 velocity components, turbulent frequency and time). The high dimensionality of transported-PDF equation leads to the numerical solution based on conventional methods such as finite difference, finite volume or finite element methods impracticable [27, 38, 72, 73].

Alternatively, the Monte-Carlo particle method was suggested to solve the transported-PDF equation [73]. In the Monte-Carlo particle method, a system of notional particles with flow and thermo-kinetic properties is considered obey the underlying governing conservation equations [72, 73]. Thus, the PDF is represented by an ensemble of stochastic particles evolving according to stochastic processes that are described by stochastic differential equations (SDEs). In this way, numerical integration for SDEs instead of for original transported-PDF equation is more efficient, and the computational cost using Monte-Carlo particle method increases only linearly with the dimensionality of the sample space [27, 38, 73].

In this section, the main idea for particle methods will be briefly outlined. Then the particle methods for solving Eq.4.12 will be discussed. The implementation of numerical integration will be given later in Sec.7.2.

4.3.1 Main idea for the particle method

In transported-PDF method, the evolution of PDF f_L of fluid particles is of key interest, since it describes the underlying physical phenomenon [72]. The main idea of the Monte-Carlo particle method is to devise stochastic processes, such that the corresponding modeled transported-PDF f_L^* evolves in a similar manner as the real flow PDF f_L [27, 72, 73]. A detailed investigation and derivation of modeling for stochastic processes can be found in [72, 73]. In the following, the key concept is briefly outlined. Although it is explained through velocity $\mathbf{u} = (u_1, u_2, u_3)^T$ as example, it can be also extended to other quantities such as turbulent frequency or thermo-kinetic states.

Recall that u_i is one velocity component in $\mathbf{u} = (u_1, u_2, u_3)^T$ and $\mathbf{V} = (V_1, V_2, V_3)^T$ its sample space variable. A stochastic process is defined in term of a system of SDEs [72]:

$$du_i = a_i(\mathbf{u}, t)dt + b_i(\mathbf{u}, t)dW_i(t), \quad (4.14)$$

4.3 PARTICLE METHOD FOR THE SOLUTION OF TRANSPORTED-PDF EQUATION

where a_i is the drift coefficient and b_i the diffusion coefficient defined by the stochastic modeled process. $W_i(t)$ is a isotropic Wiener process with the properties that: (i) its change $dW_i(t) = W_i(t + dt) - W_i(t)$ satisfies normal distribution with zero mean value ($\overline{dW_i(t)} = 0$); (ii) its covariance satisfies: $\overline{dW_i(t)dW_j(t)} = \delta_{ij} \cdot dt$ [72].

Thus the evolution of the corresponding modeled PDF $\tilde{f}_{u_i}^*$ is governed by:

$$\frac{\partial \tilde{f}_{u_i}^*}{\partial t} = -\frac{\partial}{\partial V_i} \left(a_i(\mathbf{u}, t) \cdot \tilde{f}_{u_i}^* \right) + \frac{1}{2} \frac{\partial^2}{\partial V_i \cdot \partial V_i} \left(b_i^2(\mathbf{u}, t) \cdot \tilde{f}_{u_i}^* \right). \quad (4.15)$$

Given the proper a_i and b_i , $\tilde{f}_{u_i}^*$ evolves in a similar manner as real PDF of \tilde{f}_{u_i} .

4.3.2 Modeling of particle velocity

If one knows the particle velocity, the position of particle in physical space can also be determined easily. There are various Langevin models developed for the velocity, and the most simple and widely used is the *simplified Langevin model* (SLM) [72]:

$$du_i^*(t) = -\frac{1}{\bar{\rho}} \frac{\partial \bar{p}}{\partial x_i} dt - \left(\frac{1}{2} + \frac{3}{4} C_0 \right) \Omega(u_i^*(t) - \tilde{u}_i) dt + \sqrt{C_0 k \Omega} dW_i \quad (4.16)$$

where Ω is the conditional Favre averaged turbulent frequency defined as:

$$\Omega = C_\Omega \frac{\overline{\rho^* \omega^* | \omega^* \geq \tilde{\omega}}}{\bar{\rho}}, \quad (4.17)$$

and k is the specific turbulent kinetic energy:

$$k = \frac{\widetilde{u_i'' u_i''}}{2}. \quad (4.18)$$

C_0 and C_Ω are two standard model parameters which can be set as default values as: $C_0 = 2.1$ and $C_\Omega = 0.6893$.

In Eq.4.16, the second term is the drift term with drift coefficient $a = -\left(\frac{1}{2} + \frac{3}{4} C_0\right) \Omega(u_i^*(t) - \tilde{u}_i)$. With this drift term the stochastic velocity of a particle tends to the averaged velocity of the particles. The third term in Eq.4.16 is a diffusion term with the diffusion coefficient $b = C_0 k \Omega$. This term is considered in order to model the dissipation process caused by viscosity.

4 TRANSPORTED-PDF EQUATION METHOD

However, the velocity model Eq.4.16 also contains information about the favre-averaged velocity ($u_i = \tilde{u}_i + u_i''$), which provides a redundant representation because favre-averaged velocity \tilde{u}_i is calculated through the RANS equation Eq.3.15 (coupling between RANS and transported-PDF see Chapter 6). To avoid this, it is suggested to use the following modified SLM for velocity fluctuation ($u_i''^* = u_i^* - \tilde{u}_i^*$) [43, 72]:

$$du_i''^*(t) = -\frac{1}{\bar{\rho}} \frac{\partial(\widetilde{\rho u_i'' u_j''})}{\partial x_j} dt - u_j''^* \frac{\partial \tilde{u}_i}{\partial x_j} dt - \left(\frac{1}{2} + \frac{3}{4} C_0 \right) \Omega u_i''^*(t) dt + \sqrt{C_0 k \Omega} dW_i \quad (4.19)$$

In this way, the position of a particle in physical space can be determined together by favre-averaged velocity (from RANS part) and velocity fluctuation (from Eq.4.19):

$$\frac{d\mathbf{X}^*}{dt} = \tilde{\mathbf{u}}(\mathbf{X}^*) + \mathbf{u}''^*. \quad (4.20)$$

More detailed description will be discussed in section 7.2.

4.3.3 Modeling of particle turbulent frequency

To close Eq.4.16 or Eq.4.19, a model for turbulent frequency is required. Furthermore, transported-PDF model does not contain any information about flow length scale and turbulent time scales, which can be obtained from model for turbulent frequency. This information is important especially for reacting flows, because turbulent time-scales have large influence on molecular transport processes and chemical kinetics, which will be illustrated in next section. For the model for turbulent frequency, the stochastic model for $\omega^*(t)$ proposed by [99] is used:

$$d\omega^*(t) = -C_3(\omega^* - \tilde{\omega})\Omega dt - S_\omega \Omega \omega^* dt + \sqrt{2C_3 C_4 \tilde{\omega} \Omega \omega^*} dW, \quad (4.21)$$

where C_3 and C_4 are two model parameters with values $C_3 = 1.0$ and $C_4 = 0.25$ [72, 99] Values of both model parameters are specified through comparison with the DNS data. S_ω is source of turbulent frequency defined as:

$$S_\omega = C_{\omega 2} - C_{\omega 1} \frac{P}{k\Omega}, \quad (4.22)$$

with two further model parameters $C_{\omega 1}$ and $C_{\omega 2}$ whose values depend on case. P is the turbulence production calculated as [72, 99]:

$$P = -\widetilde{u_i'' u_j''} \frac{\partial \tilde{u}_i}{\partial x_j}. \quad (4.23)$$

4.3.4 Modeling of molecular mixing

One of the challenging tasks for the transport-PDF method is to model the conditional diffusion term. This term describes the molecular mixing process, which, to a large extent, affects the accuracy of description for composition space evolution [18, 27, 38, 73]. To model the molecular mixing process physically, mixing models must fulfill several requirements as proposed in [18, 27]. The first requirement is that the scalar mean values must remain unchanged. The second is that mixing models must yield correct scalar dissipation rates. As explained in [73], the mixing process causes scalar variance decay, whose rate is determined by the scalar dissipation ϵ_ϕ :

$$\frac{1}{2} \frac{d\overline{\Psi'^2}}{dt} = -\epsilon_\phi. \quad (4.24)$$

Therefore, the characteristic scalar decay time-scale τ_ϕ can be obtained as:

$$\tau_\phi = \frac{1}{2} \frac{\overline{\Psi'^2}}{\epsilon_\phi}, \quad (4.25)$$

and the associated scalar decay frequency $\omega_\phi = 1/\tau_\phi$ can be modeled as:

$$\omega_\phi = 1/\tau_\phi = C_\phi \frac{\epsilon}{k}, \quad (4.26)$$

where k is the turbulence kinetic energy and ϵ its dissipation. C_ϕ is the so-called mixing model parameter, which is not a universal constant shown from both experiments and numerical studies [72, 73]. For reacting scalars, the determination of C_ϕ is complicated, because chemical kinetics lead to changing of turbulence length scales and thus affects the scalar variance decay rate [18, 73]. Therefore, C_ϕ must be adapted depending on the studied cases.

Furthermore, if one constant C_ϕ is applied for all thermo-kinetic state scalars, this implies that all scalars mix with the same time scales so that differential diffusion is not accounted for [27]. In this work, the effect and modeling of differential diffusion in mixing model are not considered. However, the usage of e.g. Reaction-Diffusion Manifolds (REDIMs) for simplifying chemical kinetics can partially take into account the differential diffusion, which will be illustrated in section 8.5. More details on differential diffusion modeling in the PDF method can be found in e.g. [32, 68, 101].

Most of the developed mixing models can satisfy these two requirements:

- the mean value remains unchanged and

4 TRANSPORTED-PDF EQUATION METHOD

- the scalar variance predicts the correct decay in time.

However, other requirements cannot be guaranteed by all models. For example, experiments and DNS show that the scalar PDF tends to relax to a Gaussian distribution in homogeneous turbulence from any initial shape of PDF [18, 27, 73]. As will be shown later, the Interaction by Exchange with the Mean (IEM) model, for example, preserves the PDF shape during the whole mixing process. Furthermore, scalar quantities must be bounded or within allowable regions (e.g. mass fraction of species must be less than 1, temperatures must be positive etc.) However, if one models the mixing process with Wiener processes, this requirement is difficult to fulfill and advanced techniques must be used [27]. Moreover, from the physical aspect, the modeled mixing processes should guarantee localness in geometric and composition space, which will be discussed later.

In the following, several mixing models are discussed and their advantages and disadvantages will also be summarized.

Interaction by Exchange with the Mean (IEM) Model

The most conventional and simplest micro-mixing model is the Interaction by Exchange with the Mean (IEM) model [25], which is schematic illustrated in Fig.4.2. In this model, the scalar values of each particles relax towards mean value of all particles $\tilde{\Phi}$ in a deterministic way:

$$\frac{d\Psi^{*,i}}{dt} = -\frac{1}{2}\omega_\phi (\Psi^{*,i} - \tilde{\Phi}). \quad (4.27)$$

This equation can be easily integrated numerically as:

$$\Psi^{*,i}(t + \Delta t) = \tilde{\Phi} + (\Psi^{*,i}(t) - \tilde{\Psi}) \cdot \exp\left(-\frac{1}{2}\omega_\phi \Delta t\right). \quad (4.28)$$

Although the IEM model is easy to use, it has one major drawback, namely the shape of scalar PDF remains und and thus never relaxes to a Gaussian distribution due to absence of mean scalar gradient [18, 22, 27]. This will be illustrated through the following example. Intuitively we have N_p number of particles that half of them have the scalar value $\Psi = 0$ and the rest half of them $\Psi = 1$. Using Eq.4.27 we show in Fig.4.3 the PDF evolution of scalar at different time $t_1 < t_2 < t_3 < t_4$. We see that indeed the IEM model preserves the initial scalar PDF. Furthermore, the IEM model does not consider the localness in either geometric space or composition space [18, 21, 46].

4.3 PARTICLE METHOD FOR THE SOLUTION OF TRANSPORTED-PDF EQUATION

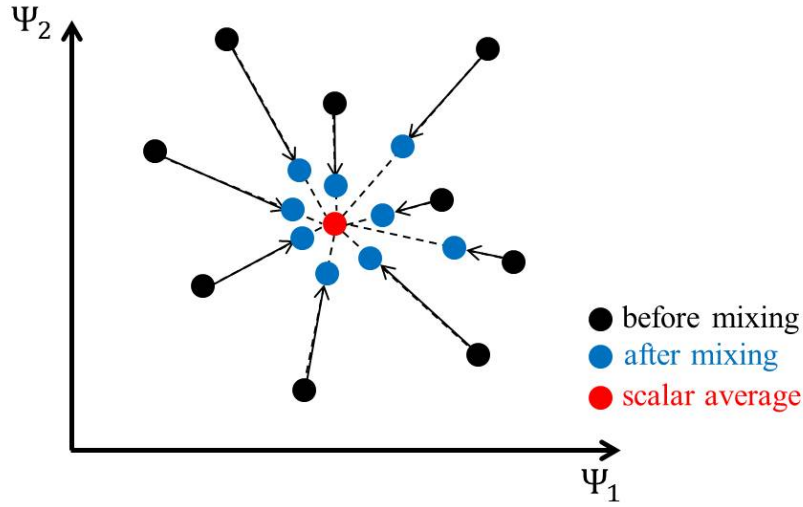


Figure 4.2: Schematic illustration of IEM mixing model.

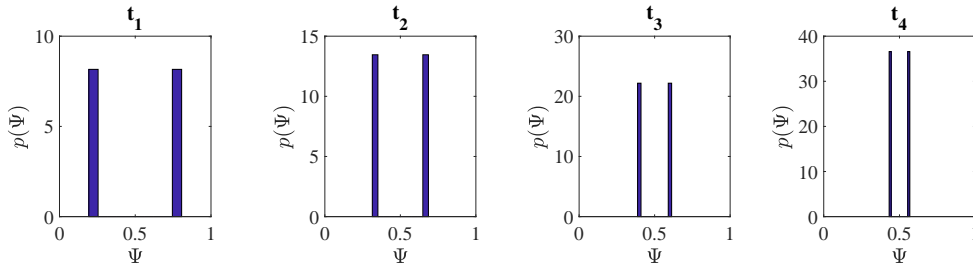


Figure 4.3: PDF evolution of scalar in a toy example for the IEM mixing model.

Modified Coalescence-Dispersion (Curl's) Model (MCM)

The modified Coalescence-Dispersion (Curl's) Model (MCM) [22, 42] is a stochastic model where particles mix in a random way, which is illustrated in Fig.4.4. In this MCM model, two particles p and q are selected randomly from the ensemble, and mixed with a certain probability p_{mix} in a timestep Δt linearly as:

$$\begin{aligned}\Psi^{*(p)}(t + \Delta t) &= \Psi^{*(p)}(t) + h \left(\hat{\Psi}^{(p,q)} - \Psi^{*(p)} \right) \\ \Psi^{*(q)}(t + \Delta t) &= \Psi^{*(q)}(t) + h \left(\hat{\Psi}^{(p,q)} - \Psi^{*(q)} \right)\end{aligned}\quad (4.29)$$

4 TRANSPORTED-PDF EQUATION METHOD

where h is the mixing extent with $h = 0$ for no mixing and $h = 1$ for complete mixing. $\hat{\Psi}^{(p,q)}$ is the average value of particle pair (p, q) . For $\Delta \rightarrow 0$, the desired variance decay can be obtained if p_{mix} is chosen as:

$$p_{\text{mix}} = \omega_\phi \cdot N_p \cdot \Delta t. \quad (4.30)$$

It can be observed from Eq.4.30, because selected particles are mixed only with certain probability, only a certain number of particles take part in mixing process, while rest of particles remain their old values.

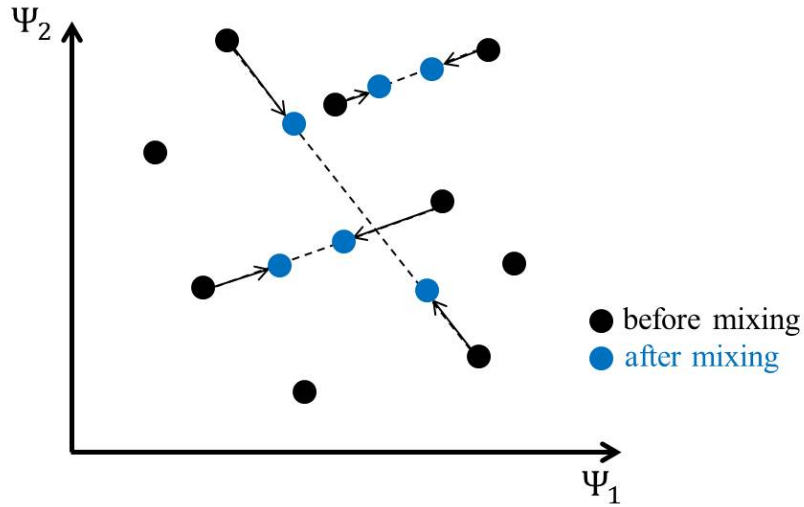


Figure 4.4: Schematic illustration of MCM mixing model.

Again we have N_p number of particles that half of them have the scalar value $\Psi = 0$ and the rest half of them $\Psi = 1$, as used in last section. Using Eq.4.29 we show in Fig.4.5 the PDF evolution of a scalar for different times $t_1 < t_2 < t_3 < t_4$. We notice that starting from initial scalar PDF, it relaxes to a Gaussian distribution, which makes MCM superior to the IEM model. However, just like IEM, the MCM has the most significant shortcoming that it does not guarantee localness either in geometric space nor in composition space because of its random selection procedure, which causes discontinuous jump processes [21, 46].

Generalized Multiple Mapping Conditioning (MMC) Model

The algorithm of the MCM model is to select two particles randomly which will be mixed with each other. However, such randomness can cause unphysical mixing [18, 27]. For example, one selects randomly one particle from unburnt

4.3 PARTICLE METHOD FOR THE SOLUTION OF TRANSPORTED-PDF EQUATION

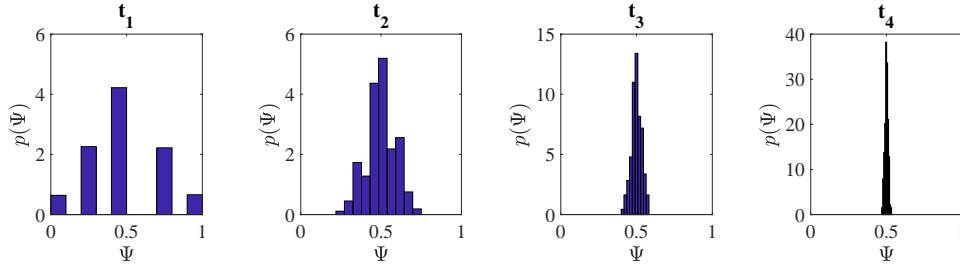


Figure 4.5: PDF evolution of scalar in toy example for MCM mixing model.

gas side, and the other one from exhausted gas side. And unburnt gas side and exhausted gas side are separated by the flame zone. If both particles are mixed, it means that mixing process occurs between unburnt gas and exhausted gas, without considering any influence of the flame zone. Therefore the MCM model can cause discontinuous jump processes and thus non-localization in geometric and composition space. The multiple mapping conditioning (MMC) model overcomes such limitation and fulfills the property of localness [21, 46].

The MMC model enforces locality in geometric and composition space using one or more reference variables. In the original version in [46] it requires the reference variables to be modeled by Markov processes. Later, this algorithm has been simplified and a generalized MMC model has been developed [21], which is illustrated in Fig.4.6. In the generalized MMC model, one still uses MCM model with one exception that the generalized MMC enforces mixing of particle pairs that are close in both reference variable and geometric spaces. This ensures the property of localness.

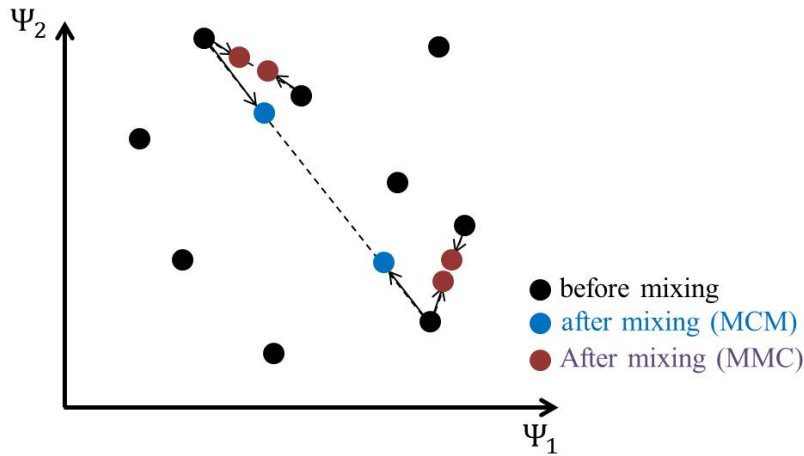


Figure 4.6: Schematic illustration of MMC mixing model.

4 TRANSPORTED-PDF EQUATION METHOD

In the concept of generalized MMC, one introduces the so-called reference variable(s) ζ that are combustion relevant (e.g. fluctuations of velocity, scalar dissipation, sensible enthalpy). Then, unlike the MCM model, the particles in MMC model must be mixed locally in ζ -space. That is, two particles are selected so that the normalized square distance:

$$\hat{d}_{p,q}^2 = \frac{1}{1 + \lambda^2} \cdot \left[\sum_{j=1}^3 \left(\frac{x_i^{*,(p)} - x_i^{*,(q)}}{L_x} \right)^2 + \lambda^2 \cdot \left(\frac{\zeta^{*,(p)} - \zeta^{*,(q)}}{L_\zeta} \right)^2 \right] \quad (4.31)$$

is minimized. L_x and L_ζ are characteristic geometric and reference scales. λ is a parameter determining the relative localization in geometric and reference space. If $\lambda = 0$, then localization is only in geometric space. If $\lambda \rightarrow \infty$, then localization is only in reference variable space. Note that the choice of reference variable is important in the MMC modeling. As stated in [21], the reference variable should have a strong effect on combustion processes, otherwise the localization procedure would be meaningless. In non-premixed reacting system, one of the logical choices for reference variable is the mixture fraction. However, generally MMC can also use other important reference variables such as velocity fluctuation, scalar dissipation or other useful quantities [21].

Euclidean minimum spanning tree (EMST) model

Another approach to enforce particles closer in composition space to mix each other than those further away is the so-called Euclidean minimum spanning tree (EMST) model [91]. Unlike the MMC model where the localization is realized in reference variable space, the EMST model focuses on the localization directly in composition space for multiple scalars, where the one-dimensional ordering in reference variable space is replaced by an Euclidean minimum spanning tree. In other words, the EMST model organizes the particles within one cell into a minimum spanning tree such that mixing process occurs only between particles that are nearest neighbors in composition space.

Summary on discussed mixing models

In Tab.4.1 we summarize the advantages and disadvantages of discussed mixing models (IEM, MCM, MMC and EMST) briefly. The symbol "+" means that the requirements are completely fulfilled and the symbol "-" means that the requirements are not fulfilled. For symbol "+/-" the requirements are partly fulfilled, which means that such property is dependent on specific cases.

4.3 PARTICLE METHOD FOR THE SOLUTION OF TRANSPORTED-PDF EQUATION

We notice that for MMC all requirements can be completely fulfilled, while for EMST the property "Relaxation to Gaussian distribution" is only partly fulfilled. However, for the studied Sandia Flame series, the application of EMST can also be used and this property for Sandia Flame series is fulfilled. Therefore, in this work, the EMST mixing model is selected and the code can be downloaded from [78].

Requirements	IEM	MCM	MMC	EMST
Preservation of scalar average	+	+	+	+
Decay of scalar variance	+	+	+	+
allowable region	+	+	+	+
Relaxation to Gaussian distribution	-	+	+	+/-
localness in composition space	-	-	+	+

Table 4.1: Mixing models considered in present work and their fulfillment of requirements. +: completely fulfilled; +/-: partly fulfilled; -: not fulfilled.

4.3.5 Evolution of particle thermo-kinetic state due to source

A significant advantage of using the transported-PDF method is that the thermo-kinetic source term (S_α in Eq.4.12) is in a closed form and without modeling. Therefore, particle thermo-kinetic states due to their source can be solved directly using:

$$\frac{d\Psi^{*,i}}{dt} = \mathbf{S}(\Psi^{*,i}), \quad (4.32)$$

which is expressed as system of ODEs with dimension $n = n_{sp} + 2$ (n_{sp} number of species, pressure and enthalpy).

Typically, this system of ODEs (Eq.4.32) using detailed chemical mechanism has become very complex in terms of dimensionality and non-linearity [35, 95]. For instance, for the simulation of CH_4 reacting system, one must solve 55 ODEs for thermo-kinetic state based on GRI 3.0 detailed chemistry ([81]). The characteristic time-scales can vary from order of magnitude $\text{O}(10^{-8}\text{s})$ to $\text{O}(10^2\text{s})$. Thus, advanced time step must at least of the same order of the shortest chemical time-scales, leading to a large number of integration steps. Therefore, the largest problem in the evolution of particle thermo-kinetic state is the high computational cost in the numerical integration of Eq.4.32. In the next chapter, concepts of model reduction for chemical kinetics and

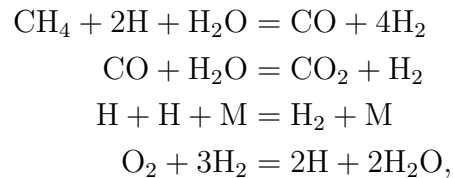
4 TRANSPORTED-PDF EQUATION METHOD

two methodologies used in this work are discussed in details, in order that computational effort due to chemical kinetics can be largely reduced while keeping accuracy sufficiently high for reacting systems.

5 Model reduction for chemical kinetics

Detailed chemical mechanisms involve more than hundred (even up to thousand) chemical species [48, 95]. Therefore, more than hundred governing equations for species (Eq.2.3) must be solved. Furthermore, due to non-linearity of elementary reaction rates, the stiffness of the system of governing equation is typically high, which enormously complicates the numerical integration [35, 57, 95]. Problems of both high dimensionality and high stiffness of the governing equation system leads to a very high computational load with respect to CPU time and a large memory storage required to handle combustion systems numerically, especially for general 3D reacting flows with complex geometry [35, 48].

Hence, there is an increasing demand for model reduction for chemical kinetics. A reduced chemistry aims at reducing both stiffness and number of governing equations for thermo-kinetic state to be integrated in the numerical simulation. The most simple one approach is the global chemistry involving one or several steps. For example, in [66] a four-step global chemical reactions for methane including seven species are proposed:



and the reaction rates are determined by using additional approximations. Although schemes of global chemical reactions are attractive due to simplicity and its easy application, it still involves various difficulties:

- Although the number of chemical species and chemical reactions is decreased, reaction rates have more complicated expressions ¹.

¹One can refer to [66] regarding the reaction rates for the four-step global chemical reactions for methane. Furthermore, one can also refer to the reduced chemical mechanisms in <http://spark.engr.uconn.edu/mechs/mechs.htm> as example

- For important processes such as ignition and extinction, such global chemical reactions are over-simplified to capture these processes, because more species will dominate.
- For pollutants such as soot, NO_x and unburnt hydrocarbons, more species and reactions are required.

Therefore, it is necessary to develop reduction methods for chemical kinetics which simplify the chemical kinetics while still retaining the essential dynamic features of the reacting systems. In this work, two manifold based simplified chemistries are discussed. In Sec.5.1, the dynamical behavior of chemical reaction systems are investigated, where is the basis for the development of manifold based simplified chemistry. Then two different reduction methods are discussed. One is the Global Quasi-linearization (GQL) [11] which reduces the chemical kinetics without consideration of physical transport. The other one is the Reaction-Diffusion Manifold (REDIM) [10] which takes into account physical transport. Both methods will be verified through CH₄ combustion system, and used in the turbulent flame modelling in this thesis.

5.1 Dynamical behavior of chemical reaction systems

The chemical reacting systems are controlled by different processes: chemical process involving reactions, and physical process involving convection and molecular diffusion etc.. Different processes usually undergo time-scales with large different orders of magnitude [35, 57, 95]. Typically, chemical time-scales in combustion systems can cover a wide range of O(10⁻¹⁰s) to O(1s), and this range of chemical time-scales is much larger than the range of physical time-scales introduced by e.g. convection or molecular diffusion [35]. Furthermore, many chemical time-scales are much faster than physical time-scales, so that these fast time-scales can be decoupled from combustion systems, yielding a simplified chemical kinetics that the full thermo-kinetic state can be represented by only a small number of variables [35, 57]. This issue is now illustrated in Fig.5.1 through a homogeneous reacting system with the governing equation:

$$\frac{\partial \Psi}{\partial t} = \mathbf{S}(\Psi), \quad (5.1)$$

where convection and diffusion terms in Eq.2.14 are not taken into account. Different initial conditions have been selected such that their corresponding

5.1 DYNAMICAL BEHAVIOR OF CHEMICAL REACTION SYSTEMS

reacting systems evolve until they reach the same equilibrium state for $t \rightarrow \infty$. Figure 5.1 shows sample trajectories of chemical reactions in a CH_4 -air homogeneous reacting system in the composition space (color lines). Projections into the H_2O -, CO - and $\text{H}-\text{CO}_2$ planes are plotted as example to illustrate the typical dynamic behaviors of chemical reacting systems. Trajectories after different relaxation times ($t > 0s$, $t > 5 \cdot 10^{-5}s$, $t > 1 \cdot 10^{-4}s$ and $t > 1 \cdot 10^{-3}s$), are shown. It can be observed that if the first $1 \cdot 10^{-4}s$ have been omitted, system dynamics can be simplified considerably. Within $1 \cdot 10^{-4}s$, almost all trajectories have merged into a one-dimensional (1D) single line in the state space. Thus, state of the whole system can be described by only one variable. The reason for this behavior is that within this short time processes controlled by fast time-scales (fast relaxation processes) dominate and are exhausted. After $1 \cdot 10^{-3}s$, system can be even approximated by its equilibrium state.

To summarize, if one is interested in the system dynamics after $1 \cdot 10^{-4}s$, then the system can be approximated using one progress variable which determines the dynamics of the system, namely the movement along the 1D manifold in state space. If one is interested in system dynamics after a shorter relaxation time (e.g. $t > 5 \cdot 10^{-5}s$ in this example), additional progress variables have to be introduced.

Based on this observation, it can be formulated that a typical combustion system can be decomposed into slow and fast processes due to the existence of different orders of magnitude in time-scales [35, 57, 95]. Therefore, the system state space belongs to an m_s -dimensional manifold (usually $m_s \ll n$) which can be expressed in an explicit form [10, 35]:

$$\mathcal{M} = \{ \Psi : \Psi = \Psi(\theta), \Psi : R^{m_s} \rightarrow R^n \}, \quad (5.2)$$

where Ψ is the thermo-kinetic state vector (see Eq.2.14) and θ is an m_s -dimensional vector of reduced coordinate parametrizing this slow manifold. The remaining question is to identify such low-dimensional manifold \mathcal{M} , which is the main topic in the rest of this chapter.

5 MODEL REDUCTION FOR CHEMICAL KINETICS

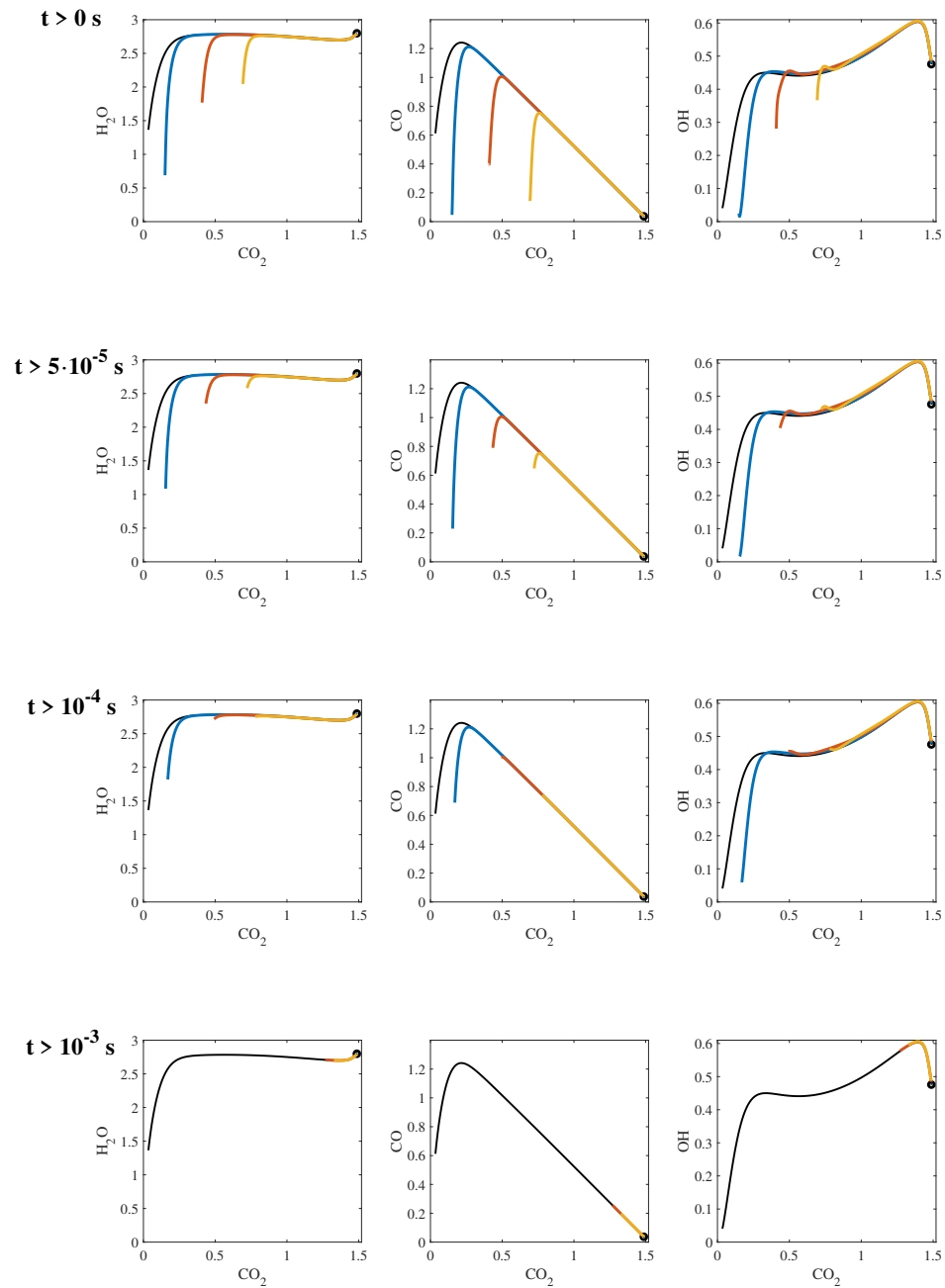


Figure 5.1: Trajectories of the chemical reaction for a CH_4 -air combustion system. \circ denotes the equilibrium point. Color lines: trajectories with different initial conditions. Black line: one common attracting trajectory; Four different relaxation times ($t > 0s$, $t > 5 \cdot 10^{-5}s$, $t > 1 \cdot 10^{-4}s$ and $t > 1 \cdot 10^{-3}s$) are shown.

5.2 Global Quasi-linearization (GQL) for the model reduction without physical transport

Historically, several first reduction methods for chemical kinetics have been developed by considering homogeneous reacting systems without physical processes such as convection and molecular transport. In other words, there exists no spatial differences of thermo-kinetic quantities. The homogeneous reacting system considered in this section is the system under adiabatic and isobaric condition. The governing equations (Eq.2.14) can thus be simplified to the following system of ordinary differential equations (ODEs):

$$\frac{\partial h}{\partial t} = 0, \quad (5.3a)$$

$$\frac{\partial p}{\partial t} = 0, \quad (5.3b)$$

$$\frac{\partial \phi_i}{\partial t} = \frac{\dot{\omega}_i}{\rho}, \quad i = 1, 2, \dots, n_{sp}, \quad (5.3c)$$

or it can also be written in vector notation in the form:

$$\frac{\partial \Psi}{\partial t} = \frac{\partial}{\partial t} \begin{bmatrix} h \\ p \\ \phi \end{bmatrix} = \mathbf{S}(\Psi). \quad (5.4)$$

Recall that in the equations above, h denotes the specific enthalpy of the system, p the pressure, $\dot{\omega}_i$ the molar rate for the formation of a chemical species i , and ϕ_i the specific mole numbers. This mathematical model describes the evolution of n_{sp} chemical species with two additional variables describing thermodynamic properties (h and p here).

Two conventional methods, Quasi-Steady State Approximation (QSSA) [9] and Partial Equilibrium Approximation (PEA) [19], are intensively studied and employed for the generation of reduced chemical kinetics based on homogeneous reacting system. However, application of both approximations still faces with several difficulties. The most significant problem is that one must decide which species can be assumed being at quasi-steady state or which elementary reactions can be assumed equilibrated. Verification of these assumptions before the numerical experiments are conducted is difficult. Thus, only post-processing can verify the validity and accuracy, requiring a significant amount of time validation for human resources. These methods are even more challenging when the assumptions are valid only for limited ranges

of initial conditions or in a certain stage of system evolution (e.g. during an induction period of the ignition). It was shown in [109] that even for the hydrogen/air system, one needs two different QSSA strategies to describe the auto-ignition processes for low and high initial temperatures. In the following, the Global Quasi-linearisation (GQL) approach [11] is discussed. It is a manifold-based reduction method based on characteristic time-scale analysis, allowing a global identification of fast and slow processes.

5.2.1 Mathematical Model for the Global Quasi-linearization (GQL) Approach

The concept of GQL approach stems from the singular perturbation theory which state that a low dimensional manifold can be obtained if a singular perturbation occurs in system [83]. However, unlike the singular perturbation theory which defines the fast and slow motion explicitly, the system of ODEs describing homogeneous reacting system Eq.5.4 gives us no explicit information about the fast and slow time-scales. The Global Quasi-linearization (GQL) approach is one possibility that allows us a global identification of the fast and slow decomposition of ODE systems . The decomposition is based on the linearisation of the thermo-chemical source term, leading to an explicit and fixed separation of fast and slow subspaces. In this section, the mathematical model for the GQL approach will be reviewed.

The GQL approach is based on three main assumptions [11]:

- There exists a decomposition of fast and slow processes of the system.
- The vector field $\mathbf{S}(\Psi)$ of the system (5.3c) possesses a linear transformation of the original coordinate system, and it can be decomposed into sub-fields describing processes having different characteristic timescales.
- The decomposition is valid everywhere inside our domain of interest. This domain of interest can be described as the domain with physically relevant values of system state variables for considered application range (e.g. positive concentrations, temperatures etc.) [109].

As it is often observed for typical combustion systems, because of the existence of time scales that differ in several orders of magnitude, it allows us to decompose the system dynamics into fast and slow motions according to singular perturbation theory. Therefore, these three assumptions are in most cases applicable for chemical reacting systems.

If the second assumption is valid, then there is a matrix \mathbf{T}_{GQL} as a linear approximation in the domain of the vector field (5.3c):

$$\mathbf{S}(\Psi) \approx \mathbf{T}_{\text{GQL}} \cdot \Psi, \quad (5.5)$$

which has the simple geometrical interpretation of mapping the state vectors Ψ to vectors $\mathbf{S}(\Psi)$ and describes the linear transformation needed. Note that since the source term is strongly non-linear, a linear and an accurate approximation of the source term is not possible. Indeed the motivation of Eq.5.5 is not to use the linearization form of source term to solve the ODE system, but to use this linearization to define the subspaces for decomposition and, thus, describing the slow manifold. Then under assumption that the dynamical system has time-scales with different orders of magnitude, this global linear transformation matrix \mathbf{T}_{GQL} can be used to identify and validate the assumptions about constant decomposition and to approximate relevant subspaces of fast and slow motions. Similar to the concept in the ILDM technique [51, 52] by using e.g. the eigenvalue/eigenvector decomposition we obtain [54]:

$$\mathbf{T}_{\text{GQL}} = \mathbf{Q}\Lambda\tilde{\mathbf{Q}} = \begin{pmatrix} Q_s & Q_f \end{pmatrix} \cdot \begin{pmatrix} N_s & N_{sf} \\ 0 & N_f \end{pmatrix} \cdot \begin{pmatrix} \tilde{Q}_s \\ \tilde{Q}_f \end{pmatrix}. \quad (5.6)$$

where Q_s is an orthogonal basis of the slow subspace. In order to obtain a basis for the fast subspace, the Sylvester equation needs to be solved [34]:

$$N_s \cdot X - X \cdot N_f = -N_{sf}, \quad (5.7)$$

and the invariant subspaces $Z = (Z_s, Z_f)$ is calculated according to [54]:

$$\begin{pmatrix} \tilde{Z}_s \\ \tilde{Z}_f \end{pmatrix} = \begin{pmatrix} \mathbf{I} & -X \\ 0 & \mathbf{I} \end{pmatrix} \cdot \begin{pmatrix} \tilde{Q}_s \\ \tilde{Q}_f \end{pmatrix}, \quad (5.8)$$

$$(Z_s \ Z_f) = (Q_s \ Q_f) \cdot \begin{pmatrix} \mathbf{I} & X \\ 0 & \mathbf{I} \end{pmatrix} \quad (5.9)$$

where Z_s ($n \times m_s$) are the invariant slow subspaces corresponding to the group of relatively "small" eigenvalues N_s ($m_s \times m_s$), and Z_f ($n \times m_f$) are the invariant fast subspaces corresponding to the group of relatively "large" eigenvalues N_f ($m_f \times m_f$). The GQL and ILDM have the same algorithm using the timescale analysis and employing the Jacobian matrix to define the fast and slow subspace. However, there is one significant difference between GQL and ILDM. For ILDM the local Jacobian matrix of source term must be evaluated

at each state, and the eigenvalue-eigenvector decomposition must be applied for each state [51, 54]. Therefore the invariant slow and fast subspaces change with state. For GQL one needs to apply eigenvalue/eigenvector decomposition for one time and the resulting invariant slow and fast subspaces are globally valid [11]. Note that although a local basis of eigenvectors for strongly non-linear system such as combustion changes drastically e.g. before and after ignition, the subspaces still remain approximately the same with a high accuracy, which will be demonstrated later.

The singular perturbation hidden parameter ϵ can be estimated by the gap between the largest eigenvalue in group N_s and the smallest eigenvalue in group N_f [11, 13]:

$$\epsilon = \frac{\max |\lambda^{\text{real}}(N_s)|}{\min |\lambda^{\text{real}}(N_f)|} \ll 1. \quad (5.10)$$

Thus, we can transfer the original ODE systems into a singular perturbed system by introducing new coordinates for state vector:

$$\begin{aligned} \mathbf{u} &= \tilde{Z}_s \cdot \Psi, \\ \mathbf{v} &= \tilde{Z}_f \cdot \Psi, \end{aligned} \quad (5.11)$$

here $\mathbf{u} = (\mathcal{U}_1, \dots, \mathcal{U}_{m_s})^T$ is the vector consisting new variables describing slow motions and $\mathbf{v} = (\mathcal{V}_1, \dots, \mathcal{V}_{m_f})^T$ the fast motions. The fast subsystem is then given as:

$$\begin{aligned} \mathbf{u} &= \mathbf{u}_0 \\ \frac{d\mathbf{v}}{dt} &= \tilde{Z}_f \cdot \mathbf{S} \left((Z_s \ Z_f) \cdot \begin{pmatrix} \mathbf{u} \\ \mathbf{v} \end{pmatrix} \right), \end{aligned} \quad (5.12)$$

The slow subsystem reads:

$$\begin{aligned} \frac{d\mathbf{u}}{dt} &= \tilde{Z}_s \cdot \mathbf{S} \left((Z_s \ Z_f) \cdot \begin{pmatrix} \mathbf{u} \\ \mathbf{v} \end{pmatrix} \right), \\ 0 &= \tilde{Z}_f \cdot \mathbf{S} \left((Z_s \ Z_f) \cdot \begin{pmatrix} \mathbf{u} \\ \mathbf{v} \end{pmatrix} \right). \end{aligned} \quad (5.13)$$

The fast and slow subsystems have clear physical meanings which are illustrated schematic in Fig.5.2:

Fast motion: During the fast motion, slow variables do not change (point line in Fig.5.2) leading to the condition $\mathbf{u} = \mathbf{u}_0$ and the system evolution

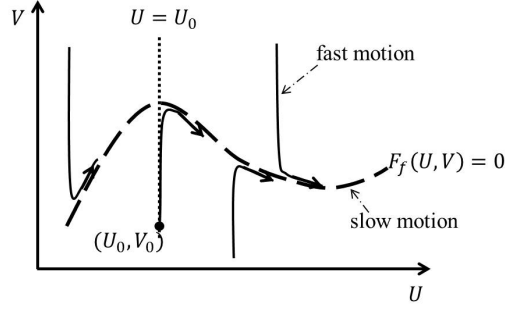


Figure 5.2: Schematic representation of fast (point line) and slow (dashed line) manifolds and solution trajectories (solid lines) in state space.

is only described by fast variables (ODE for $\frac{d\mathbf{V}}{dt}$ term). Typically, this fast motion lasts in the asymptotic sense for a time of the order of $O(\epsilon)$ (Eq.5.10), until the system trajectory started from $(\mathbf{U}_0, \mathbf{V}_0)$ instantly approaches the phase of slow motion.

Slow motion: During the slow motion, since the fast time-scales are exhausted, the system dynamics is constrained on the slow manifold (algebraic equation in Eq.5.15). The system state will move along the slow manifold until reaching equilibrium state.

In the numerical calculation, it is convenient to express the Eq.5.14 and 5.15 in their original coordinate system. In this way the fast subsystem is described in original coordinate as follows [109]:

$$\begin{aligned} \tilde{Z}_s \cdot \Psi &= \tilde{Z}_s \cdot \Psi_0 \\ \frac{\partial \Psi}{\partial t} &= Z_f \cdot \tilde{Z}_f \cdot \mathbf{S}(\Psi), \end{aligned} \quad (5.14)$$

And the slow subsystem is described in original coordinate in the form of DAE system as follows [109]:

$$\begin{aligned} \frac{\partial \Psi}{\partial t} &= Z_s \cdot \tilde{Z}_s \cdot \mathbf{S}(\Psi) \\ 0 &= \tilde{Z}_f \cdot \mathbf{S}(\Psi), \end{aligned} \quad (5.15)$$

5.2.2 Implementation of GQL approach

The basic idea in the implementation of GQL approach is that one finds a GQL reduced chemistry with minimal dimension m_s for one arbitrary specific initial conditions (initial temperature T_0 , initial pressure p_0 and fuel/air equivalent ratio Φ) defined at the starting point. Then this GQL

reduced chemistry will be validated for varying initial conditions and mixture compositions. An optimal GQL reduced chemistry is the one that predicts several important quantities (e.g. ignition delay times) of all varying initial conditions within user-defined tolerance. Fig.5.3 shows a detailed procedure for the implementation of GQL reduced chemistry. It consists mainly of three blocks, which will be described in details in the following.

Block 1: Initial set-up:

In this block, one arbitrary specific initial condition (initial temperature T_0 , initial pressure p_0 and fuel/air equivalent ratio Φ) is specified. In order to investigate the performance of a GQL reduced chemistry, one must also specify certain target-quantities for the validation. Such target-quantities can be ignition delay time for homogeneous reacting system or laminar flame speed for premixed flame. Then one defines a tolerance ϵ_{tol} so that the relative errors ϵ_{rel} of target-quantities must be less than this tolerance. Finally the dimension of reduced chemistry is set to be equal to the dimension of original detailed system ($m_s = n$) as starting point.

Block 2: Generation of GQL reduced chemistry for one specific case:

In this block, the main task is to generate a GQL reduced chemistry for one specific initial condition. A \mathbf{T}_{GQL} is built-up and the corresponding eigenvalue/eigenvector are calculated. Depending on m_s , the system will be decomposed by using invariant subspaces and the $Z = (Z_s, Z_f)$ and $\tilde{Z} = (\tilde{Z}_s, \tilde{Z}_f)^T$ are determined. Then Eq.5.15 based on m_s -dimensional GQL reduced chemistry will be integrated. Finally the target-quantities based on m_s -dimensional GQL reduced chemistry and detailed chemistry are compared. If the relative errors are within tolerance ϵ_{tol} , dimension of GQL reduced chemistry is decreased by 1 ($m_s = m_s - 1$), and the invariant subspaces will be re-computed based on new dimension m_s . This procedure will be repeated until relative errors of target-quantities based on GQL reduced chemistry with decreased m_s dimension are no longer smaller than tolerance ϵ_{tol} .

Before the procedure continues to block 3, dimension of GQL reduced chemistry is re-set to $m_s = m_s + 1$, which corresponds to the lowest dimension of GQL reduced chemistry to ensure that the relative errors of target-quantities are within tolerance. Then the invariant subspaces $Z = (Z_s, Z_f)$ and $\tilde{Z} = (\tilde{Z}_s, \tilde{Z}_f)^T$ are computed for continuing validation in block 3.

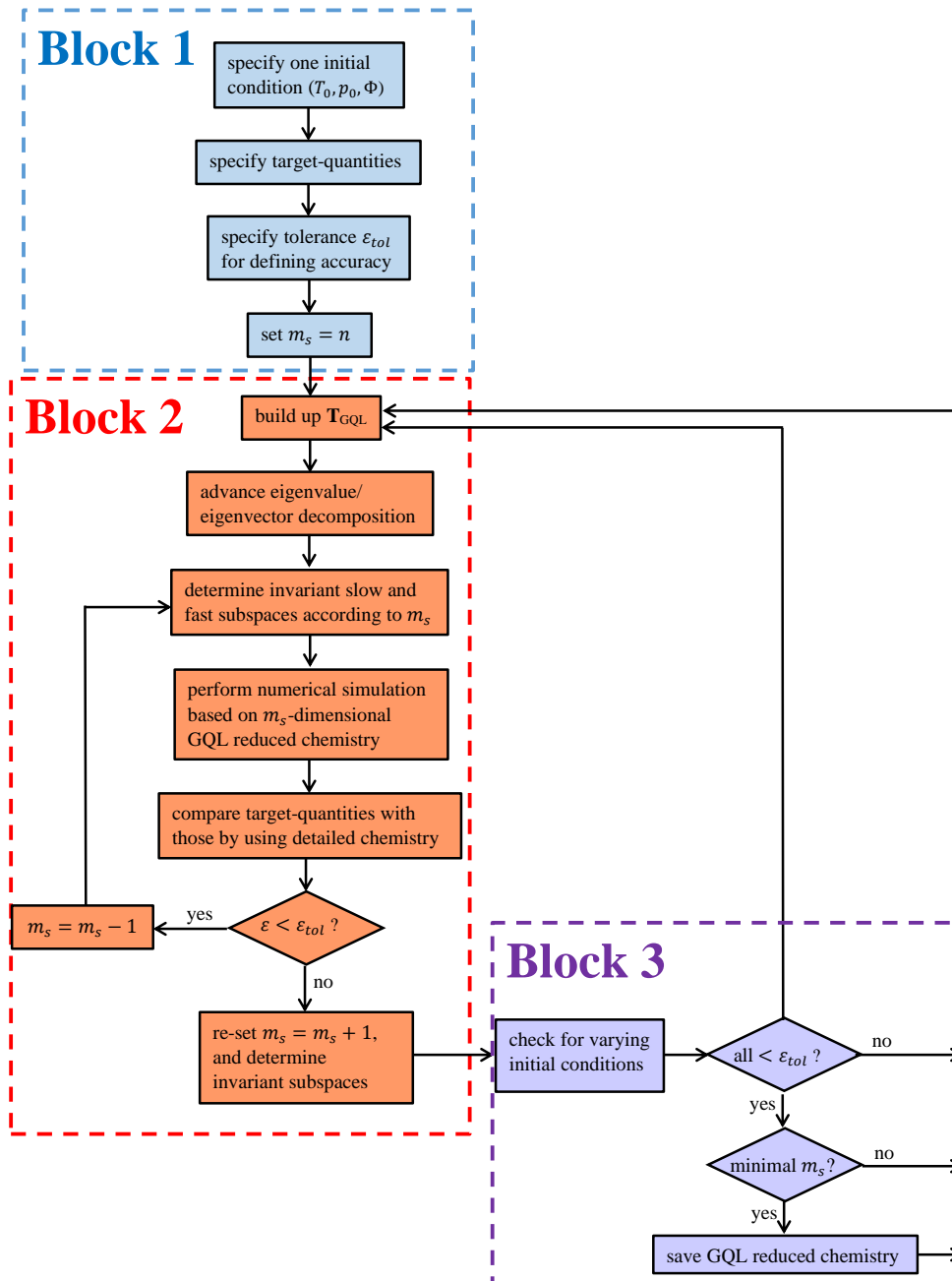


Figure 5.3: flow chart of generation of GQL reduced chemistry.

Block 3: Validation of GQL reduced chemistry for varying initial conditions:

In Block 2, an m_s -dimensional GQL reduced chemistry is constructed for one specific initial condition defined in block 1, and will be further validated for varying initial conditions. Several typical conditions (e.g. highest and lowest initial temperatures and pressures, richest and leanest mixture compositions) can be selected here for this further validation.

If relative errors of target-quantities for all selected initial conditions are within tolerance, one should also check whether this new GQL reduced chemistry has smaller relative errors for all selected initial conditions than the one already stored. If yes, the stored one will be replaced by this new m_s -dimensional GQL reduced chemistry. If not, a new \mathbf{T}_{GQL} is built-up and a new iteration started.

If the relative errors of target-quantities for any selected initial condition is larger than specified tolerance, this GQL reduced chemistry will be considered as "invalid". The procedure goes back to block 2 to build up a new \mathbf{T}_{GQL} , and a new iteration is started. Such iteration is repeated for a large amount of times (say 10^5 times), ensuring that the GQL reduced chemistry has indeed the lowest dimension and is valid for a wide range of application range.

5.2.3 Some comments on GQL implementation**Comment 1: Issue about constructing a \mathbf{T}_{GQL} :**

In Block 2, building up a \mathbf{T}_{GQL} is the most important step, since it is used for the determination of invariant subspaces. Several algorithms have been suggested and validated. One possibility [11] is to select n linearly independent vectors $[\Psi_1, \dots, \Psi_n]$ in such a way that the corresponding vector field $[\mathbf{S}(\Psi_1), \dots, \mathbf{S}(\Psi_n)]$ is also linear independent. Then \mathbf{T}_{GQL} can be determined by using $\mathbf{T}_{\text{GQL}} = [\mathbf{S}(\Psi_1), \dots, \mathbf{S}(\Psi_n)] \cdot [\Psi_1, \dots, \Psi_n]^{-1}$. However, this algorithm can cause degeneration and thus may lead to an artificial decomposition [11]. To overcome this problem, in [109] another algorithm was proposed based on the mean value theorem. In this algorithm, the linear approximation of the original vector field is described by one Jacobian matrix, and thus this Jacobian matrix can represent the global behaviors of the system dynamics. In this case, $\mathbf{T}_{\text{GQL}} = \mathbf{J}(\Psi_{\text{ref}})$, where Ψ_{ref} is the state where one determines the Jacobian matrix.

Comment 2: Integration of system using GQL reduced chemistry:

In GQL approach, system is decomposed explicitly into fast and slow subsystems. In the numerical calculation based on GQL reduced chemistry, the system is first integrated using Eq.5.14 describing fast subsystem, and then integrated using Eq.5.15 describing slow subsystem till equilibrium point.

As pointed in [109], with an optimal dimension of GQL reduced chemistry, numerical simulation shows that the time for initial states to relax towards GQL slow manifolds lasts extremely short. In other words, the initial states are already very close to the GQL slow manifolds. Therefore, integration of fast subsystem is not necessary, and integration of the slow subsystem using Eq.5.15 is sufficient. This issue has been validated in different combustion system such as H₂-air [109] and CH₄-air [110].

However, if one has a lower dimension of GQL reduced chemistry so that the initial states cannot be considered close to the GQL slow manifolds, then the system must be integrated using both fast and slow subsystems.

5.2.4 GQL approach for a CH₄/Air Auto-Ignition

In this section, the Global Quasi-linearization (GQL) approach is applied for the methane/air auto-ignition combustion system. The CH₄ detailed mechanisms used is the San Diego mechanism [106], which consists of $n_{sp} = 48$ reacting species and $n_r = 247$ elementary reactions (without He and Ar). Therefore the total dimension of Eq.(5.4) is $n = n_{sp} + 2 = 50$, consisting of $n_c = 6$ conserved quantities (2 conserved quantities related to the enthalpy h and the pressure p , and 4 related to element conservation for atoms of C, O, H and N), and the dimension of reacting subspace is $n - n_c = 50 - 6 = 44$. The reactor simulation is performed varying equivalence ratios from 0.4 to 3.0, and initial pressures and temperatures are varied from 1 to 150 bar and 1000 to 2000 K, respectively.

At the very beginning, one specific initial condition with $T_0 = 1800\text{K}$, $p_0 = 1\text{bar}$ and stoichiometric mixture composition $\Phi = 1.0$ is considered. The ignition delay time τ_{ign} is selected as target-quantity. The tolerance to qualify the GQL reduced chemistry is set to be 6%, which is one order of magnitude less than deviations of τ_{ign} predicted by different detailed mechanisms [110]. Figure 5.4 shows the convergence curves of relative errors of ignition delay times against dimension of GQL reduced chemistry for this specific initial condition ($T_0 = 1800\text{K}$, $p_0 = 1\text{bar}$, $\Phi = 1.0$), following the procedure in block 2. A minimal dimension of $m_s = 14$, which ensures the accuracy (less than 6%) for this specific initial condition, can be achieved.

5 MODEL REDUCTION FOR CHEMICAL KINETICS

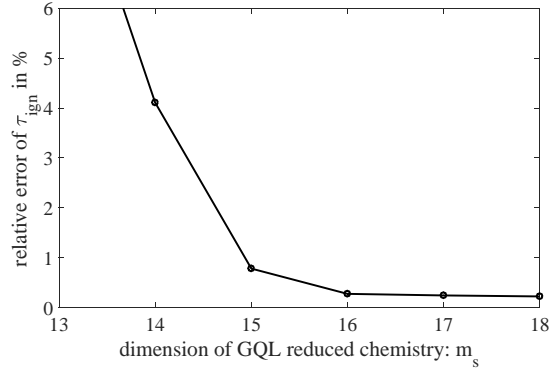


Figure 5.4: Relative errors in % versus dimension of GQL reduced chemistry for initial condition: $T_0 = 1800\text{K}$, $p_0 = 1\text{bar}$ and stoichiometric mixture composition $\Phi = 1.0$.

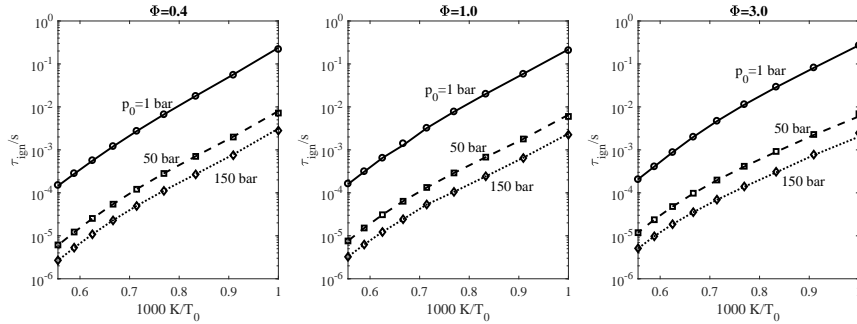


Figure 5.5: Comparison of ignition delay times between detailed (symbols) and GQL reduced chemistry (Lines). Figure from [110].

For the further validation for varying initial conditions in block 3, eight initial conditions (combination of lowest and highest initial temperatures and pressures, and richest and leanest mixture compositions) are selected, ensuring that the GQL reduced chemistry should be applicable for the considered wide range of conditions. The iteration in block 2 and block 3 is repeated for 10^5 times, and an optimal 14-dimensional (14D) GQL reduced chemistry is obtained.

In Fig.5.5 ignition delay times are compared between detailed chemistry (symbols) and 14D GQL reduced chemistry (lines) for the considered wide application range. It can be observed that the ignition delay times predicted by 14D GQL reduced chemistry agree very well with those by detailed chemistry, and the overall relative errors are less than 6%.

In Fig.5.6 species concentrations (in specific mole number) for major and minor species from detailed chemistry (symbols) and 14D GQL reduced chemistry (solid lines) are compared in state space. Initial condition in this example is $T_0=1800$ K, $p_0=50$ bar and stoichiometric mixture composition. We observe that for all species, the 14D GQL reduced chemistry predicts the species concentration with good accuracy. The fact that the GQL reduced chemistry performs very well also demonstrates that the slow and fast subspace decomposition for optimal dimension does not change before and after ignition, although the chemical time-scales can change drastically before and after ignition.

5.2.5 Summary on the GQL approach

The Global Quasi-linearisation (GQL) approach for model reduction of chemical kinetics was discussed in this section. This approach allows a global analysis of the system hierarchy. It has a simple geometrical interpretation, namely linear mapping transforming state vectors into the system vector fields. This global linear transformation matrix can be used to identify the coordinate transformation to the system into a decomposed form and the fast and slow invariant subspaces. The GQL approach has some important features that makes it very efficient and attractive for application, namely:

- the global decomposition is found using invariant subspaces of the GQL matrix in the whole domain of interest of the state space;
- global slow and fast variables can be found for the whole domain of chemistry;
- both fast and slow subsystems can be treated by integration separately, which are less stiff compared to the original system.

5 MODEL REDUCTION FOR CHEMICAL KINETICS

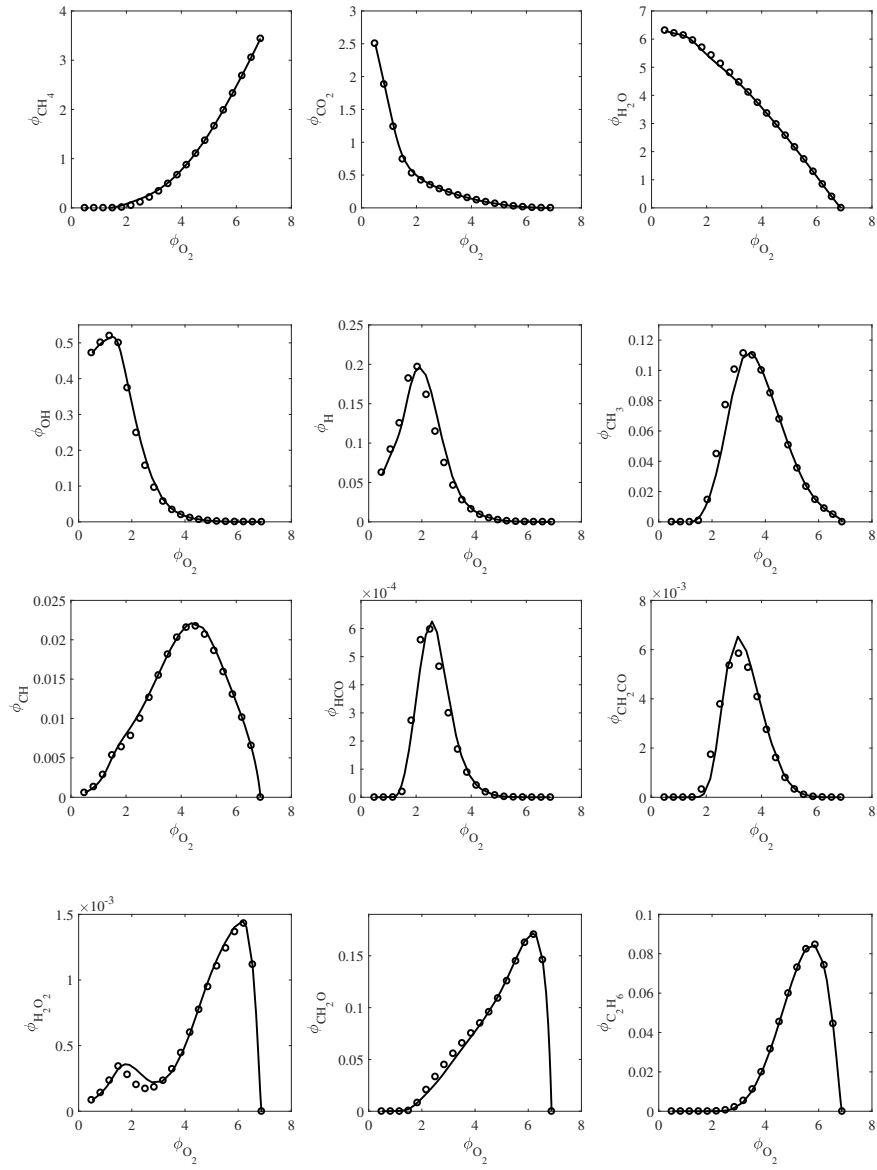


Figure 5.6: System state space in 2D projection. Comparison of the auto-ignition results from 14D GQL reduced chemistry (solid lines) and detailed chemistry (symbols) at $T_0=1800$ K, $p_0=50$ bar and stoichiometric condition in the state space.

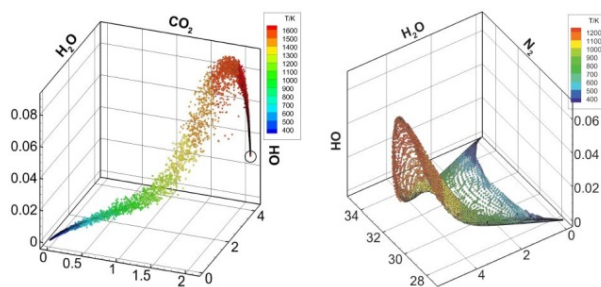


Figure 5.7: Distribution of composition states from DNS in 3D projection of composition state space. *Figure is taken from [63] with permission of the author.*

5.3 Reaction-diffusion manifolds (REDIM) for the model reduction with physical transport

Although the GQL approach is suitable for several important fuels such as methane [110], n-heptane [12] and methane/DME mixture [74], we notice that the reduced chemistry still has a relatively high dimension (e.g. 14 dimension for methane [110]). The reason is that one needs such high dimension to cover whole chemistry domain (e.g. initial ignition stage). Another weak point in the GQL approach is that the physical transports (e.g. convection and diffusion processes) are not considered for the model reduction. However, in most combustion system, physical processes such as convection and molecular transport exist and more fast time-scales can be decoupled from system.

In figure 2 two DNS results of premixed turbulent methane-air-flame (left) and non-premixed hydrogen-air counter-flow flame (right) in a 3D projection of state space [63] are shown. In both cases, chemistry and physical processes take place. We observe clearly that a much lower dimensional structure can be achieved if physical processes are considered. The reason for such structure is that there exist different characteristic time scales describing chemical and physical process in combustion systems. If one compares the time-scales of chemical reactions with typical physical time-scales caused by e.g. turbulent mixing or molecular transport, one can observe that most of chemical time-scales are much faster than physical time-scales, and only several chemical time-scales are needed to be considered.

In this section, we extend our considered reacting system to a system with physical transport, in which evolution of thermo-kinetic states described by a vector $\Psi = (h, p, \phi_1, \dots, \phi_{n_{sp}})^T$ of $n = n_{sp} + 2$ dimensions (h is the specific

enthalpy, p the pressure and ϕ_i is the specific mole fraction of species i) can be described as [35, 57] (see Eq.2.14):

$$\frac{\partial \Psi}{\partial t} = \mathbf{S}(\Psi) - \mathbf{u} \cdot \text{grad}(\Psi) + \frac{1}{\rho} \text{div}(\mathbf{D} \cdot \text{grad}(\Psi)) = \mathcal{R}(\Psi, \nabla \Psi, \nabla^2 \Psi) \quad (5.16)$$

Here, \mathbf{u} is the velocity, \mathbf{D} is the $n \times n$ -dimensional transport matrix, ρ the density and \mathbf{S} is the n -dimensional source term.

In order to reduce the dimensionality of the system given in Eq.5.16, an invariant manifold with a much lower dimension ($m_s \ll n$) needs to be constructed. This invariant manifolds can be written in an explicit form as:

$$\mathcal{M} = \{ \Psi : \Psi = \Psi(\theta), \Psi : R^{m_s} \rightarrow R^n \}, \quad (5.17)$$

where θ is the vector of reduced coordinates parametrizing this slow manifold.

In the following, the Reaction-Diffusion Manifolds (REDIM) method proposed in [10] as one of the methods to reduce chemical kinetics considering physical transports is discussed briefly.

5.3.1 REDIM theory and evolution equation

As proposed in [10], an invariant m_s -dimensional REDIM can be obtained, if one solves the following PDE system Eq.5.18 until its stationary state:

$$\frac{\partial \Psi(\theta)}{\partial t} = (\mathbf{I} - \Psi_\theta \cdot \Psi_\theta^\dagger) \cdot \left(\mathbf{S}(\Psi) - \mathbf{u} \cdot \text{grad}(\Psi) + \frac{1}{\rho} \text{div}(\mathbf{D} \cdot \text{grad}(\Psi)) \right), \quad (5.18)$$

where \mathbf{I} is the $(n \times n)$ -dimensional identity matrix. Ψ_θ is the matrix of partial derivatives of Ψ with respect to θ ($(\Psi_\theta)_{ij} = \partial \Psi_i / \partial \theta_j$). Mathematically the columns of Ψ_θ span the tangential subspace to the manifold. Ψ_θ^\dagger is a pseudo-inverse of Ψ_θ with the unity property $\Psi_\theta^\dagger \cdot \Psi_\theta = \mathbf{I}$. The $\mathbf{Pr}_s = \Psi_\theta \cdot \Psi_\theta^\dagger$ is a projection matrix for the vector field $\mathcal{R}(\Psi, \nabla \Psi, \nabla^2 \Psi)$ to be projected onto its tangential subspace, and the term $\mathbf{Pr}_f = \mathbf{I} - \Psi_\theta \cdot \Psi_\theta^\dagger$ for the vector field to be projected onto its normal space. Note that the pseudo-inverse matrix Ψ_θ^\dagger is not unique and additional conditions must be introduced, which will be discussed in detail in the next section.

Physically, the projection in the REDIM evolution equation Eq.5.18 is required to force the manifold evolution evolving to the invariant manifold of relatively slow motions, such that the normal component of the vector field on the invariant manifold vanishes [10, 35]. Furthermore, this projection term ensures that the invariant manifold does not shrink along the tangential subspace [33].

The Eq.5.18 can be further simplified and re-written as (details see [10]):

$$\frac{\partial \Psi(\theta)}{\partial t} = (\mathbf{I} - \Psi_\theta \cdot \Psi_\theta^+) \cdot \left\{ \mathbf{S}(\Psi(\theta)) + \frac{1}{\rho} [(\mathbf{D}\Psi_\theta \gamma(\theta))_\theta \gamma(\theta)] \right\}. \quad (5.19)$$

where $\gamma(\theta) = \text{grad}(\theta)$ is a gradient estimate with the assumption that it does not depend on space [10]. From this REDIM evolution equation, we notice that the REDIM evolution equation is only influenced by thermo-kinetic source term and molecular diffusion process. In other words, the convection process has no direct influence on invariant manifold. To show this issue, we project the convection term onto its normal component with projection operator $\mathbf{I} - \Psi_\theta \cdot \Psi_\theta^+$, and obtain:

$$(\mathbf{I} - \Psi_\theta \cdot \Psi_\theta^+) \cdot (\mathbf{u} \cdot \Psi_\theta \cdot \text{grad}(\theta)) = \mathbf{u} \cdot (\Psi_\theta \cdot \text{grad}(\theta) - \Psi_\theta (\Psi_\theta^+ \Psi_\theta) \cdot \text{grad}(\theta)) = 0. \quad (5.20)$$

This means that the convection term is already in the tangential direction of slow subspaces.

This REDIM evolution equation has several principle advantages:

- The reduced model takes into account coupled analysis of reaction and diffusion process.
- There is no principle restriction on the dimension, and a higher dimension of REDIM reduced chemistry can be generated in a generic way [33].
- This evolution equation for REDIM is a general expression without any simplification of chemistry or physical transport such as diffusion. Therefore, it works also for detailed molecular transport models [56].
- Little knowledge about the system behavior is required. For the counterflow diffusion flame, for example, one does not need to know the exact extinction stretch rate of flames. And this extinction stretch rate can still be predicted with good accuracy with REDIM reduced chemistry [112]. Furthermore, the transient behaviors can also be well predicted [14, 112].

5.3.2 Generation of REDIM reduced chemistry

In order to generate a REDIM reduced chemistry, one must solve the REDIM evolution equation 5.19 till its stationary solution ($t \rightarrow \infty$). In Fig.5.8,

a detailed procedure for the generation of REDIM reduced chemistry is summarized.

Since the REDIM evolution equation is a PDE system, one must specify the boundary condition and initial profile. Initial condition is less important, since one only interests in the steady solution of Eq.5.19. In other words, it does not matter which initial state one uses, the system will always evolve towards the slow manifold. However, a physically reasonable initial condition can lead to a faster convergence of REDIM evolution equation (Eq.5.19). The boundary condition defines the application regime of the generated REDIM reduced chemistry, which depends on the user specified problem definition.

Furthermore, in order to identify the REDIM, a suitable estimate of gradient $\gamma(\theta)$ has to be defined. In principle, there are three possibilities:

- The simplest way is to set constant values (e.g. $\text{grad}(\theta) = \text{const.}$). However, this might be inaccurate for low dimensions;
- One can also get gradients from typical flame scenarios ². In this way, gradient estimates represent the typical dynamics of combustion system. However, set of flamelet scenarios has to be chosen.
- The most accurate but comprehensive way is obtain gradients from DNS data, which represents real behavior of considered combustion system [55]. However, in this way one must performe DNS which is computationally expensive.

Although the gradient estimate affects the accuracy of REDIM reduced chemistry for low dimensions, it becomes less and less important for increasing dimension of reduced model [10, 33].

Additionally, one also needs to define number of grid points (N_{grid}) for the discretization of Eq.5.19. Afterwards, the discretized REDIM evolution equation 5.19 is integrated till its stationary solution.

The generated REDIM reduced chemistry (stationary solution of Eq. 5.19) is then used for the numerical simulation for flames. If the reduced results based on REDIM is convergent with increasing N_{grid} , then the REDIM is successfully generated. If not, one increases grid sizes N_{grid} again and the REDIM evolution equation with increased N_{grid} is integrated again. This loop is repeated until reduced results are convergent with increased N_{grid} .

²Here flame scenario means not only burning flames, but also other scenarios such as pure mixing processes, ignition processes, etc.

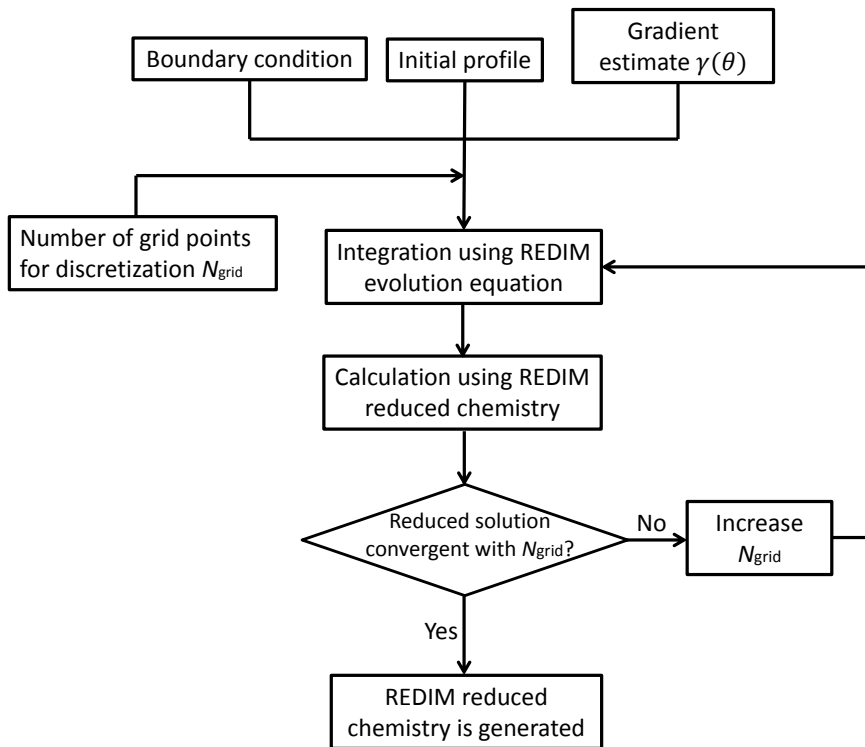


Figure 5.8: flow chart of generation of REDIM reduced chemistry.

5.3.3 Governing equations based on REDIM reduced chemistry

Recall that system Eq.5.16 represents the evolution of the full n -dimensional state Ψ in time and space. In the concept of manifold based simplified chemistry, this equation system contains redundant information, because Ψ can be parametrized by m_s variables θ with $m_s \ll n$ ($\Psi = \Psi(\theta)$). Therefore, one should change the equation system Eq.5.16 into a reduced equation system in terms of progress variables φ with m_s dimension.³ It is common

³Note that φ does not need to be necessarily selected equal to θ . Actually, they have different physical meanings:

- θ are used to parametrize the slow manifold describing the thermo-kinetic space $\Psi = \Psi(\theta)$;
- φ are used as progress variables describing the evolution of system progress in the reduced equation system (see Eq.5.24 and Eq.5.28 below).

to represent progress variables φ in terms of original species in the chemical kinetics:

$$\varphi = \mathbf{C}_\varphi \cdot \Psi, \quad (5.21)$$

where \mathbf{C}_φ is a parametrization matrix with the property:

$$\mathbf{I} = \mathbf{C}_\varphi \cdot \Psi_\varphi. \quad (5.22)$$

Here the parametrization matrix \mathbf{C}_φ is a constant (m_s by n)-dimensional matrix. If e.g. the thermo-kinetic state is listed as $\Psi = (h, p, \phi_{\text{N}_2}, \phi_{\text{H}_2\text{O}}, \phi_{\text{CO}_2}, \phi_{\text{O}}, \dots)^T$ and $\theta = (w_{\text{N}_2}, w_{\text{H}_2\text{O}} + w_{\text{CO}_2})^T$, then the corresponding parametrization matrix \mathbf{C}_φ is given by:

$$\mathbf{C}_\varphi = \begin{pmatrix} 0 & 0 & M_{\text{N}_2} & 0 & 0 & 0 & \dots \\ 0 & 0 & 0 & M_{\text{H}_2\text{O}} & M_{\text{CO}_2} & 0 & \dots \end{pmatrix} \quad (5.23)$$

After defining the progress variable φ according to Eq.5.21, the major target now is to change the equation system Eq.5.16 into an reduced equation system in terms of φ . In the following, two different ways are introduced and discussed.

VARIANT 1: Transforming with parametrization matrix \mathbf{C}_φ

Similar to the definition of φ via Eq.5.21, pre-multiplying the equation system Eq.5.16 with \mathbf{C}_φ then yields:

$$\begin{aligned} \frac{\partial \varphi}{\partial t} &= \mathbf{C}_\varphi \cdot \frac{\partial \Psi}{\partial t} \\ &= \mathbf{C}_\varphi \cdot \mathbf{S}(\Psi) - \mathbf{C}_\varphi \cdot \mathbf{u} \cdot \text{grad}(\Psi) - \frac{1}{\rho} \cdot \mathbf{C}_\varphi \cdot \text{div}(\mathbf{D} \cdot \text{grad}(\Psi)) \\ &= \mathbf{C}_\varphi \cdot \mathbf{S}(\Psi) - \mathbf{u} \cdot \text{grad}(\varphi) - \frac{1}{\rho} \cdot \mathbf{C}_\varphi \cdot \text{div}(\mathbf{D} \cdot \text{grad}(\Psi)). \end{aligned} \quad (5.24)$$

Although this approach is simple, the use of Eq.5.24 leads to an error, if a not perfectly invariant manifold is used. Furthermore, the accuracy of the reduced equation system is largely affected by the choice of parametrization matrix for φ . A systematic study can be found in [90]. Therefore, it is more essential to derive another way to allow an arbitrary parametrization matrix.

VARIANT 2: Projection of vector field $\mathcal{R}(\Psi, \nabla \Psi, \nabla^2 \Psi)$ onto manifold \mathcal{M}

As discussed in [52, 53, 79], all physical processes such as molecular transport can be viewed as perturbations of the reaction system. Geometrically, such

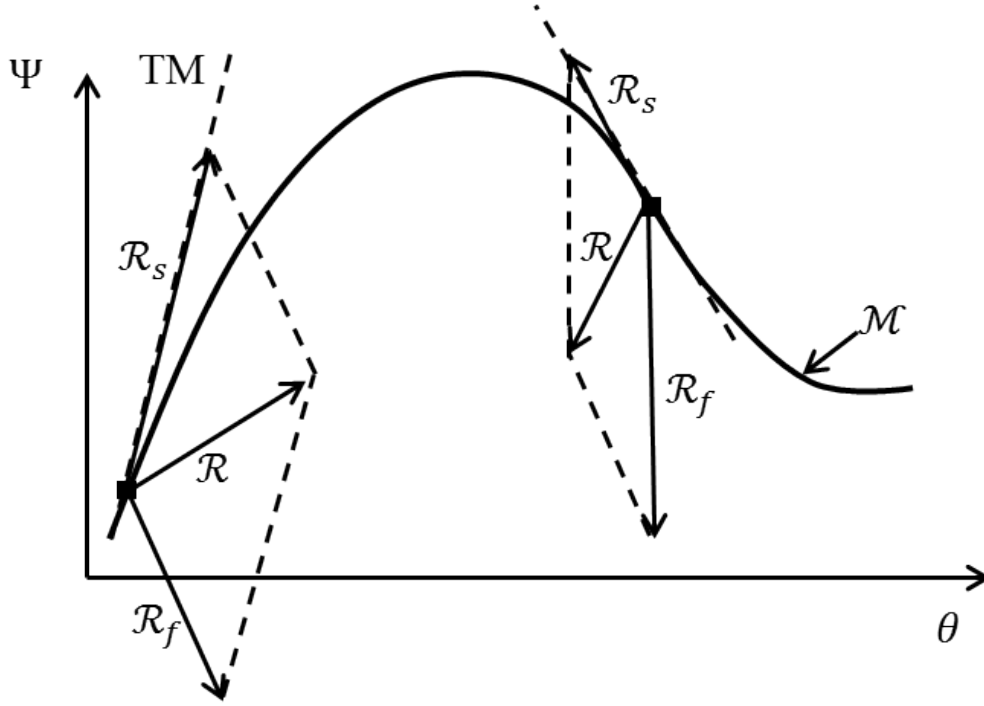


Figure 5.9: Schematic illustration of vector field $\mathcal{R}(\Psi, \nabla\Psi, \nabla^2\Psi)$ with physical processes considered as perturbation.

perturbations move the thermo-kinetic states off the manifold, which is schematically illustrated in Fig.5.9. Note that here and in the following content, a one-dimensional manifold is sketched to clarify the problem, but it can also be directly applied for manifolds with higher dimensions. Due to physical processes, the vector field $\mathcal{R}(\Psi, \nabla\Psi, \nabla^2\Psi)$ (right-hand side of Eq.5.16) might not be in the tangential subspace of manifold \mathcal{M} . This can be the case if the gradient estimate supplied to the REDIM integration equation ($\gamma(\theta)$ in Eq.5.19) is an estimated value [90].

However, one can decompose vector field into two parts, namely:

$$\mathcal{R}(\Psi, \nabla\Psi, \nabla^2\Psi) = \mathcal{R}_s(\Psi, \nabla\Psi, \nabla^2\Psi) + \mathcal{R}_f(\Psi, \nabla\Psi, \nabla^2\Psi), \quad (5.25)$$

where both parts have different physical meanings:

- $\mathcal{R}_s(\Psi, \nabla\Psi, \nabla^2\Psi)$ is the term projected onto the tangential subspace of slow manifold \mathcal{M} . This term describes the rate of change in the slow subspace and causes system state move along the slow manifold.

- $\mathcal{R}_f(\Psi, \nabla\Psi, \nabla^2\Psi)$ is the perturbation term causing system state depart from the slow manifold \mathcal{M} , and describes the rate of change in the fast subspace.

Usually the combustion system dynamics is governed by time-scales that differ from orders of magnitude [35, 57, 95], and time-scales controlling $\mathcal{R}_s(\Psi, \nabla\Psi, \nabla^2\Psi)$ are much smaller than those controlling $\mathcal{R}_f(\Psi, \nabla\Psi, \nabla^2\Psi)$ [52]. Hence all time-scales introduced by $\mathcal{R}_f(\Psi, \nabla\Psi, \nabla^2\Psi)$ are so fast that they do not couple with time-scales introduced by physical transport [52, 53]. Accordingly, the detailed equation system Eq.5.16 can be simplified if all fast time-scales are decoupled from the system, and the system dynamics is only governed by $\mathcal{R}_s(\Psi, \nabla\Psi, \nabla^2\Psi)$ controlled by slow time-scales:

$$\frac{\partial\Psi}{\partial t} = \mathcal{R}(\Psi, \nabla\Psi, \nabla^2\Psi) \approx \mathcal{R}_s(\Psi, \nabla\Psi, \nabla^2\Psi). \quad (5.26)$$

According to [10], term $\mathcal{R}_s(\Psi, \nabla\Psi, \nabla^2\Psi)$ can be determined using a projector $\mathbf{Pr}_s = \Psi_\theta \cdot \Psi_\theta^+$ onto the tangential subspace describing slow motion:

$$\frac{\partial\Psi}{\partial t} = \mathcal{R}_s(\Psi, \nabla\Psi, \nabla^2\Psi) = \Psi_\theta \cdot \Psi_\theta^+ \cdot \mathcal{R}(\Psi, \nabla\Psi, \nabla^2\Psi). \quad (5.27)$$

Equation 5.27 clearly shows that with the projector $\Psi_\theta \cdot \Psi_\theta^+$, the vector field $\mathcal{R}(\Psi, \nabla\Psi, \nabla^2\Psi)$ is projected onto the tangential subspace and the evolution of system dynamics is constrained in the slow manifold. In this case, an arbitrary parametrization matrix can be used to define progress variables φ , and the system is not sensitive to the parametrization matrix \mathbf{C}_φ any more. Pre-multiplying the Eq.5.27 with \mathbf{C}_φ yields again a reduced equation system in terms of progress variable φ :

$$\begin{aligned} \frac{\partial\varphi}{\partial t} &= \mathbf{C}_\varphi \cdot \frac{\partial\Psi}{\partial t} \\ &= \mathbf{C}_\varphi \cdot \Psi_\theta \cdot \Psi_\theta^+ \cdot \mathcal{R}(\Psi, \nabla\Psi, \nabla^2\Psi) = \Pi \cdot \mathcal{R}(\Psi, \nabla\Psi, \nabla^2\Psi) \\ &= \Pi \cdot \left(\mathbf{S}(\Psi) - \mathbf{u} \cdot \text{grad}(\Psi) + \frac{1}{\rho} \text{div}(\mathbf{D} \cdot \text{grad}(\Psi)) \right) \\ &= \hat{S}(\varphi) + \Pi \cdot \left(-\mathbf{u} \cdot \text{grad}(\Psi) + \frac{1}{\rho} \text{div}(\mathbf{D} \cdot \text{grad}(\Psi)) \right) \end{aligned} \quad (5.28)$$

From Eq.5.28 we observe that the thermo-kinetic source term is described dependent on progress variable φ , while the physical processes should be calculated in full state space. The term $\Pi = \mathbf{C}_\varphi \cdot \Psi_\theta \cdot \Psi_\theta^+$ serves as a projection operator that only tangential components of physical processes are calculated.

If the REDIM is parametrized using progress variables, say $\varphi = \theta$, the projection operator Π can be further simplified:

$$\Pi = \mathbf{C}_\varphi \cdot \Psi_\theta \cdot \Psi_\theta^+ = \Psi_\varphi^+. \quad (5.29)$$

Note that here no restriction to the kind of physical processes has been made. Such physical processes can also be e.g. mixing processes in turbulence simulations, where diffusion processes are modeled in a different way from the one in Eq.5.16 (details see chapter 6.2 later).

5.3.4 Projection process

As mentioned above, physical processes serve as perturbations tending to move the system off the slow manifold, and the fast chemical processes cause a relaxation of the system back to the manifold. However, there is still one important question: how the fast process $\mathcal{R}_f(\Psi, \nabla\Psi, \nabla^2\Psi)$ should be defined? This is schematically illustrated in Fig.5.10, where two different projection processes (colored by blue and red) are sketched. Although the component \mathcal{R}_s is in the tangential subspace of manifold \mathcal{M} , the component \mathcal{R}_f can be defined in different directions, describing different rates of change in the fast subspaces.

Such various definition of \mathcal{R}_f can be attributed to the definition of pseudo-inverse matrix Ψ_θ^+ . Recall that any matrix Ψ_θ^+ , which fulfils the condition $\Psi_\theta^+ \cdot \Psi_\theta = \mathbf{I}$ can be used for the projection $\mathbf{Pr}_s = \Psi_\theta \cdot \Psi_\theta^+$. In general, any pseudo-inverse defined in Eq.5.30 can be used:

$$\Psi_\theta^+ = (\mathbf{X}(\theta) \cdot \Psi_\theta)^{-1} \cdot \mathbf{X}(\theta), \quad (5.30)$$

where $\mathbf{X}(\theta)$ can be any $(m_s$ by $n)$ -dimensional matrix depending on reduced coordinate θ which parametrize the manifold \mathcal{M} , and are the basis spanning the slow subspace. In the following, two different projection algorithms, corresponding to the definition of \mathbf{X} in Eq.5.30, are proposed and their physical significances will be clarified through Fig.5.11.

Variant 1: Projection perpendicular to slow subspaces: $\Pi_{Z_s}^\perp$

The first variant is to define an $(m_s$ by $n)$ -dimensional constant matrix \mathbf{C} , so that the pseudo-inverse matrix according to Eq.5.30 reads:

$$\Psi_\theta^+ = (\mathbf{C} \cdot \Psi_\theta)^{-1} \cdot \mathbf{C}. \quad (5.31)$$

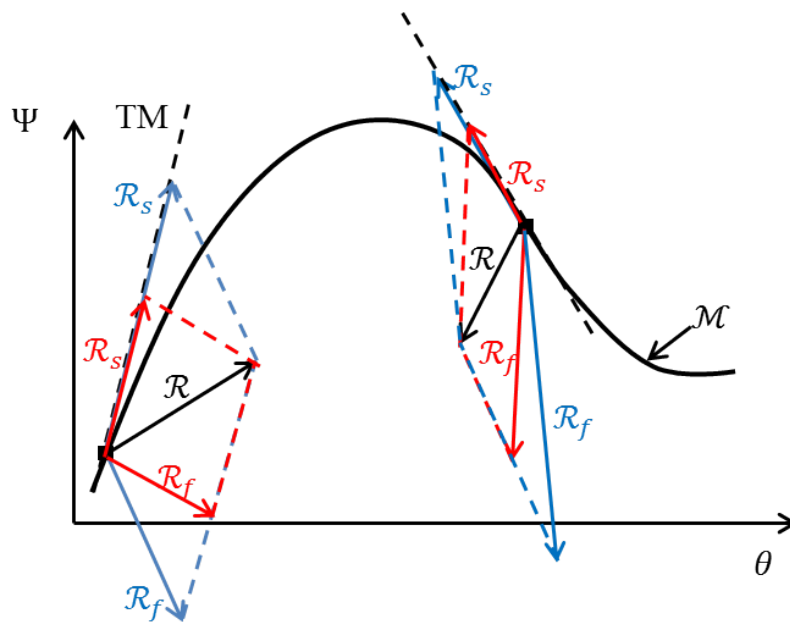


Figure 5.10: Schematic illustration of different projection processes as example.

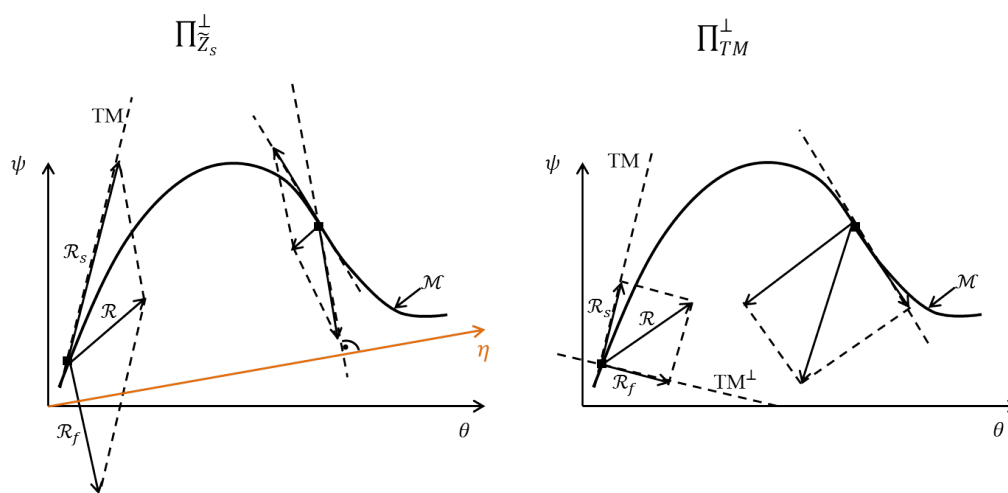


Figure 5.11: Illustration of two projection processes: Left ($\Pi_{\tilde{Z}_s}^\perp$): Projection perpendicular to slow subspaces; Right (Π_{TM}^\perp): Projection perpendicular to tangential subspace of manifold.

It can be easily shown that this definition satisfies both the unity property ($\Psi_\theta^+ \cdot \Psi_\theta = \mathbf{I}$) and the following additional condition:

$$\mathbf{C} \cdot (\mathbf{I} - \Psi_\theta \cdot \Psi_\theta^+) = 0, \quad (5.32)$$

indicating that after projecting a vector onto the tangential subspace of the manifold, its coordinates using matrix \mathbf{C} do not change [33], which is illustrated in Fig.5.11 left titled with $\Pi_{\tilde{Z}_s}^\perp$. Say $\mathbf{C} = \tilde{Z}_s$ to be used in Eq.5.31, which \tilde{Z}_s is used to define variables $\eta = \tilde{Z}_s \cdot \Psi$. Then in this case, the normal component of vector field is perpendicular to the η axis, and the system is relaxed back onto the slow manifold in direction that variables η remain constant. It is obvious that the directions of the term $\mathcal{R}_f(\Psi, \nabla\Psi, \nabla^2\Psi)$ have to correspond to the direction of fast subspace of system 5.16, which can be investigated by using the GQL method, and it is suitable to define variables η as slow variables \mathcal{U} . This will be explained in details in Sec.6.2.

Variant 2: Projection perpendicular to the tangential subspace of manifold: Π_{TM}^\perp

The second variant is to determine the Ψ_θ^+ using the modified Moore-Penrose pseudo-inverse [34] as:

$$\Psi_\theta^+ = (\Psi_\theta^T \cdot \mathcal{S} \cdot \Psi_\theta)^{-1} \cdot \Psi_\theta^T \cdot \mathcal{S}, \quad (5.33)$$

where \mathcal{S} is a regular scaling matrix. Since enthalpy h and pressure p in thermo-kinetic state vector Ψ are several orders of magnitude larger than specific mole numbers of species ϕ_i ($i = 1, 2, \dots, n_{sp}$), the scaling matrix used here is to perform a scaling of values for the thermo-kinetic states so that these values are in the same order of magnitude. If thermo-kinetic state vector is expressed as $\Psi = (h, p, \phi_i)^T$, then the regular scaling matrix can set to be:

$$\mathcal{S} = \begin{pmatrix} 10^{-12} & 0 & 0 \\ 0 & 10^{-12} & 0 \\ 0 & 0 & \frac{1}{\max(\phi_i)^2} \end{pmatrix}, \quad i = 1, 2, \dots, n_{sp} \quad (5.34)$$

The physical significance using Eq.5.33 is illustrated in Fig.5.11 right. Using the Moore-Penrose pseudo-inverse, the fast process is embended in the fast subspaces spanned by $(\Psi_\theta^T)^\perp$, which is perpendicular to the tangential subspace of slow manifold. In other words, the vector field \mathcal{R} splits into fast and slow parts, which are perpendicular to each other: $\mathcal{R}_s \cdot \mathcal{R}_f = 0$. And the system state is projected back onto the slow manifold in normal direction.

Unlike the variant 1 that an optimal direction of fast relaxation is required to define *a priori*, using orthogonal projection process needs no additional information.

5.3.5 2D REDIM approach for a counterflow diffusion flame CH₄-Air system

In this section, the performance of REDIM for a counterflow diffusion flame CH₄-Air system will be discussed. The main aim of this part is to show that REDIM is able to capture both steady and non-steady behavior, and thus suitable for the simulation of turbulent flames.

As example, we consider an important flame configuration: counterflow diffusion flames. The following boundary conditions have been chosen, which correspond to the well-known Sandia Flame [4]

- Left boundary: mixture composition: 25% CH₄+75% air; $p = 1$ bar; $T = 292$ K;
- Right boundary: mixture composition: 100% air; $p = 1$ bar; $T = 294$ K.

In the following calculation, a unity Lewis number is assumed because it is a reasonable simplification and is also applied in many numerical simulations [47, 68, 69, 84]. For this counterflow flames, the quenching limit based on detailed chemistry equals to $a = 651s^{-1}$.

Generation of REDIM reduced chemistry

Figure 5.12 shows the numerical setup for the construction of the corresponding REDIM according to the procedure discussed in Fig.5.8. For the boundary condition (shown in left figure), we simply take two stationary solutions. The upper boundary is the stationary solution with very low strain rate $50 s^{-1}$, and the lower boundary is defined by pure mixing line (inert counterflow diffusion solution). This boundary encloses all possible strain rates and also extinction regimes in the following study. Furthermore, both boundaries are set as Dirichlet boundary.

For the initial profile and gradient estimation, we simply arbitrarily use three additional stationary flamelets (with strain rates 200, 400 and $600 s^{-1}$). Then states for the whole range is linear interpolated, which is shown in middle figure for initial guess. The reduced coordinate $\theta = (\theta_1, \theta_2)^T = (N_2, CO_2)^T$ is used here. The integration of REDIM evolution equation to its stationary

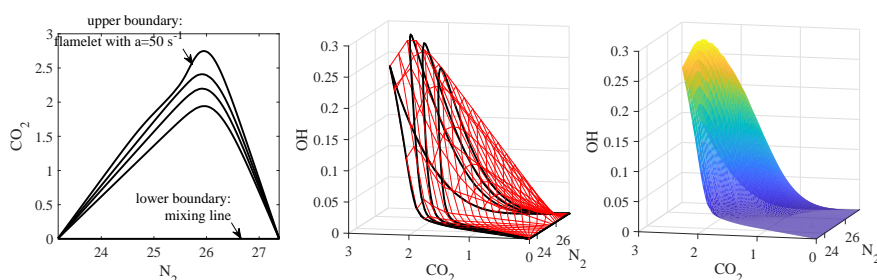


Figure 5.12: Implementation of REDIM reduced chemistry. Figure from [112].

solution results in REDIM reduced chemistry, which is shown in right figure in Fig.5.12.

From a numerical viewpoint, the accuracy of REDIM also depends on the grid resolution, which is illustrated in Fig.5.13. The temperatures and mass fractions of OH at stoichiometric mixture fraction position against different grids N_{grid} are plotted for four different strain rates. It can be observed that REDIM with coarse grid (e.g. $N_{\text{grid}} = 40 \times 40$ or 60×60) can predict good results for small and moderate strain rates (here $a = 200$ and $500s^{-1}$), but lead to extinction results for strain rates close to quenching limit (here $a = 600$ and $648s^{-1}$). In order to guarantee the performance of REDIM even close to quenching limit, one must use REDIM with sufficient fine grid (e.g. $N_{\text{grid}} = 100 \times 100$ or more). Furthermore, one notices that the quantities predicted by REDIM with $N_{\text{grid}} = 100 \times 100$ are mostly equal to those predicted by REDIM with $N_{\text{grid}} = 140 \times 140$, showing that for REDIM up $N_{\text{grid}} = 100 \times 100$ quantities is convergent to constant values with increasing grid numbers.

REDIM reduced chemistry for steady flamelets

In Fig.5.14 temperatures and mass fractions of OH and HCCO at stoichiometric mixture fraction over different strain rates up to quenching limit are plotted for comparison of detailed chemistry and REDIM reduced chemistry. We notice that for strain rates close to quenching limit some deviations can be observed, while at small strain rates negligible deviations are observed. It should be mentioned again that in the generation of REDIM reduced chemistry, the gradient estimation we gave into the REDIM evolution equation is a rough estimation. If one uses a more detailed gradient estimation especially close to quenching limit, one can get more accurate results for flame structure with strain rates close to quenching limit.

5 MODEL REDUCTION FOR CHEMICAL KINETICS

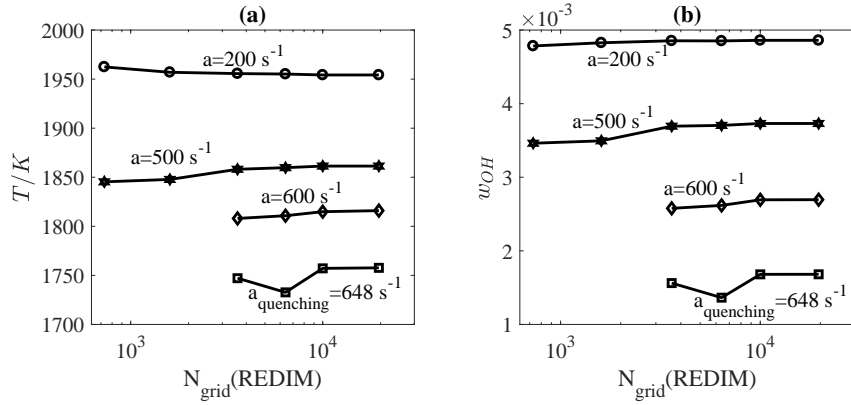


Figure 5.13: Grid sensitivity of temperatures (left) and mass fraction of OH (middle) for different strain rates. Figure from [112].

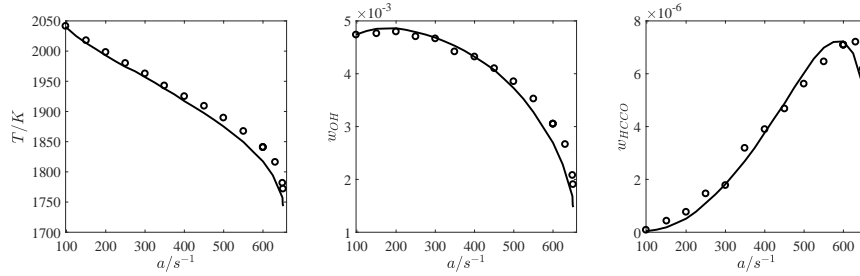


Figure 5.14: Temperatures (left), mass fractions of OH (middle) and HCCO (right) over strain rates based on detailed chemistry (symbols) and REDIM reduced chemistry (solid lines). Figure from [112].

In Fig.5.15 we show profiles of different thermo-kinetic quantities over mixture fraction for three different strain rates: $a = 100s^{-1}$ for low strain rate, $a = 400s^{-1}$ for moderate strain rate and $a = 600s^{-1}$ for high strain rate close to quenching limit ($a = 651.78s^{-1}$). It is observe clearly that for high strain rate we can observe some deviations, while for low and moderate strain rates the profiles predicted by REDIM agree very well with those by detailed chemistry.

5.3 REACTION-DIFFUSION MANIFOLDS (REDIM) FOR THE MODEL REDUCTION WITH PHYSICAL TR

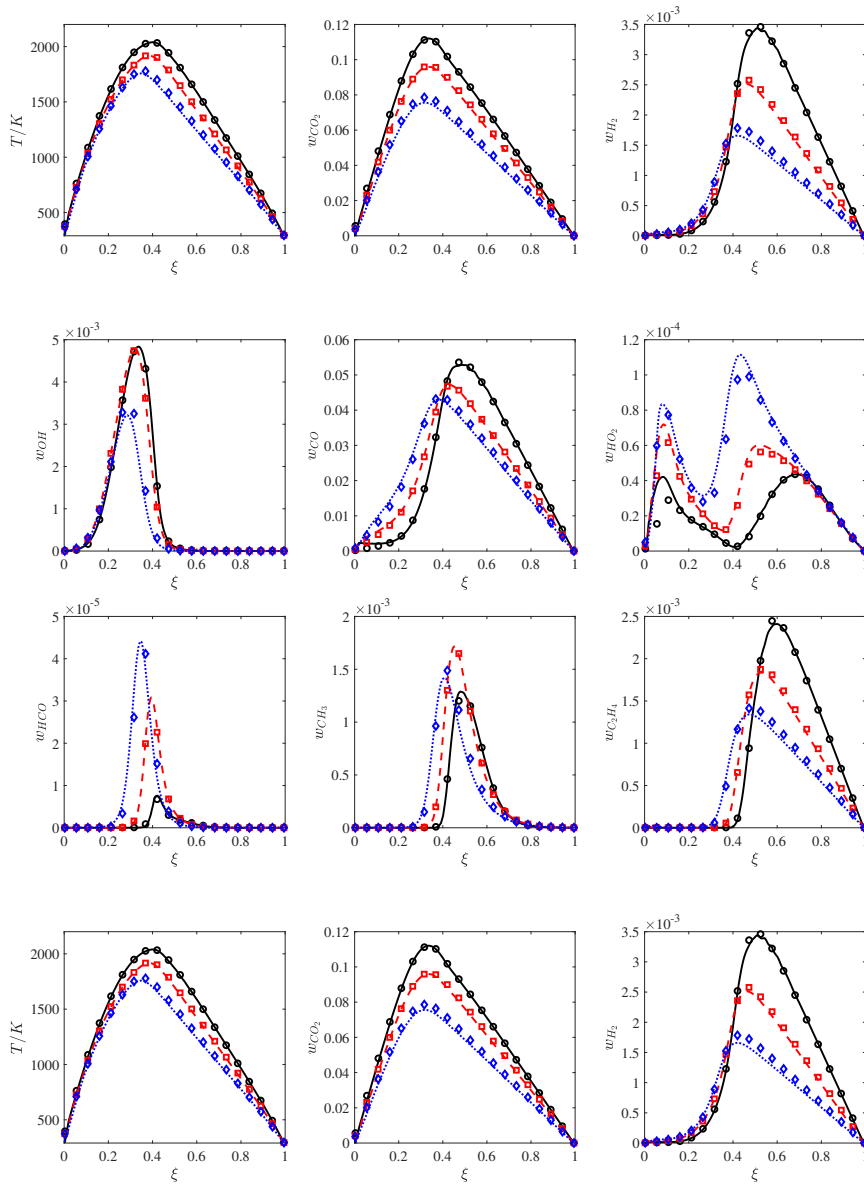


Figure 5.15: Thermo-kinetic quantities over mixture fractions for strain rates $a = 100 \text{ s}^{-1}$ (black), $a = 400 \text{ s}^{-1}$ (red), and $a = 600 \text{ s}^{-1}$ (blue). Symbols: detailed chemistry; Lines: 2D REDIM reduced chemistry;

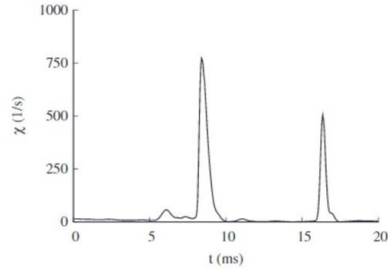
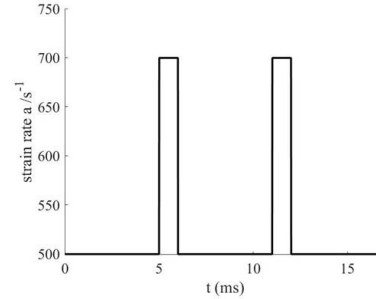
Real behavior in turbulent**Modeled behavior**

Figure 5.16: Left: intermittent nature of scalar dissipation field in turbulent flow. Figure from [2]; Right: modeled strain rate perturbation as pulse function.

REDIM for counterflow diffusion flames with strain rate perturbation as pulse function

So far, the performance of REDIM has been validated for laminar counterflow flames with constant strain rates. However, in turbulent non-premixed flames, the strain rate (or equivalently the scalar dissipation rate) undergoes an intermittent turbulent nature, which is shown as example in Fig.5.16 left [2]. As observed, scalar dissipation rate can change in rapid bursts that may vary from low to extremely high values. Therefore, such intermittent character plays an important role for turbulent flames concerning modeling the turbulence-chemistry interaction.

In order to check whether REDIM can capture such intermittent nature in turbulent flows, the strain rate of studied flame system is perturbed according to a pulse function, which is similar to the real behaviors in turbulent flows. The pulse width in our simulation is 1 ms, which is in the same order of the width in Fig.5.16 left. Strain rate is perturbed stepwise between 500s^{-1} and 700s^{-1} starting at $t \geq 5\text{ms}$, so that the maximum of strain rate exceeds quenching limit.

Figure 5.17 shows the comparison of predicted temperature and mass fractions of OH, CO and CH_3 at stoichiometric mixture fraction using both REDIM reduced chemistry (blue lines) and detailed chemistry (red lines). It is clearly observed that REDIM reduced chemistry can also predict such behavior quite well, with the only minor deviations where peak values are

5.3 REACTION-DIFFUSION MANIFOLDS (REDIM) FOR THE MODEL REDUCTION WITH PHYSICAL TR

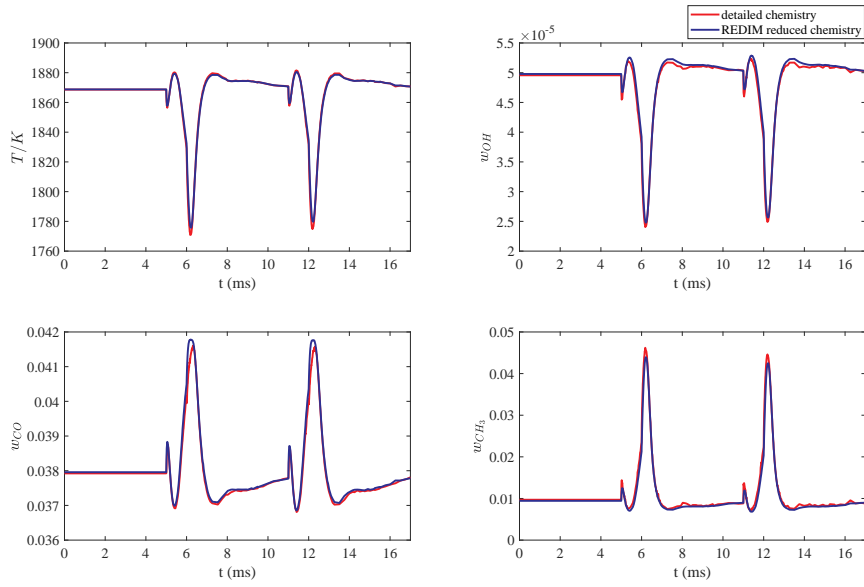


Figure 5.17: Response of selected thermo-kinetic quantities at stoichiometric mixture fraction to the perturbed strain rates. Blue lines: REDIM reduced chemistry. red lines: detailed chemistry.

reached. Therefore, it is believed that the REDIM reduced chemistry can predict thermo-kinetic quantities very well, if strain rate changes suddenly as observed in turbulent flames.

5.3.6 Summary on the REDIM approach

In this section, the concept of Reaction-Diffusion Manifolds (REDIMs) was briefly discussed. If the vector field is the in the tangential subspace of REDIM manifold, a projection must be considered, which was discussed in details. Since the REDIM takes physical transport (e.g. convection and molecular diffusion) into account, a much lower dimension of reduced chemistry (usually two-dimensional or three dimensional) is sufficient. Its application in CH_4 combustion system also shows that the REDIM reduced chemistry can predict thermo-kinetic quantities very well, if strain rate changes suddenly as observed in turbulent flames (e.g. intermittency). Therefore, the REDIM can be further employed into turbulent flame calculation.

6 Hybrid Finite-Volume/ Transported-PDF Method Based on REDIM Reduced Chemistry

As mentioned in Section 3.3, methods solving RANS have the disadvantages with respect to unclosed averaged Reynolds stresses and thermo-chemical source term [27, 70, 72]. Traditional models, such as two-equation models (e.g. $k - \epsilon$ model) for unclosed averaged Reynolds stresses and Eddy Breakup model for thermo-chemical source term, are applicable for some specific cases. In comparison with these traditional models, PDF method achieves closure through a transported-PDF equation for the one-point, one time PDF in a turbulent flow [38, 73]. The PDF method has the significant advantage that both unclosed averaged Reynolds stresses and thermo-chemical source term are solved exactly without any modeling [27, 38, 73].

The numerical calculation using detailed chemistry for turbulent reacting flows is not easily feasible because of the high dimension and the high stiffness of the governing PDE system [35, 57, 95]. Therefore, the reduced chemistry is used, aiming at reducing the dimension and stiffness of system which keeping accuracy sufficiently high for reliable results.

In this chapter, a hybrid algorithm which is a combination of a Finite-Volume Method (FVM), transported-PDF solved using particle method, and REDIM as reduced chemistry is discussed. The hybrid algorithm is outlined in Section 6.1. And the coupling strategies between manifold based simplified chemistry and mixing processes in PDF method is addressed and methodologies are suggested in Section 6.2.

6.1 Outline of hybrid algorithm

In Fig. 6.1 the hybrid algorithm is represented. At the beginning, the Finite-Volume Method (FVM) code and the particle method code are initialized.

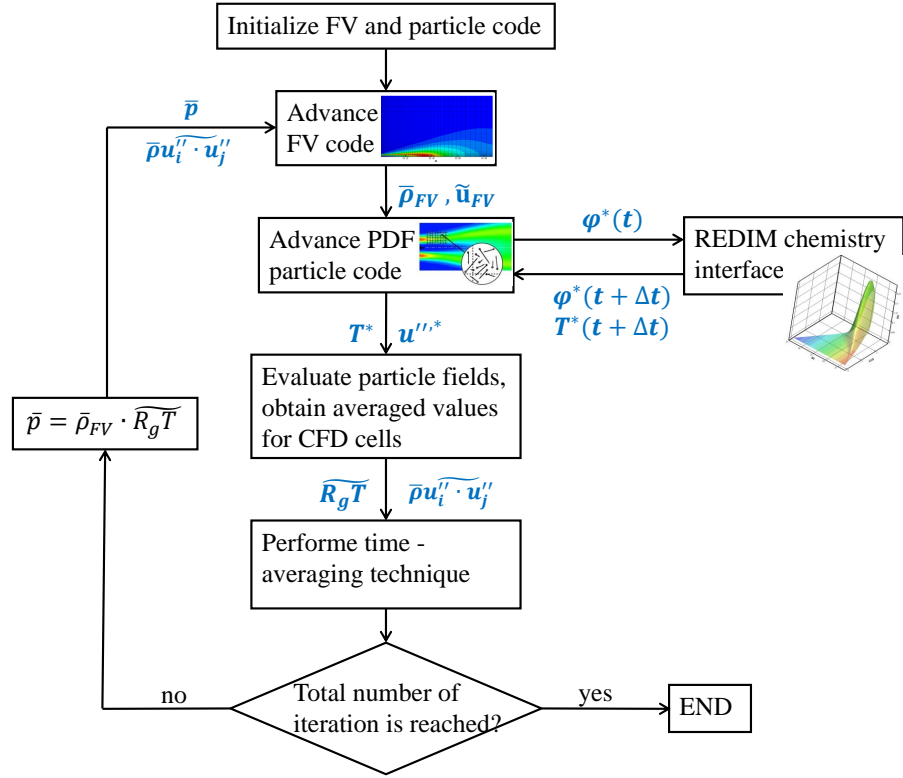


Figure 6.1: Flow chart of hybrid FV/transported-PDF method coupled with REDIM reduced chemistry.

At this step, the user-defined initial conditions and boundary conditions are imported into the code. Then the FVM is performed to obtain the Favre-averaged density $\bar{\rho}_{FV}$ (from Favre-averaged mass conservation equation Eq.3.14) and velocity \tilde{u}_{FV} (from Favre-averaged momentum conservation equation Eq.3.15) for each CFD cell, which are fed into the PDF particle code. In the particle method calculation, each CFD cell contains a certain number of particles N_p . Each particle evolves in physical space \mathbf{X}^* , in the velocity fluctuation space \mathbf{u}''^* , in the turbulent frequency space ω^* and in the progress variable space φ^* ¹. In order to evaluate the evolution of particles in the progress variable space, progress variables of each particle φ^* at time level t are fed into REDIM reduced chemistry code, and the temperature T^* and progress variables φ^* at time level $t + \Delta t$ are calculated and fed back to PDF particle code. After the PDF particle method code is performed,

¹Note that due to the evolution of particles in physical space, particles can leave their original cells and enter new cells. In this case, they will be assigned to new cells

velocity fluctuation \mathbf{u}''^* and temperature T^* of each particle are obtained. Those particles sharing the same CFD cell are used to calculate the favre-averaged Reynolds stresses $\overline{\rho u_i'' u_j''}$ and temperature $\overline{R_g \cdot T}$ for this CFD cell. Afterwards, a time-averaging technique (Sec. 7.3.2) is applied for all favre-averaged quantities to reduce the statistical and bias error, and enhance the stability of numerical calculation for $\tilde{\mathbf{u}}_{\text{FV}}$ in FVM. Then the updated time-averaged temperature $\overline{R_g \cdot T}$ is used for the determination of averaged pressure via ideal gas law:

$$\bar{p} = \bar{\rho}_{\text{FV}} \cdot \overline{R_g \cdot T}. \quad (6.1)$$

Equation 6.1 indicates that no poisson equation [26, 72] for the pressure has to be solved. This calculated \bar{p} and updated time-averaged (using time-averaging technique) Reynolds stresses $\overline{\rho u_i'' u_j''}$ are fed into FVM code for the next iteration. This loop is repeated until the maximal number of iteration step is reached.

A more detailed description can be found in [89]. In Chapter 7 numerical implementation for the whole hybrid algorithm involving FVM and Monte Carlo particle method in the PDF calculation will also be discussed in details.

6.2 Coupling of reduced chemistry with mixing processes in PDF method

For the particle mixing and reaction, the following equation is integrated at each time step from t_n to t_{n+1} :

$$\frac{d\Psi^*}{dt} = \mathbf{M}(\Psi^*) + \mathbf{S}(\Psi^*), \quad (6.2)$$

where \mathbf{M} is mixing process and \mathbf{S} reaction process. However, if manifold based simplified chemistry is applied, one only needs information about progress variables φ so that all other thermo-kinetic quantities can be extracted since $\Psi = \Psi(\varphi)$. Therefore, instead of calculating evolution of full thermo-kinetic quantities Ψ , only evolution of progress variables φ is necessarily needed to be determined:

$$\frac{d\varphi^*}{dt} = \hat{\mathbf{M}} + \hat{\mathbf{S}}, \quad (6.3)$$

where $\hat{\mathbf{M}}$ and $\hat{\mathbf{S}}$ are mixing and reaction processes related to progress variables φ . In this section, the coupling of manifold based simplified chemistry with

mixing processes in PDF method is discussed, and two different coupling strategies are introduced.

In the concept of manifold based simplified chemistry, it is assumed that the thermo-kinetic states at any time and at any point in the flow are restricted on an attracting low-dimensional slow manifold \mathcal{M} [10, 35, 52, 53, 57]. However, as already discussed in Sec. 5.3.3 and Sec. 5.3.4, perturbations due to e.g. molecular transport cause system states moving off this slow manifold \mathcal{M} , and a projection of thermo-kinetic state back onto slow manifold \mathcal{M} is needed, which couples the processes between transport processes and manifold based simplified chemistry. The importance and algorithm of projection process in Sec. 5.3.3 and Sec. 5.3.4 are discussed in a general way, and in this section projection process will be intensively discussed in the context of PDF method solving following several important questions:

- Why is coupling between turbulent mixing process and manifold based simplified chemistry so important?
- How can turbulent mixing process and manifold based simplified chemistry be coupled with each other?

Let us first focus on the stochastic mixing process in the full thermo-kinetic state space in the PDF particle method, which is illustrated in Fig.6.2. In the mixing processes, two states are selected and mixed with each other (Step 1), leading to states away from the slow manifold (Step 2). Since the evolution of system dynamics is constrained to a movement only in the tangential subspace of the slow manifold, a projection of the thermo-kinetic states away from the slow manifold is required to relax back onto the manifold (arrows in Step 3). After states are relaxed back onto slow manifold, all states are located again on the slow manifold (Step 4).

In Sec. 5.3.3 and Sec. 5.3.4, the governing equation for progress variables φ ($\varphi = \mathbf{C}_\varphi \cdot \Psi$) and the definition of pseudo-inverse matrix Ψ_θ^+ for projection process are derived in a general way, and thus can be also applied for the evolution of progress variables of each particle φ^* :

$$\frac{\partial \varphi^*}{\partial t} = \Pi \cdot (\mathbf{S}^* + \mathbf{M}^*),$$

with projection matrix: $\Pi = \mathbf{C}_\varphi \cdot \Psi_\theta \cdot \Psi_\theta^+$. (6.4)

Now the definition of Ψ_θ^+ and physical significants for corresponding projection process in the content of mixing processes coupled with manifold based simplified chemistry will be discussed according to the concept in Sec.5.3.4.

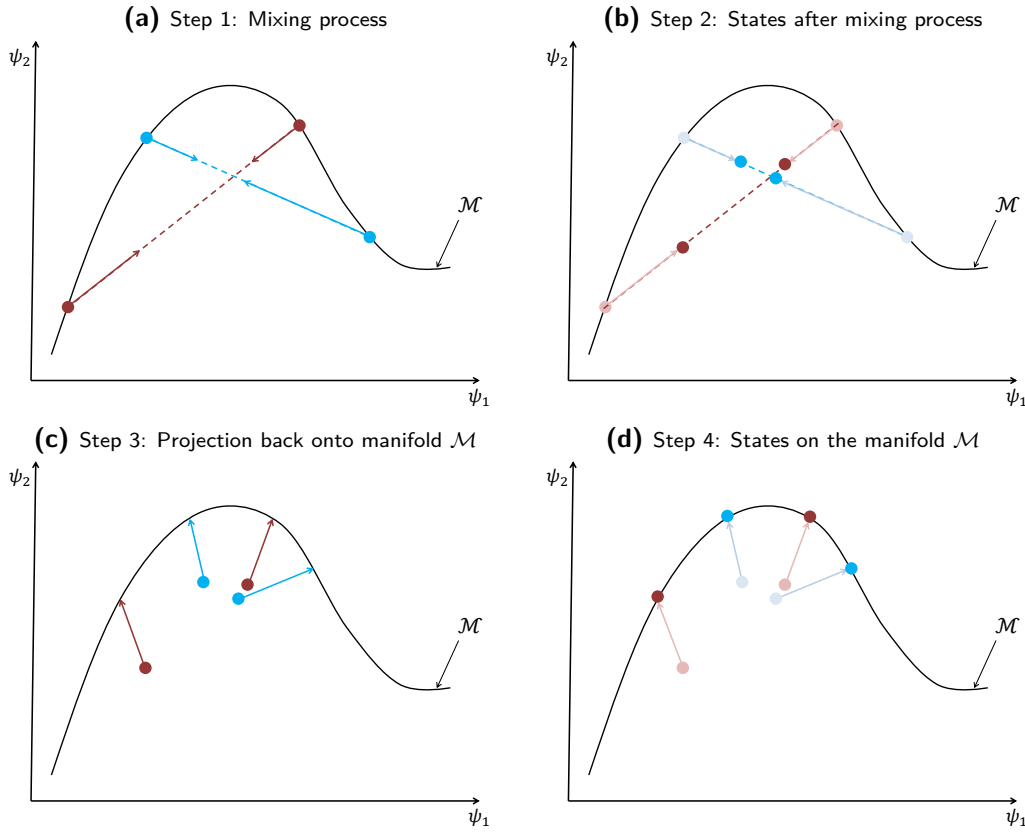


Figure 6.2: Stochastic mixing process and its behavior with respect to slow manifold.

6.2.1 Coupling based on projection perpendicular to slow subspaces

As discussed in Sec.5.3.4, if Ψ_θ^+ is defined as:

$$\Psi_\theta^+ = (\mathbf{C}_\eta \cdot \Psi_\theta)^{-1} \cdot \mathbf{C}_\eta, \quad \text{with parametrization matrix } \mathbf{C}_\eta \text{ as: } \eta = \mathbf{C}_\eta \cdot \Psi, \quad (6.5)$$

it means that the system states which are located away from the slow manifold \mathcal{M} are projected back onto the manifold in the direction where variables η remain constant, which corresponds to the variant $\Pi_{Z_s}^\perp$ in Fig.5.11 left and is illustrated in Fig.6.3 related to mixing processes in PDF particle method. After the mixing processes, thermo-kinetic states are away from the slow manifold. Then these states are projected back onto slow manifold in the direction perpendicular to η -axis.

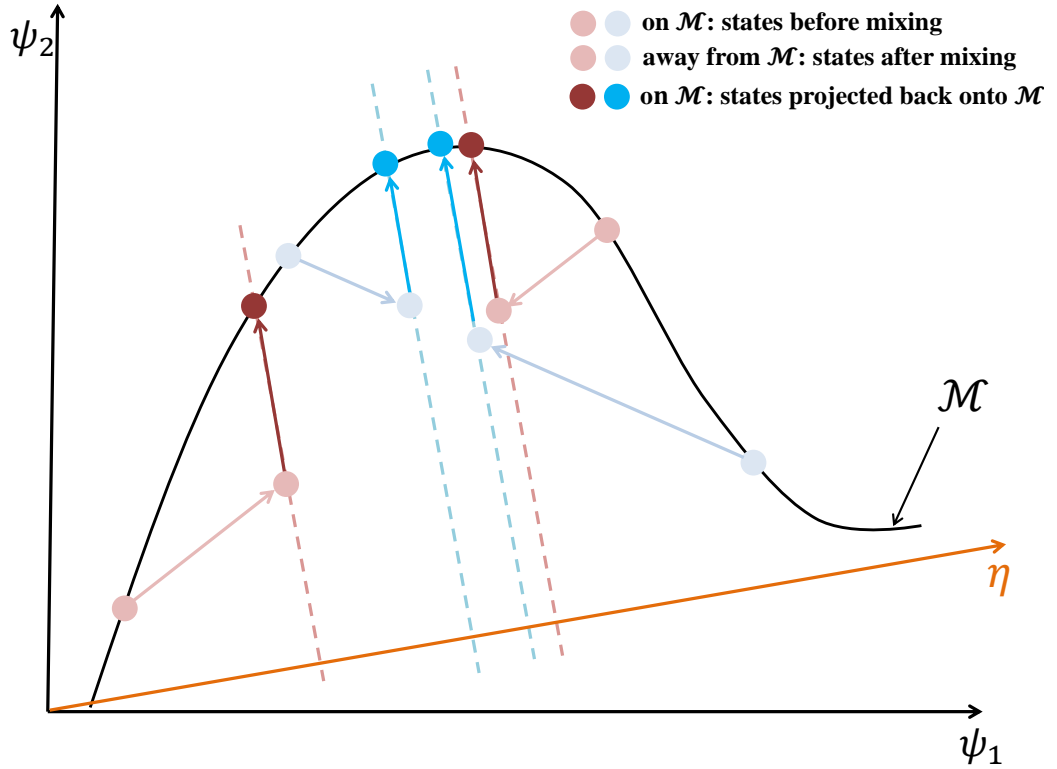


Figure 6.3: Illustration for coupling strategy between mixing process and manifold based simplified chemistry based on projection perpendicular to slow subspaces.

Nevertheless, since the reacting system consists of a large number of species, \mathbf{C}_η is extremely difficult to be found out empirically and meanwhile ensures that this projection direction is compatible with fast relaxation processes. However, two important approximations can be considered for this problem:

- During the fast relaxation process, physical transport can be assumed as frozen [51, 111], and the convection-diffusion-reacting system on the fast relaxation stage can be approximated to a pure homogeneous reacting system [111].
- Thermo-kinetic states are relaxed approximately parallel back onto the slow manifold [111], which can also be observed in Fig.5.1.

Based on both approximations, the Global Quasi-linearization (GQL) discussed in Sec.5.2 is a suitable tool. As mentioned in Sec. 5.2, slow subspace $\tilde{\mathcal{Z}}_s$ is used for the determination of slow variables that do not change during fast motion. Therefore, one can define $\mathbf{C}_\eta = \tilde{\mathcal{Z}}_s$ in Eq.6.5.

6.2.2 Coupling based on projection perpendicular to tangential subspace of manifold

Another variant of projection process discussed in Sec.5.3.4 is to define Ψ_θ^+ using *Moore-Penrose* pseudo inverse strategy:

$$\Psi_\theta^+ = (\Psi_\theta^T \cdot \Psi_\theta)^{-1} \cdot \Psi_\theta^T, \quad (6.6)$$

it means that the system states which are located away from the slow manifold \mathcal{M} are projected back onto the manifold in the direction which is perpendicular to the tangential space of slow manifold.

This projection process is illustrated schematically in Fig.6.4. After mixing processes, states are away from the slow manifold, and projected back onto manifold in direction characterized by TM^\perp . Note that in this case, projection direction depends on reduced coordinates θ and must be evaluated for each particle.

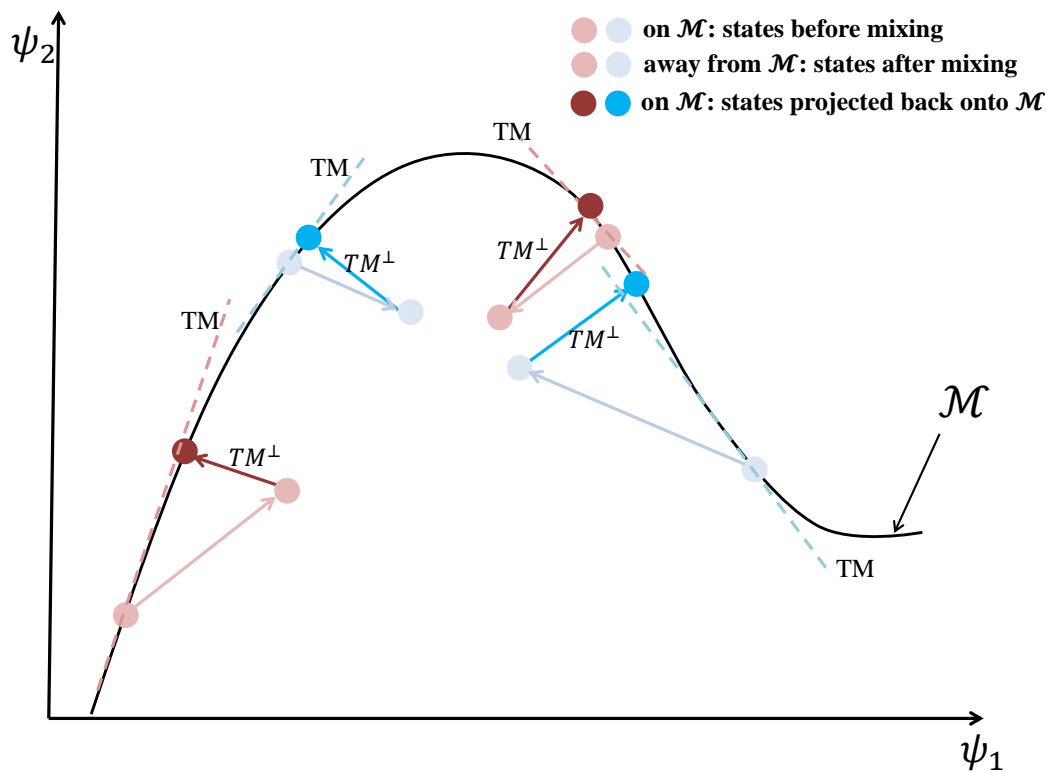


Figure 6.4: Illustration for coupling strategy between mixing process and manifold based simplified chemistry based on projection perpendicular to tangential subspace of manifold \mathcal{M} .

7 Numerical Implementation of Hybrid Finite-Volume/Transported-PDF Method Based on REDIM Reduced Chemistry

In the previous chapter the hybrid Finite-Volume/Transported-PDF method based on REDIM reduced chemistry was discussed. The coupling between FVM and PDF particle method for transported-PDF equation is discussed in Sec.6.1 and the coupling between mixing processes in PDF particle method and manifold based simplified chemistry in Sec.6.2. In this chapter, numerical implementation for the whole hybrid algorithm is discussed.

7.1 Finite Volume Method (FVM) for RANS equations

The FVM is a numerical technique that transforms the PDE system representing conservation equations over differential volumes into discrete algebraic equations over finite volume or cells [1, 26, 62]. In general, the numerical implementation of FVM can be divided into several steps, which is illustrated through Fig.7.1.

In the beginning, the set of governing equations must be defined and neither relevant nor of interest are simplified. For example, set of 3D governing equations can be simplified to 2D, or ideal gas law can be used instead of Van der Waals equation [15]. Then the computational domain is defined and discretized into computational mesh on which the governing equations are eventually solved [1, 26, 62]. In the next step, the governing equations are discretized into sets of algebraic equation for each cell in the computational domain, which are numerically solved.

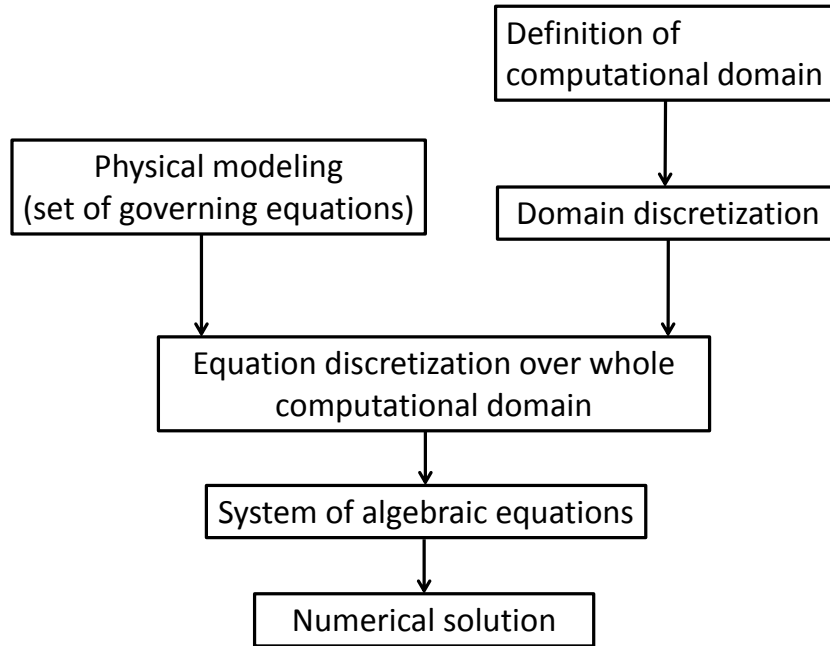


Figure 7.1: Flow chart of FVM implementation.

In this work, the inhouse-code SPARC [59] developed at KIT (Department of Fluid Machinery) is applied for the FVM part, consistent with the works of S. Lipp [49] and G.Steinhilber [89]. It is a finite-volume based solver for compressible Navier-Stokes equations on block-structured computational domain. The time integration is based on explicit Runge-Kutta method with fourth-order accuracy [24, 26], and the spatial integration for both convective and diffusive terms has second order accuracy [26, 62]. To ensure numerical stability due to convective term, the Symmetric Limited Positive (SLIP) scheme [41] is used.

In the coupling with PDF particle method, averaged density $\bar{\rho}_{FV}$ and favre-averaged velocity \tilde{u}_{FV} are obtained from FVM part and fed into PDF particle code for further calculation.

7.2 Numerical integration of the system of stochastic particle equations

As discussed in Section 4.3, the transported-PDF equation can be efficiently solved using Monte-Carlo particle method, considering a system of notional particles that obey the underlying governing conservation equations [27, 38, 73].

Evolution of stochastic particle system, although introduced in previous chapters, is reproduced here for reference:

- Particle position:

$$\frac{d\mathbf{X}^*}{dt} = \tilde{\mathbf{u}}(\mathbf{X}^*) + \mathbf{u}''^*, \quad (7.1)$$

- Partical velocity fluctuation:

$$du_i''^*(t) = -\frac{1}{\bar{\rho}} \frac{\partial(\bar{\rho} \widetilde{u_i'' u_j''})}{\partial x_j} dt - u_j''^* \frac{\partial \tilde{u}_i}{\partial x_j} dt - \left(\frac{1}{2} + \frac{3}{4} C_0 \right) \Omega u_i''^*(t) dt + \sqrt{C_0 k \Omega} dW_i, \quad (7.2)$$

- Particle turbulent frequency:

$$d\omega^*(t) = -C_3(\omega^* - \tilde{\omega})\Omega dt - S_\omega \Omega \omega^* dt + \sqrt{2C_3 C_4 \tilde{\omega} \Omega \omega^*} dW, \quad (7.3)$$

- Particle mixing and reaction:

$$\frac{d\Psi^*(t)}{dt} = \mathbf{M}^* + \mathbf{S}(\Psi^*). \quad (7.4)$$

The fractional-step method, consistent with the one in [43], is used to integrate these differential equations. The idea of this fractional-step method is to split the processes into several sub-processes, and advance numerical integration for each sub-processes independently. In the following and in Fig.7.2, all quantities at each time step are advanced from t_n to t_{n+1} ($\Delta t = t_{n+1} - t_n$) described in followings.

7.2.1 Integration of particle position

Particle positions evolve according to Eq.7.1. They are integrated in the first step over a time intervall $\frac{\Delta t}{2}$ from t_n to $t_{n+\frac{1}{2}}$ through:

$$\mathbf{X}^*(t_{n+\frac{1}{2}}) = \mathbf{X}^*(t_n) + \left(\tilde{\mathbf{u}}_{FV}^*(t_n) + \mathbf{u}''^*(t_n) \right) \cdot \frac{\Delta t}{2}, \quad (7.5)$$

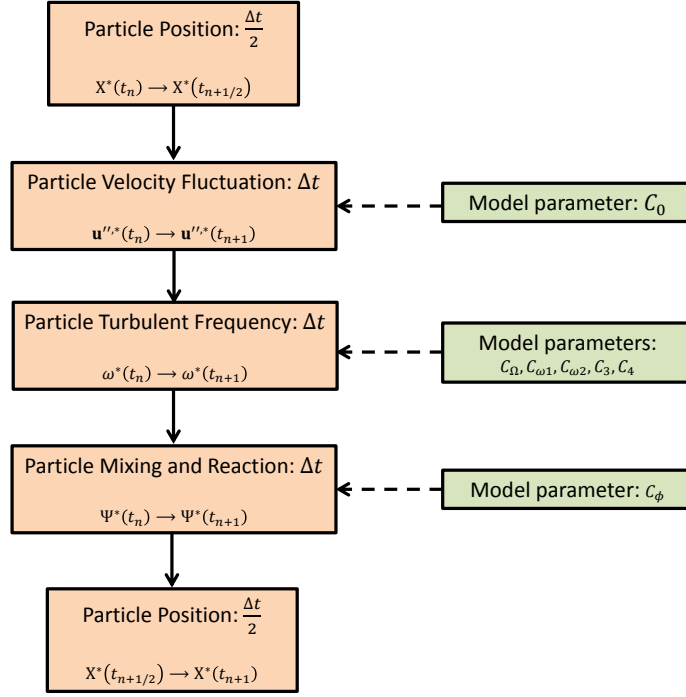


Figure 7.2: A schematic of the numerical algorithm in one time step.

so that the particle position at time $t_{n+\frac{1}{2}}$ is obtained. After integration of all other sub-processes, the particle position at time level t_{n+1} is calculated as:

$$\mathbf{X}^*(t_{n+1}) = \mathbf{X}^*(t_n) + \Delta t \cdot \left(\tilde{\mathbf{u}}_{\text{FV}}^*(t_{n+\frac{1}{2}}) + \frac{1}{2}(\mathbf{u}''^*(t_{n+1}) + \mathbf{u}''^*(t_n)) \right). \quad (7.6)$$

7.2.2 Integration of particle velocity fluctuation

Defining

$$\begin{aligned} a_i &= -\frac{1}{\bar{\rho}_{\text{FV}}} \frac{\partial(\bar{\rho} \widetilde{u''_i u''_j})}{\partial x_j}, \\ b_{ij} &= -\frac{\partial \tilde{u}_i}{\partial x_j} - \left(\frac{1}{2} + \frac{3}{4} C_0 \right) \Omega \delta_{ij}, \\ c &= C_0 k \Omega, \end{aligned}$$

Eq.7.2 becomes

$$du''_i^*(t) = a_i \cdot dt + b_{ij} \cdot u''_j^*(t)dt + \sqrt{c} \cdot dW_i. \quad (7.7)$$

7.2 NUMERICAL INTEGRATION OF THE SYSTEM OF STOCHASTIC PARTICLE EQUATIONS

The numerical integration is solved using a second-order scheme as described in [43]:

$$\begin{aligned}\Delta u_i''^{*,*} &= \left(a_i + b_{ij} \cdot u_j''^{*,*}(t_n) \right) \cdot \Delta t + \sqrt{c \cdot \Delta t} \cdot \xi_i^u, \\ u_i''^{*,*}(t_{n+1}) &= u_i''^{*,*}(t_n) + \Delta u_i''^{*,*} + \frac{1}{2} b_{ij} \cdot \Delta u_j''^{*,*} \cdot \Delta t,\end{aligned}\quad (7.8)$$

where ξ_i^u is a random variable with Gauss distribution with mean value $\overline{\xi_i^u} = 0$ and variance $\overline{\xi_i^u \xi_j^u} = 1$. The coefficients a_i , b_{ij} and c are all evaluated at the point $\mathbf{X}^*(t_{n+\frac{1}{2}})$.

7.2.3 Integration of particle turbulent frequency

Defining

$$\begin{aligned}A &= C_3 \cdot \tilde{\omega} \cdot \Omega, \\ B &= (C_3 + S_\omega) \cdot \Omega, \\ C &= 2 \cdot C_3 \cdot C_4 \cdot \tilde{\omega} \cdot \Omega,\end{aligned}$$

Eq.7.3 becomes

$$d\omega^*(t) = A \cdot dt - B \cdot \omega^* \cdot dt + \sqrt{C \cdot \omega^*} dW, \quad (7.9)$$

here the coefficients A , B and C are all evaluated at the point $\mathbf{X}^*(t_{n+\frac{1}{2}})$. The new particle turbulent frequency is [43]:

$$\omega^*(t_{n+1}) = \max(0, \mu_\omega + \sigma_\omega \cdot \xi^\omega), \quad (7.10)$$

where μ_ω is the mean value of $\omega^*(t_{n+1})$ as:

$$\mu_\omega = \omega^*(t_n) \cdot \exp(-B \cdot \Delta t) + \frac{A}{B} \cdot (1 - \exp(-B \cdot \Delta t)), \quad (7.11)$$

and σ_ω is the variance of $\omega^*(t_{n+1})$ as:

$$\sigma_\omega^2 = \frac{c \cdot \Delta t}{2 \cdot (1 + B \cdot \Delta t)} \cdot (\mu_\omega + \omega^*(t_n)). \quad (7.12)$$

Here ξ^ω is again a random variable with gauss distributaion, independent of the one ξ_i^u in the velocity fluctuation calculation.

7.2.4 Integration of particle mixing and reaction

For the particle mixing and reaction, the corresponding equation 7.4 is integrated at each time step from t_n to t_{n+1} :

$$\varphi^*(t_{n+1}) = \varphi^*(t_n) + \left[\hat{\mathbf{S}}(\varphi^*(t_n)) + \hat{\mathbf{M}}^*(\varphi^*(t_n)) \right] \cdot dt. \quad (7.13)$$

Note that in many works [30, 43, 100, 105] the mixing and reaction processes are also calculated separately, namely the thermo-kinetic states evolve at the first step due to mixing process, and at the second step due to reaction process. The numerical difference between both algorithms is minor. In this work, the mixing and reaction processes are calculated together for the evolution of progress variables because, the necessary source term can be extracted from the chemistry table, and thus is not necessary to split into two different steps.

As discussed in Sec.6.2, particle states move away from slow manifold due to mixing and reaction processes and must be projected back onto manifold. Thus the evolution of progress variables of each particle consists of the following several sub-steps:

- Start from the progress variable values φ_t^j stored for particles at considered time t and get the corresponding full thermo-kinetic state $\Psi(\varphi_t^j)$;
- Calculate the temporal evolution (mixing model and reaction) in the full thermo-kinetic state for each involved particle $\Phi\left(\Psi\left(\varphi_t^j\right)\right)$;
- Project the term of each involved particle in tangential subspace of slow manifold: $\Delta\varphi^j = \Pi \cdot \Phi\left(\Psi\left(\varphi_t^j\right)\right)$;
- Calculate the evolution of each involved particle with projected vector change related to progress variables: $\varphi_{t+\Delta t}^j = \varphi^j + \Delta\varphi^j$.

7.3 Some numerical issues in the PDF particle method

7.3.1 Control of particle number

During the initialization of PDF particle code (c.f. Fig.6.1), initial distribution of notional particle positions are consistent with the constructed finite-volume mesh. However, if non-uniform grids are employed, many particles could

be gathered in big cells due to particle motion in physical space (Eq.7.1). To maintain an acceptable spatial distribution of particles as they move in physical spatial space, a (nearly) constant number of particles per cell is desired, which is known to reduce the computational cost of numerical integration in PDF particle method [37, 38].

The most common method to achieve a uniform distribution for particle number is based on particle cloning and clustering in order to increase or decrease particle number N_p per cell. Say $N_{p,\min}$ and $N_{p,\max}$ are the (user-defined) allowed minimum and maximum of particle number cell, particles are cloned in cells having $N_p < N_{p,\min}$, while particles are clustered in cells having $N_p > N_{p,\max}$ [38, 114]. In the following, cloning and cluster strategies in particle number control used in this work are discussed.

Cloning strategy

In the cloning process, the heaviest-mass particle with mass m^* in each cell is selected. Its mass is then splitted into two particles each having mass $\frac{m^*}{2}$ and each having the same properties (e.g. velocity, turbulent frequency, thermo-kinetic state etc.) as the selected particle. In this way, the cloning process does not change the local PDF of particles properties [38]. This procedure is repeated until $N_p = N_{p,\min}$.

Clustering strategy

Unlike cloning procedure which is almost unproblematic, clustering procedure (decreasing particle number) is more challenging, because distribution of particle properties can be changed and it could lead to artificial mixing [37, 114].

In this work, the clustering strategy is followed by the one introduced in [77]. The lightest two particles with mass m_1^* and m_2^* are considered. One of both is deleted in a statistical way:

- particle 1 is removed with probability $\frac{m_2^*}{m_1^* + m_2^*}$;
- particle 2 is removed with probability $\frac{m_1^*}{m_1^* + m_2^*}$.

This procedure ensures that any statistical moment of particle property is conserved in a statistical manner [77].

7.3.2 Time-averaging technique

To reduce the statistical and bias errors of a quantity \tilde{q} and to enhance the numerical stability, it is suggested in [43] to use the following time-averaging technique for statistically stationary problems:

$$\tilde{q}(t_{n+1}) = \mu_{ta} \cdot \tilde{q}(t_n) + (1 - \mu_{ta}) \cdot \tilde{q}_{inst}(t_{n+1}), \quad (7.14)$$

where

$$\mu_{ta} = \frac{N_{TA} - 1}{N_{TA}} \quad (7.15)$$

with the time-averaging factor $N_{TA} > 1$.

Equation 7.14 shows that the new averaged value of any quantity at time level t_{n+1} determined from the value of time level t_n , $\tilde{q}(t_n)$, weighted with weighting factor μ_{ta} , and the instantaneous value at time level t_{n+1} , $\tilde{q}_{inst}(t_{n+1})$, weighted with factor $1 - \mu_{ta}$. As shown in [43, 89], the larger the time-averaging factor N_{TA} is, the smaller the statistical and bias errors are. However, one needs more integration steps to obtain stationary solution. A numerical investigation for time-averaging technique is given in details in [43].

7.3.3 Some issues in REDIM storage and application coupled with PDF

REDIM storage and interpolation strategy

In the calculation of evolution of thermo-kinetic state for each particle based on REDIM reduced chemistry, all necessary informations will be pre-calculated and stored in REDIM table. Furthermore, REDIM is parametrized using progress variables φ for convenient usage in turbulent calculation. The generated REDIM reduced chemistry is stored using orthogonal and equidistant mesh (shown in Fig.7.3), because it is ideally structured for an efficient look-up, and a point-by-point search is not required [10].

In each grid point $\varphi^{i,j} = (\varphi_1^{i,j}, \varphi_2^{i,j})^T$, the following useful quantities are stored:

- temperature $T(\varphi)$,
- specific gas constant $R_g(\varphi)$,
- thermo-kinetic state $\Psi(\varphi)$,
- projection matrix $\Pi = \mathbf{C}_\varphi \cdot \Psi_\theta \cdot \Psi_\theta^+$ and

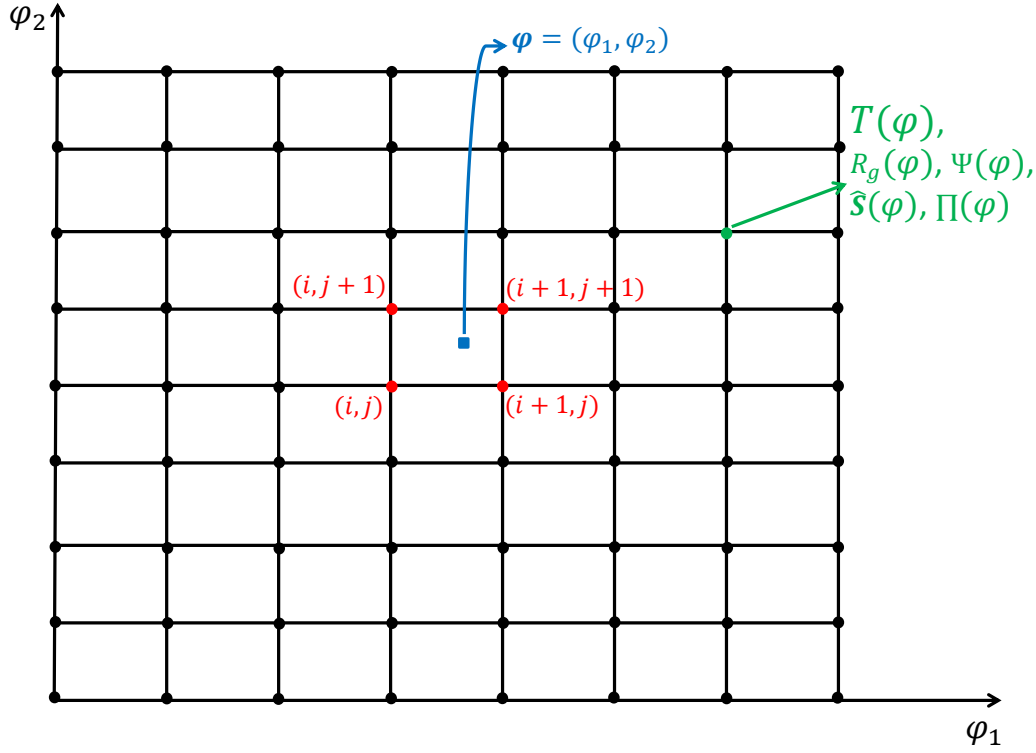


Figure 7.3: Example of REDIM storage.

- projected thermo-kinetic source term $\hat{S}(\varphi) = \Pi \cdot \mathbf{S}(\Psi(\varphi))$.

The table look-up is based on bilinear interpolation which has a low computational cost, because all steps are calculated in form of algebraic equations. Say the value of a quantity $q(\varphi) = q(\varphi_1, \varphi_2)$ should be calculated. Then the bilinear interpolation is [75]:

Step 1: linear interpolation in φ_1 -direction:

$$q(\varphi_1, \varphi_2^{i,j}) = \frac{\varphi_1^{i+1,j} - \varphi_1}{\varphi_1^{i+1,j} - \varphi_1^{i,j}} \cdot q(\varphi_1^{i,j}, \varphi_2^{i,j}) + \frac{\varphi_1 - \varphi_1^{i,j}}{\varphi_1^{i+1,j} - \varphi_1^{i,j}} \cdot q(\varphi_1^{i+1,j}, \varphi_2^{i+1,j})$$

$$q(\varphi_1, \varphi_2^{i,j+1}) = \frac{\varphi_1^{i+1,j} - \varphi_1}{\varphi_1^{i+1,j} - \varphi_1^{i,j}} \cdot q(\varphi_1^{i,j+1}, \varphi_2^{i,j+1}) + \frac{\varphi_1 - \varphi_1^{i,j}}{\varphi_1^{i+1,j} - \varphi_1^{i,j}} \cdot q(\varphi_1^{i+1,j+1}, \varphi_2^{i+1,j+1})$$

Step 2: linear interpolation in φ_2 -direction:

$$q(\varphi) = q(\varphi_1, \varphi_2) = \frac{\varphi_2^{i+1,j+1} - \varphi_2}{\varphi_2^{i+1,j+1} - \varphi_2^{i,j+1}} \cdot q(\varphi_1, \varphi_2^{i,j}) + \frac{\varphi_2 - \varphi_2^{i,j+1}}{\varphi_2^{i+1,j+1} - \varphi_2^{i,j+1}} \cdot q(\varphi_1, \varphi_2^{i,j+1}) \quad (7.16)$$

8 Study of turbulent non-premixed CH₄-air flames

In the previous chapters, all necessary tools for the numerical simulation of turbulent reacting flows have been discussed. Chapter 3.3 deals with the RANS method and chapter 4 deals with the PDF method for the closure of Favre-averaged Reynolds stresses and thermo-kinetic source term in RANS. To reduce the computational cost stemmed from detailed chemistry, chapter 5 discusses the model reduction for manifold based simplified chemistry. Then in chapter 6 the coupling strategies between FVM and PDF methods, and between mixing process in PDF method and manifold based simplified chemistry are discussed. In chapter 7 numerical implementation for the whole methodology is outlined.

In this chapter the proposed methodology is validated for the well-known turbulent non-premixed piloted CH₄-air flames, namely the Sandia Flame D, E and F [4].

8.1 Experimental configuration

The methane/air piloted turbulent jet Sandia flame is used as experimental test-case to simulate the turbulent flame. The geometrical configuration is schematically sketched in Fig.8.1. In the following, important information for this flame series is listed, more details can be found in [4] and experimental measurements can be found in [6].

This flame series consists of a main fuel jet with $D = 7.2$ mm diameter, with a mixture composition of 25% methane and 75% dry air by volume. The initial temperature is 294K. The coaxial pilot has an inner diameter of 7.7mm and an outer diameter of 18.2mm, with a mixture of C₂H₂, air, CO₂ and N₂, and is operated at lean condition ($\Phi = 0.77$), with the same nominal enthalpy and equilibrium composition as methane/air at this equivalence ratio. The energy release of the pilot is approximately 6% of the main jet for each flame. The piloted burner is fixed with the jet exit approximately 15cm above the wind tunnel exit, which has a dimension of 30 cm × 30 cm.

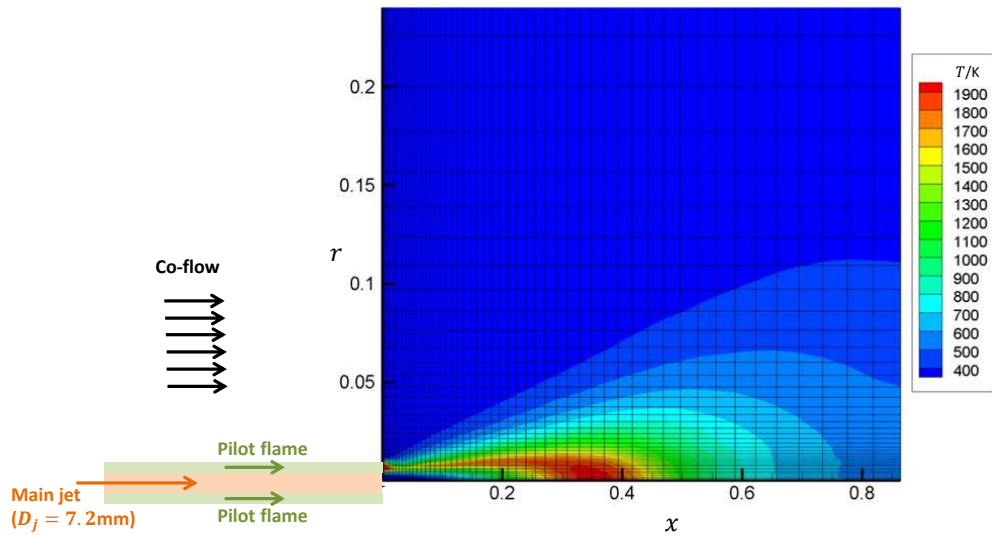


Figure 8.1: Schematic Sandia flame configuration.

The jet velocities this flame series increase from D to F as:

- Sandia Flame D: the Reynolds number of the jet is 22400, which represents a jet velocity of 49.6m/s;
- Sandia Flame E: the Reynolds number of the jet is 33600, which represents a jet velocity of 74.4m/s;
- Sandia Flame F: the Reynolds number of the jet is 44800, which represents a jet velocity of 99.2m/s;

Experimental measurements are performed with spontaneous Raman and Rayleigh scattering for major species and temperature. The LIF technique is used for the concentrations of OH and NO. The uncertainties of the measurements are estimated to be within $\pm 2\%$ for mass fractions of N₂, O₂, CH₄, CO₂, H₂O, H₂ and temperature, $\pm 5\%$ for OH and CO, and $\pm 10\%$ for NO [4].

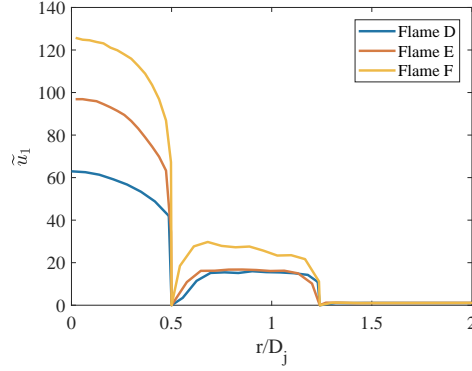


Figure 8.2: Mean velocities in axial direction \tilde{u}_1 for Sandia Flame D, E and F at jet exit plane ($x = 0$).

8.2 Numerical set-up

In order to perform numerical simulation, information about boundary conditions for e.g. mean velocities, Reynolds stresses, temperatures, species concentrations and turbulent frequency are necessary. In this section, we shortly outline the procedure how numerical issues such as boundary conditions and model parameters are set up for Sandia Flame D, E and F. The origin of spatial coordinate is fixed at the center of jet exit plane (see Fig.8.1). In the following, q_1 stands for a quantity q in axial direction, q_2 in radial direction and q_3 in circumferential direction.

8.2.1 Boundary conditions for the flow field

In [6] experimental measurement for most flow quantities are provided. Therefore, they can be directly used as boundary conditions. The mean velocity in axial direction \tilde{u}_1 is taken from measurement [6] (shown in Fig.8.2 for all flames), while \tilde{u}_2 in radial direction is set to be 0 because they are negligible small (of order of magnitude $O(1)$ m/s), consistent with the choice in [17].

For Reynolds stresses, all values except unmeasured $\widetilde{u_3''u_3''}$ are also taken from measurement [6], which are shown in Fig.8.3. The Reynolds stress $\widetilde{u_3''u_3''}$ in the circumferential direction, which was not measured, is taken to be equal to the radial normal stresses, consistent with the choice in [17]:

$$\widetilde{u_3''u_3''} = \widetilde{u_2''u_2''}. \quad (8.1)$$

Furthermore, for the model of turbulent frequency Eq.4.21, one also needs the turbulent frequency at the inlet and its variance. Consistent with the

8 STUDY OF TURBULENT NON-PREMIXED CH₄-AIR FLAMES

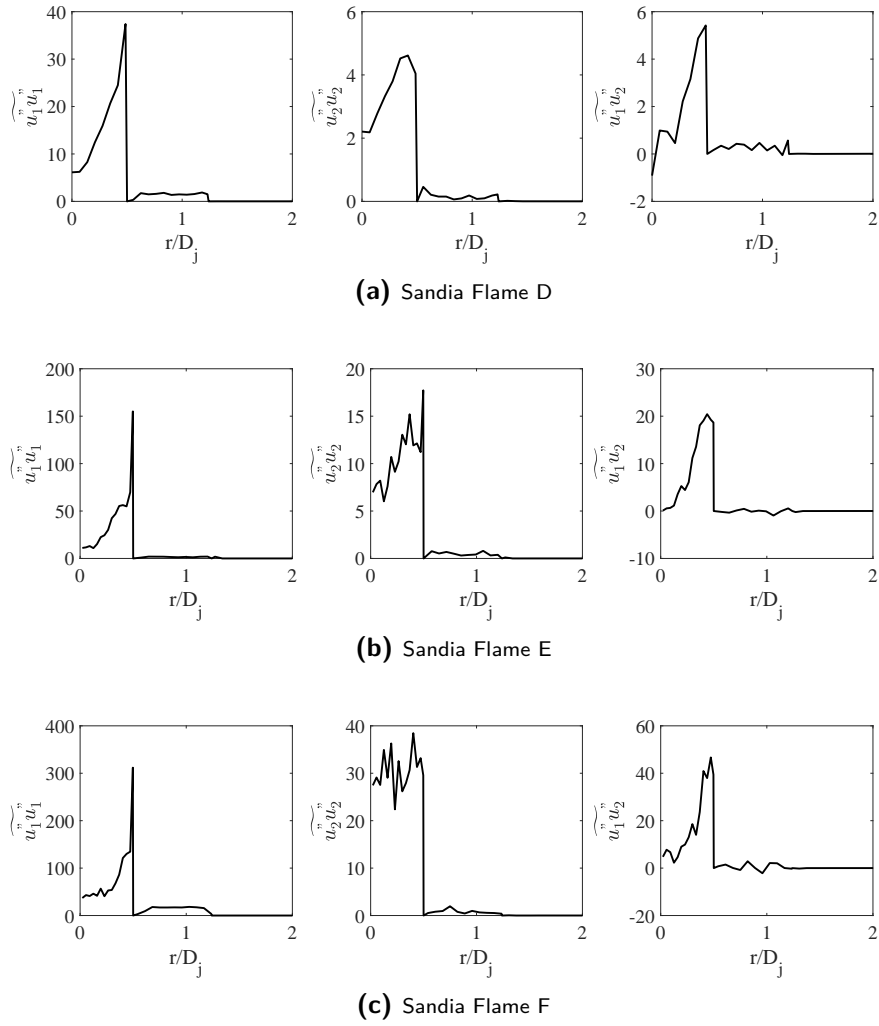


Figure 8.3: Reynolds stresses $\overline{u_1''u_1''}$, $\overline{u_2''u_2''}$ and $\overline{u_1''u_2''}$ along radial direction at jet exit plane ($x = 0$) for Sandia Flame D (a), E (b) and F (c).

set-up in [17], the ratio of production to dissipation of turbulent kinetic energy k is specified as unity as follows:

$$\frac{\wp}{\epsilon} = \frac{\wp}{k \cdot \tilde{\omega}} = 1 \quad (8.2)$$

where ϵ is the dissipation rate, k the turbulent kinetic energy and \wp the rate of production of turbulent kinetic energy calculated as [72]:

$$\wp = \overline{u_1''u_2''} \cdot \frac{\partial \tilde{u}_1}{\partial r}. \quad (8.3)$$

In this equation, quantities of $\widetilde{u_1''u_2''}$ and $\widetilde{u_1}$ can be taken from experimental measurement (c.f. Fig.8.2 and Fig.8.3). Equation 8.2 and 8.3 together determine the inlet profile of mean turbulent frequency at jet exit plane $x = 0$.

8.2.2 Boundary condition for thermo-kinetic state

As already outlined in previous section, main jet consists of 25% CH₄ and 75% dry air by volume under temperature $T = 294\text{K}$ and pressure 1bar, the corresponding thermo-kinetic state is:

$$\Psi_{\text{main-jet}} = \begin{pmatrix} H \\ p \\ \phi_{\text{N}_2} \\ \phi_{\text{O}_2} \\ \phi_{\text{CO}_2} \\ \phi_{\text{CH}_4} \\ \phi_{\text{OH}} \\ \vdots \end{pmatrix} = \begin{pmatrix} -725.7 \text{ kJ/kg} \\ 1 \cdot 10^5 \text{ Pa} \\ 23.21 \text{ mol/kg} \\ 6.088 \text{ mol/kg} \\ 0.0 \text{ mol/kg} \\ 9.66 \text{ mol/kg} \\ 0.0 \text{ mol/kg} \\ \vdots \end{pmatrix} \quad (8.4)$$

The co-flow consists of pure dry air under temperature $T = 292\text{K}$ and pressure 1bar, the corresponding thermo-kinetic state is:

$$\Psi_{\text{co-flow}} = \begin{pmatrix} H \\ p \\ \phi_{\text{N}_2} \\ \phi_{\text{O}_2} \\ \phi_{\text{CO}_2} \\ \phi_{\text{CH}_4} \\ \phi_{\text{OH}} \\ \vdots \end{pmatrix} = \begin{pmatrix} -7.18 \text{ kJ/kg} \\ 1 \cdot 10^5 \text{ Pa} \\ 27.30 \text{ mol/kg} \\ 7.35 \text{ mol/kg} \\ 0.0 \text{ mol/kg} \\ 0.0 \text{ mol/kg} \\ 0.0 \text{ mol/kg} \\ \vdots \end{pmatrix} \quad (8.5)$$

The pilot composition at the burner exit can be taken as the composition of an unstrained CH₄/air premixed flame with fuel/air equivalent ratio $\xi = 0.77$ at the point in the flame profile where temperature $T = 1880\text{K}$, because it has

the same enthalpy and equilibrium composition as experimental measurements [4]. Following this process, the thermo-kinetic state is:

$$\Psi_{\text{pilot}} = \begin{pmatrix} H \\ p \\ \phi_{\text{N}_2} \\ \phi_{\text{O}_2} \\ \phi_{\text{CO}_2} \\ \phi_{\text{CH}_4} \\ \phi_{\text{OH}} \\ \vdots \end{pmatrix} = \begin{pmatrix} -206.7 \text{ J/kg} \\ 1 \cdot 10^5 \text{ Pa} \\ 26.22 \text{ mol/kg} \\ 1.65 \text{ mol/kg} \\ 2.50 \text{ mol/kg} \\ 0.0 \text{ mol/kg} \\ 0.17 \text{ mol/kg} \\ \vdots \end{pmatrix} \quad (8.6)$$

8.2.3 Computational domain and numerical parameters

The simulation is performed for a $120D \times 40D$ domain discretized by 51×42 cells (total of 2142 cells).

The initial number of particles per cell is $N_p = 50$. During the control of particle number, the maximum allowed particle number per cell is $N_{p,max} = 1.2 \cdot N_p = 60$ and the minimum is $N_{p,min} = 0.8 \cdot N_p = 40$, which is consistent with the choice in [61].

In the time-averaging technique, time-averaging factor $N_{TA} = 2000$ is used in Eq.7.15, which is consistent with the choice in [17].

The following table lists the parameters and their respective values for each model used in transported-PDF method.

Turbulent Frequency Model	
C_Ω	0.6893
$C_{\omega 1}$	0.71
$C_{\omega 2}$	0.9
C_3	1.0
C_4	1.25
Simplified Langevin Model	
C_0	2.1
Mixing Model (EMST)	
C_ϕ	1.5

Table 8.1: Parameters used in the simulation of the turbulent flame.

8.2.4 Progress variables and parametrization coordinates

The applied 2D REDIM reduced chemistry used in this work is parametrized by reduced coordinates $\theta = (\theta_1, \theta_2)^T = (\phi_{\text{N}_2}, \phi_{\text{CO}_2})^T$. This choice is arbitrary, with the only condition that any quantity q in REDIM table is a surjective function $f: q = f(\theta_1, \theta_2)$. In other words, at each point $\theta = (\theta_1, \theta_2)^T$, there exists one and only one corresponding function value q .

The progress variables stored in notional particles are $\varphi = (\varphi_1, \varphi_2)^T = (\phi_{\text{N}_2}, \phi_{\text{CO}_2})^T$. Note that the choice of progress variables does not affect the simulation results, but the projection process yes (see Sec. 6.2). Therefore, other choice of progress variables can be chosen through a parametrization matrix as:

$$\begin{pmatrix} \varphi_1 \\ \varphi_2 \end{pmatrix} = \mathbf{C}_\varphi \cdot \Psi \quad (8.7)$$

where here \mathbf{C}_φ is a parametrization matrix with dimension $2 \times n$, and Ψ the thermo-kinetic state vector with dimension $n \times 1$ ($n = n_{sp} + 2$).

8.2.5 Slow subspaces for CH₄ combustion system

In the definition of the projection process discussed in Sec.6.2, the determination of the projection perpendicular to slow subspaces still needs information about the slow subspaces or coordinates of slow variables (η or \mathbf{C}_η) in Eq. 6.5:

$$\Psi_\theta^+ = (\mathbf{C}_\eta \cdot \Psi_\theta)^{-1} \cdot \mathbf{C}_\eta$$

In the literature, the first slow variable is mostly selected as specific mole number of N₂ (ϕ_{N_2}), which describes the mixing process due to its monotonical dependence on mixture fractions. The second slow variable is defined differently, and two variants are given as follows as examples:

- Variant 1: according to one suggested by Pierce and Moin [67]:

$$\eta = w_{\text{CO}_2} + w_{\text{H}_2\text{O}}; \quad (8.8)$$

- Variant 2: according to one suggested by Van Oijen and de Goey [98]:

$$\eta = \phi_{\text{CO}_2} + \phi_{\text{H}_2\text{O}} + \phi_{\text{H}_2}. \quad (8.9)$$

According to different definition of η , one obtain different parametrization matrix \mathbf{C}_η for Eq.6.5 for the determination of projection matrix in Eq. 6.5. However, the choice of the second slow variable in these variants only considers

one-to-one correspondence between η and Ψ , and no more mathematical and physical meanings are supported.

To find out the optimal reduced coordinate for CH₄-O₂-N₂ reaction system, the GQL approach is conducted for an isobaric homogeneous reaction process for CH₄-O₂-N₂ combustion system. The detailed chemistry GRI 3.0 [81] consists of 53 species and 325 elementary reactions including NOx chemistry. The generated GQL reduced chemistry should be valid for a wide range initial temperatures ($1000\text{K} \leq T_0 \leq 2000\text{K}$) and mixture compositions ($0.4 \leq \Phi \leq 3.0$), same as the conditions in Sec.5.2.4. The initial pressure considered here remains constant as $p_0 = 1$ bar, since the Sandia Flame is operated under ambient conditions [4].

Following the procedure described in Sec. 5.2.2, an $m_s = 18$ dimensional GQL reduced chemistry is generated¹. Below the first four eigenvalues N_s and corresponding characteristic time-scales τ_s of the generated 18-dimensional GQL for GRI 3.0 are listed:

$$N_s = \begin{pmatrix} \lambda_{s1} \\ \lambda_{s2} \\ \lambda_{s3} \\ \lambda_{s4} \\ \vdots \end{pmatrix} = \begin{pmatrix} -0.041 \\ -164.6 \\ -1.21 \cdot 10^3 \\ -1.28 \cdot 10^3 \\ \vdots \end{pmatrix} \quad (8.10)$$

$$\tau_s = \begin{pmatrix} \tau_{s1} \\ \tau_{s2} \\ \tau_{s3} \\ \tau_{s4} \\ \vdots \end{pmatrix} = \begin{pmatrix} 1/|\lambda_{s1}| \\ 1/|\lambda_{s2}| \\ 1/|\lambda_{s3}| \\ 1/|\lambda_{s4}| \\ \vdots \end{pmatrix} = \begin{pmatrix} 24.52 \\ 0.0061 \\ 8.28 \cdot 10^{-4} \\ 7.82 \cdot 10^{-4} \\ \vdots \end{pmatrix} s. \quad (8.11)$$

We notice that both slow subspaces are indeed controlled by slow modes. The first mode corresponds to a characteristic time-scale in order of magnitude $O(10\text{ s})$ and the second $O(10^{-3}\text{ s})$, which are larger than the turbulent time-scales for at least Sandia Flame D and E shown in [45]. Therefore except the first two slowest time-scales, the rest can be decoupled. Directions in which states are projected back onto slow manifolds can be approximately by using slow subspaces controlled by the first two slowest eigenvalues $\lambda_{s1} = -0.04077$ and $\lambda_{s2} = -164.634$.

¹In Sec.5.2.4 a 14-dimensional GQL based on Sandiego-2014 mechanism is generated for CH₄-air combustion system. Here a 18-dimensional GQL reduced chemistry is generated for GRI 3.0, because it includes NOx chemistry, and 4 additional dimensions are needed to describe NOx.

If the thermo-kinetic state vector is defined as:

$$\Psi = (h, p, \phi_{\text{N}_2}, \phi_{\text{H}_2\text{O}}, \phi_{\text{CO}_2}, \dots, \phi_{\text{NO}}, \phi_{\text{NO}_2}, \dots)^{\text{T}}, \quad (8.12)$$

then the $(m_s \times n = 2 \times 55)$ -dimensional slow subspaces is $\tilde{Z}_s = (\tilde{Z}_{s1}, \tilde{Z}_{s2})^{\text{T}}$:

$$\begin{array}{cccccccc} h & p & \phi_{\text{N}_2} & \phi_{\text{H}_2\text{O}} & \phi_{\text{CO}_2} & \cdots & \phi_{\text{NO}} & \phi_{\text{NO}_2} & \cdots \\ \tilde{Z}_s = \begin{pmatrix} 0 & 0 & 0.032 & 0.005 & -2.85 \cdot 10^{-4} & \cdots & 1.0 & 0.99 & \cdots \\ 0 & 0 & 0.013 & 0.48 & 1.0 & \cdots & -0.074 & -0.094 & \cdots \end{pmatrix} \end{array} \quad (8.13)$$

Note that here the matrix is scaled such that the largest absolute entry in each row is 1. Then the projection matrix Π_{C} using the above \tilde{Z}_s reads:

$$\Pi_{\text{C}} = \mathbf{C}_{\varphi} \Psi_{\theta} \cdot (\Psi_{\theta})^{+} = \mathbf{C}_{\varphi} \Psi_{\theta} \cdot (\tilde{Z}_s \cdot \Psi_{\theta})^{-1} \cdot \tilde{Z}_s. \quad (8.14)$$

In this way, two slow variables defined by this slow subspace $\mathbf{U} = (\mathcal{U}_1, \mathcal{U}_2)^{\text{T}} = \tilde{Z}_s \cdot \Psi$ are defined. According to the discussion in Sec.6.2, it means that states are projected back onto slow manifold in the direction \mathcal{U}_1 and \mathcal{U}_2 remain unchanged. It can be observed that the first (and also the slowest) slow variable consists mainly of NOx species (e.g. NO and NO₂ listed above). This coincides with the fact that NOx chemistry is very slow and its involving chemical time-scales are long [35, 104].

However, using a full detailed \tilde{Z}_s would cause a non-surjective mapping between thermo-kinetic states q and $\eta = \mathbf{C}_{\eta} \cdot \Psi$, which complicates numerical calculation of projection process. Therefore, the goal now is to simplify slow subspace \tilde{Z}_s without losing accuracy and ensures a surjective mapping. In the following, slow subspace \tilde{Z}_s is simplified with two different ways.

Simplification for \tilde{Z}_{s1} :

The first slow variable (\mathcal{U}_1) is controlled by the slowest mode (besides conserved modes) with an order of magnitude $O(10 \text{ s})$. Furthermore, we observe that the entries for NOx species are comparably larger than other species. This gives us a hint that this slowest mode is attributed to the NOx slow chemistry. Figure 8.4 (b) shows the state space in N_2 - \mathcal{U}_1 -projection for the 2D REDIM generated for Sandia Flame. We observe clearly that there is almost a linear relation between N_2 and \mathcal{U}_1 . This indicates that the first reduced coordinate can be chosen as specific mole number of N_2 for simplicity.

$$\tilde{Z}_{s1}^{\text{Simp}} = (0, 0, 1, 0, 0, 0, \dots), \quad \text{if } \Psi = (h, p, \phi_{\text{N}_2}, \phi_{\text{H}_2\text{O}}, \phi_{\text{CO}_2}, \phi_{\text{O}}, \phi_{\text{H}}, \phi_{\text{OH}}, \dots)^{\text{T}} \quad (8.15)$$

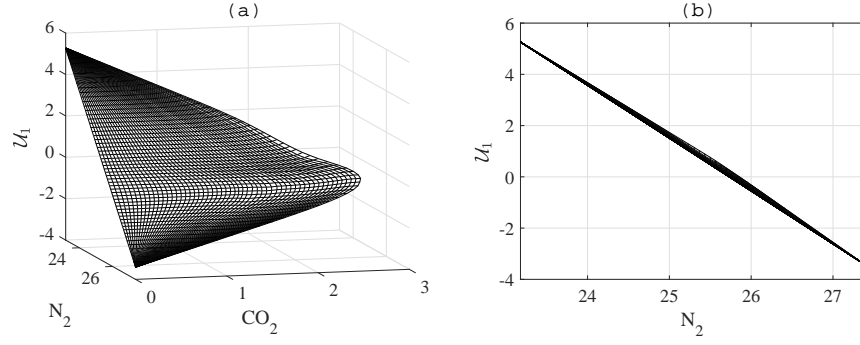


Figure 8.4: State space in N₂-CO₂- \mathcal{U}_1 -projection (a) and N₂- \mathcal{U}_1 -projection (b) for the 2D REDIM generated for Sandia Flame.

which corresponds to:

$$\mathcal{U}_1 = \phi_{N_2}. \quad (8.16)$$

This is consistent to many other studies [67, 69, 76] that mixture fraction is used as a progress variable. N₂ is linearly dependent on mixture fraction, and mixture fraction can be seen as a conserved quantity which does not change during fast back relaxation process. This means, the thermo-kinetic states are projected back onto slow manifold in direction where ϕ_{N_2} (mixture fraction) does not change.

Simplification for \tilde{Z}_{s2} :

Now let us take a look at $\tilde{Z}_{s,2}$. We observe that most of the entries are small. Furthermore, many minor species are in much smaller amount compared to major species so that the multiplication of entry values and the corresponding specific mole number (Eq.8.17) is small:

$$\left| \tilde{Z}_{s2,i} \cdot \Psi_{i,\max} \right|, \quad i = 1, 2, \dots, n \quad (8.17)$$

where $\tilde{Z}_{s2,i} = (\tilde{Z}_{s2,1}, \tilde{Z}_{s2,2}, \dots, \tilde{Z}_{s2,n})$. If we only select the first largest two values so that the others are

$$\left| \tilde{Z}_{s2,i} \cdot \Psi_{i,\max} \right| < 5.0, \quad (8.18)$$

and set such small terms to 0, we obtain the following simplified parametrization matrix:

$$\tilde{Z}_{s2}^{\text{Simp}} = (0, 0, 0, 0.5, 1, 0, 0, \dots), \quad \text{if } \Psi = (h, p, \phi_{N_2}, \phi_{H_2O}, \phi_{CO_2}, \phi_O, \phi_H, \phi_{OH}, \dots)^T \quad (8.19)$$

which corresponds to:

$$\mathcal{U}_2 = \phi_{\text{CO}_2} + 0.5 \cdot \phi_{\text{H}_2\text{O}}. \quad (8.20)$$

This means, the thermo-kinetic states are projected back onto slow manifold approximately in direction where $\phi_{\text{CO}_2} + 0.5 \cdot \phi_{\text{H}_2\text{O}}$ does not change.

Test of simplified reduced coordinate for homogeneous reacting system

According to the Eq.8.12, we obtain one simplified slow subspace:

$$\tilde{Z}_s^{\text{Simp}} = \begin{pmatrix} \tilde{Z}_{s1} \\ \tilde{Z}_{s2} \end{pmatrix} = \begin{pmatrix} 0 & 0 & 1.0 & 0 & 0 & \cdots & 0 & 0 \cdots \\ 0 & 0 & 0 & 0.5 & 1.0 & \cdots & 0 & 0 \cdots \end{pmatrix}. \quad (8.21)$$

In order to validate this simplified slow subspaces, in Fig.8.5 we compare the results of ignition delay times based on detailed chemistry (symbols), original full \tilde{Z}_s given by Eq.8.13 (red lines) and simplified $\tilde{Z}_s^{\text{Simp}}$ given by Eq.8.21 (blue lines) for homogeneous reacting system. We notice that although solutions using full \tilde{Z}_s give better prediction, relative errors of solutions using simplified $\tilde{Z}_s^{\text{Simp}}$ are all less than 6%, indicating that this simplified slow subspace given in Eq.8.15 is simple but practically without loss of accuracy.

In Fig.8.5 right two figures, we compare the ignition delay time again between using detailed chemistry and using the simplified \tilde{Z}_s^* given in Eq.8.15 for initial pressure $p_0 = 1\text{bar}$ and stoichiometric mixture of CH_4 and air over temperature range $900\text{K} \leq T_0 \leq 2000\text{K}$. Again we notice that the relative deviations between using detailed chemistry and using the simplified \tilde{Z}_s^* given in Eq.8.15 are only less than 5%, indicating that this projection matrix (or reduced slow variables) given in Eq.8.15 is simple but practically without loss of accuracy.

8.3 Simulation of Sandia Flame series based on GRI 3.0 and unity Lewis number assumption for molecular transport

In this section, the GRI 3.0 mechanism [81] is selected to generate the REDIM reduced chemistry, and the unity Lewis number assumption for molecular transport is applied. The construction of the 2D REDIM reduced chemistry is discussed in details in Sec. 5.3.5, and the validity of 2D REDIM reduced chemistry is verified there based on an investigation of the laminar counterflow

8 STUDY OF TURBULENT NON-PREMIXED CH₄-AIR FLAMES

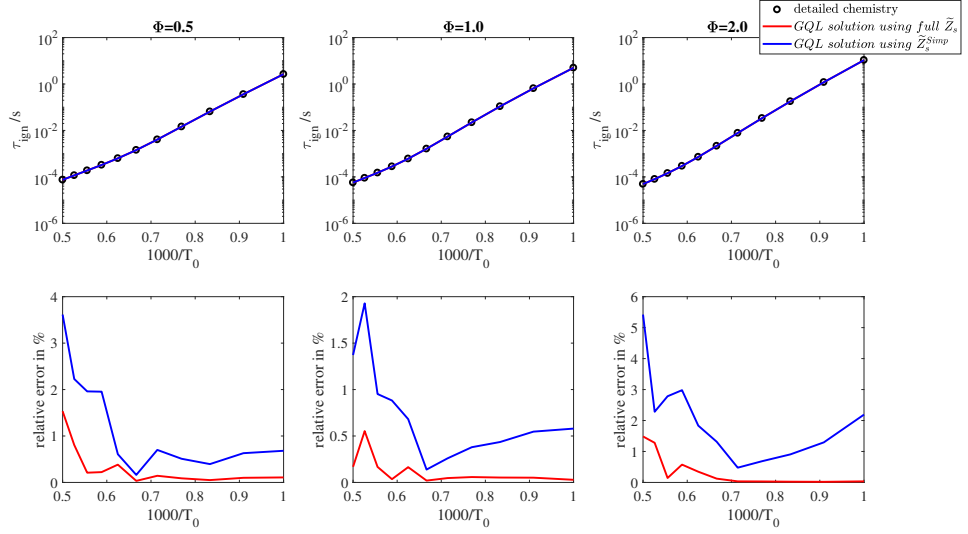


Figure 8.5: Ignition delay time τ_{ign} (upper) and the relative errors of τ_{ign} (below) for initial pressure $p_0 = 1\text{bar}$ over temperature range $1000\text{K} \leq T_0 \leq 2000\text{K}$ and different fuel/air equivalent ratios. Circles: detailed chemistry; Red lines: GQL reduced chemistry using full \tilde{Z}_s given by Eq.8.13; Blue lines: GQL reduced chemistry using simplified $\tilde{Z}_s^{\text{simp}}$ given by Eq.8.21.

diffusion flames. In the following, this 2D REDIM reduced chemistry will be applied for the simulation of Sandia Flame D, E and F.

To validate the proposed algorithm, the following results are plotted together:

- Experimental measurements from [6] are plotted with circles;
- Simulation results based on ISAT detailed chemistry [17] are shown with black lines;
- Simulation results using 2D REDIM reduced chemistry. Its coupling with mixing processes is based on a projection strategy perpendicular to slow subspaces (symbolized by dashed lines), three variants are selected:
 - the first one is the strategy according to Pierce and Moin (Eq.8.8) [67] denoted by purple dashed lines. In the following, it is called $\Pi_{\tilde{Z}_s}^\perp$ (P&M);
 - the second one is the strategy according to Van Oijen and de Goey (Eq.8.9) [98] denoted by blue dashed lines. In the following, it is called $\Pi_{\tilde{Z}_s}^\perp$ (FGM); and

- the third one is obtained by using GQL approach proposed in Sec.8.2.5 (Eq.8.21) denoted by red dashed lines. In the following, it is called $\Pi_{Z_s}^\perp$ (GQL).
- Simulation results using 2D REDIM reduced chemistry. Its coupling with mixing processes is based on a projection strategy perpendicular to tangential subspaces of slow manifold symbolized by red solid lines. In the following, it is called Π_{TM}^\perp .

Since the Sandia Flame serie operates under different Reynolds numbers of the main jet, each flame configuration has a different degree of local extinction and re-ignition. For example, the Sandia Flame D has a smaller Reynolds number, meaning that it has a lower degree of local extinction, while Sandia Flame F with the highest Reynold number in this serie has a much higher degree of local extinction. In order to validate simulation results of proposed algorithms and projection strategies, two important quantities must be introduced and examined for validation:

Conditional favre-averaged quantities $\widetilde{q|\xi}$

Since turbulent flows undergo random processes that can be described in a statistical way, scatter plots of thermo-kinetic states provide the possibility to have a first insight. Figure 8.6 shows scatter plots of temperatures for two different positions, $x/D_j = 7.5$ and $x/D_j = 30$, for Sandia Flame D, E and F from experimental measurements [6]. Additionally two stable burning solutions of laminar counterflow-diffusion flame scenarios with very low (upper red lines) and close to extinction limit (lower red lines) strain rates are also shown, in order to explicitly show the regimes of stable burning laminar flames (in the following, this regime is called as "stable flame regime"). Several observations should be adresses here:

- **Local Extinction:** All three flames have scatter points outside the stable flame regime, meaning the occurance of local extinction. As the turbulence becomes stronger, more scatter points are located outside the stable flame regime. For Sandia Flame F, a large number of scatter points can be observed outside the stable flame regime for both $x/D_j = 7.5$ and $x/D_j = 30$, which means that a high degree of local extinction takes place overall for Sandia Flame F.
- **Re-ignition** Now let us focus on Sandia Flame D and E. At position $x/D_j = 7.5$, more scatter points outside stable flame regime can be

observed for Sandia Flame E than those for Sandia Flame D. This means, higher degree of local extinction occurs for Sandia Flame E than it for Sandia Flame D. However, at position $x/D_j = 30$, most scatter points for both Sandia Flame D and E are located within stable flame regime. This phenomenon means that at $x/D_j = 30$ Sandia Flame E is re-ignited (after local extinction takes place at $x/D_j = 7.5$) and a burning flame is built.

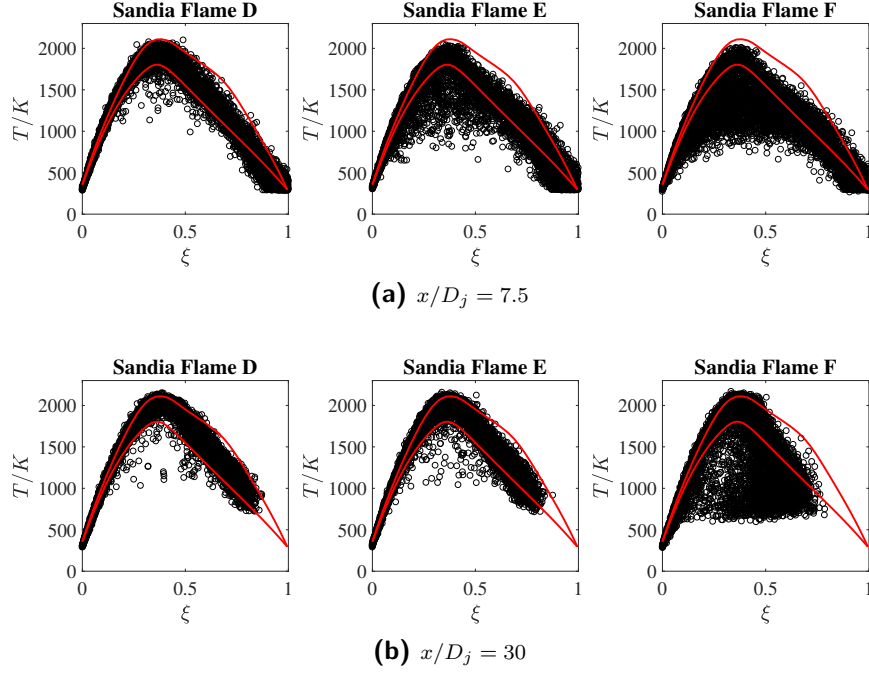


Figure 8.6: Scatter plots of temperatures at $x/D_j = 7.5$ and $x/D_j = 30$ for Sandia Flame D, E and F from experimental measurements [6].

Although scatter plots provide statistical information about how frequent one event (e.g. one certain temperature, or one certain mass fraction of species) occurs, a better quantitative comparison between experimental measurement and simulation results is achieved by comparing the so-called conditional favre-averaged (conditioned on mixture fraction) value of any quantity defined as:

$$\widetilde{q|\xi} = \frac{\overline{\rho \cdot q|\xi = \varsigma}}{\overline{\rho|\xi = \varsigma}} \quad (8.22)$$

In Fig.8.7 conditional favre-averaged temperatures at $x/D_j = 7.5$ and $x/D_j = 30$ from experimental measurements [6] for Sandia Flame D, E and F

are shown as examples. At $x/D_j = 7.5$ where local extinction can be observed, the higher turbulence flames have, the lower the conditional favre-averaged temperatures are. At $x/D_j = 30$ where re-ignition takes place, Sandia Flame D and E have similar conditional favre-averaged temperatures.

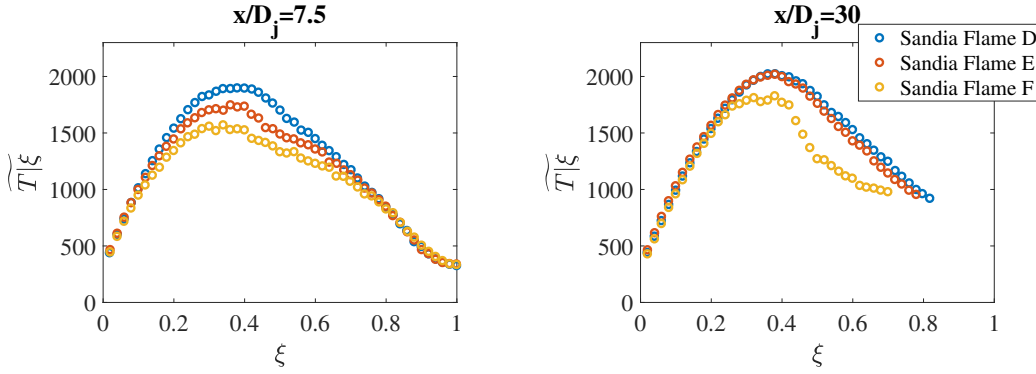


Figure 8.7: Conditional favre-averaged temperatures at $x/D_j = 7.5$ and $y/D_j = 30$ for Sandia Flame D, E and F from experimental measurements [6].

Burning Index of Temperature $BI(T)$:

Besides conditional favre-averaged values, in order to quantify the local extinction and re-ignition the so-called Burning Index (BI) has been introduced in [107]. For temperature it is defined as:

$$BI(T) = \frac{\langle \rho T | \xi_l \leq \xi \leq \xi_u \rangle}{\langle \rho | \xi_l \leq \xi \leq \xi_u \rangle} \cdot \frac{1}{T_{\text{ref}}}, \quad (8.23)$$

where the limits $\xi_l = 0.3$ and $\xi_u = 0.4$ are the mixture fraction regime around the stoichiometry ($\xi_{\text{stoi}} = 0.365$). $T_{\text{ref}} = 2023\text{K}$ is a reference value for temperature, an adiabatic flame temperature of a premixed flame with stoichiometric mixture composition. $BI(T) = 1$ means complete burning solution, and $BI(T) = 0$ means extinction.

Figure 8.8 shows the experimental burning index of temperature for Sandia Flame D, E and F. We see that

- The $BI(T)$ for Sandia Flame D is almost equal to 1 everywhere, indicating that Flame D is a stable flame and a low degree of local extinction can be observed.

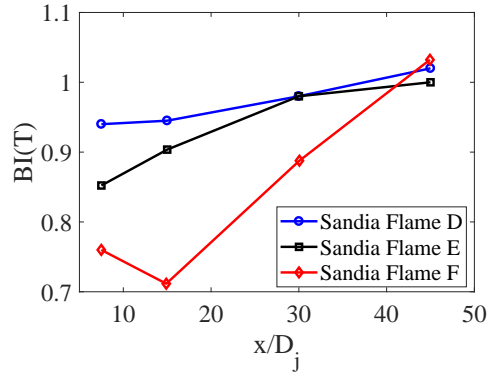


Figure 8.8: Experimental burning index of temperature for Sandia Flame D, E and F.

- The Sandia Flame E has lowest $BI(T)$ at $x/D_j = 7.5$ and increases along the centerline. At $x/D_j > 30$ the $BI(T)$ is approximately 1 and the Flame E up this point has a strong burning solution, while for $x/D_j = 7.5$ and $x/D_j = 15$ moderate degree of local extinction must be observed.
- The Sandia Flame F has very low burning index at $x/D_j = 7.5$ and $x/D_j = 15$, indicating that there are high degrees of local extinction at both positions. At $x/D_j = 30$, the $BI(T) \approx 0.9$ and the flame is re-ignited. And at $x/D_j = 45$ we again observe a stable and complete burning solution.

Therefore, burning index $BI(T)$ is a suitable quantity to quantify the local extinction and re-ignition phenomena.

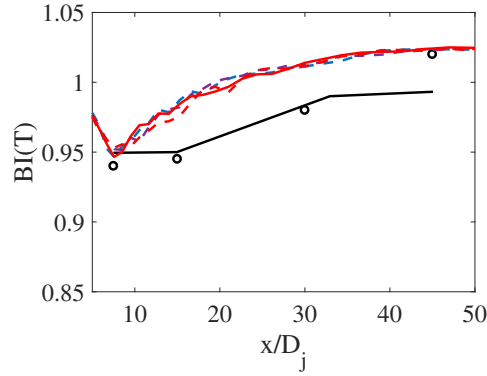


Figure 8.9: Burning index of temperature $BI(T)$ along the centerline for Sandia Flame D. Symbols: experimental results [6]. Black lines: results from [17]. Red dashed lines: using $\Pi_{Z_s}^\perp$ (GQL); Blue dashed lines: using $\Pi_{Z_s}^\perp$ (FGM); Purple dashed lines: $\Pi_{Z_s}^\perp$ (P&M); Red solid lines: Π_{TM}^\perp .

8.3.1 Sandia Flame D

In Fig.8.9 the predicted burning index of temperature $BI(T)$ using different projection strategies is compared together with experimental measurement (symbols) [6] and results from [17]. It is observed that for Sandia Flame D, there are minor differences between these strategies (note the scale of the axis) and all results show good agreements with experimental measurements and results from ISAT. The reason is that the Sandia Flame D is a stable flame and most of the thermo-kinetic states are located within the stable flame regime (c.f.8.6). This means, there is enough time for the chemical reaction during the turbulent mixing processes, and the evolution of thermo-kinetic states can be considered approximately along the tangential subspace of REDIM slow manifold \mathcal{M} . Therefore, projection strategies play minor role for Sandia Flame D.

Figures 8.10 and 8.11 show the conditional favre-averaged quantities over mixture fraction at three different locations ($x/D_j = 7.5, 15$ and 30) for Sandia Flame D. Consistent to the observation from burning index, simulation results have a very good agreement with those using ISAT [17] and experimental measurement, regardless which projection strategies are applied. The results show clearly that since Sandia Flame D is a relative stable turbulent flame with less degree of local extinction, its thermo-kinetic quantities can be well described by two-dimensional manifold (here 2D REDIM) and their evolutions are approximately along the tangential subspaces of manifold

so that projection process plays less role in the coupling between mixing processes in PDF model and manifold based simplified chemistry.

While most quantities are well predicted, the only noticeable deviation between simulation results (from using both ISAT and 2D REDIM) and experimental measurement can be observed for H₂. The reason can be attributed to the differential diffusion effect and the unity Lewis number assumption as a weak approximation for the prediction of H₂. A further investigation of differential diffusion effect and its influence on the prediction of H₂ will be discussed in Sec.8.5.

8.3 SIMULATION OF SANDIA FLAME SERIES BASED ON GRI 3.0 AND UNITY LEWIS NUMBER ASSUM

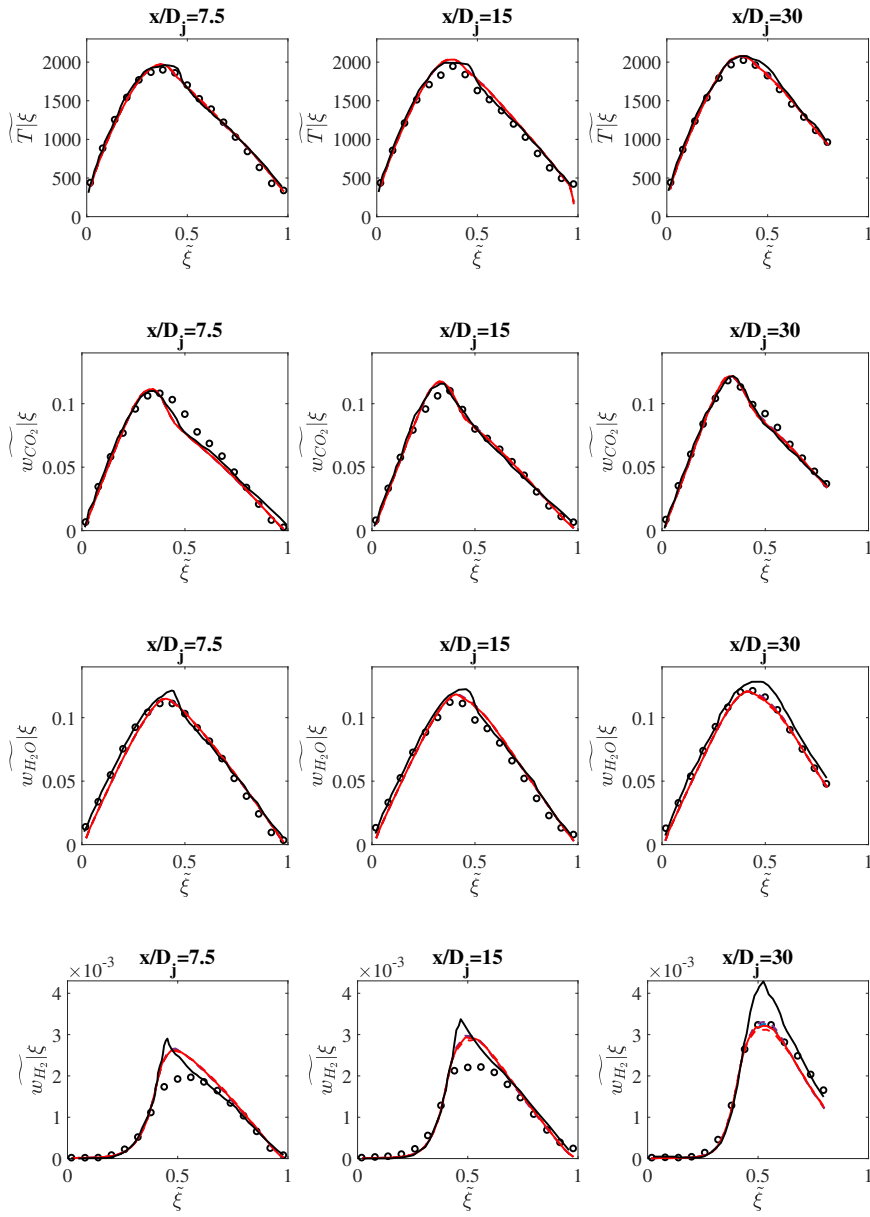


Figure 8.10: Conditional favre-averaged quantities over mixture fraction at three different locations for Sandia Flame D. Symbols: experimental results [6]. Black lines: results from [17]. Red dashed lines: using $\Pi_{Z_s}^\perp$ (GQL); Blue dashed lines: using $\Pi_{Z_s}^\perp$ (FGM); Purple dashed lines: $\Pi_{Z_s}^\perp$ (P&M). Red solid lines: $\Pi_{T_M}^\perp$.

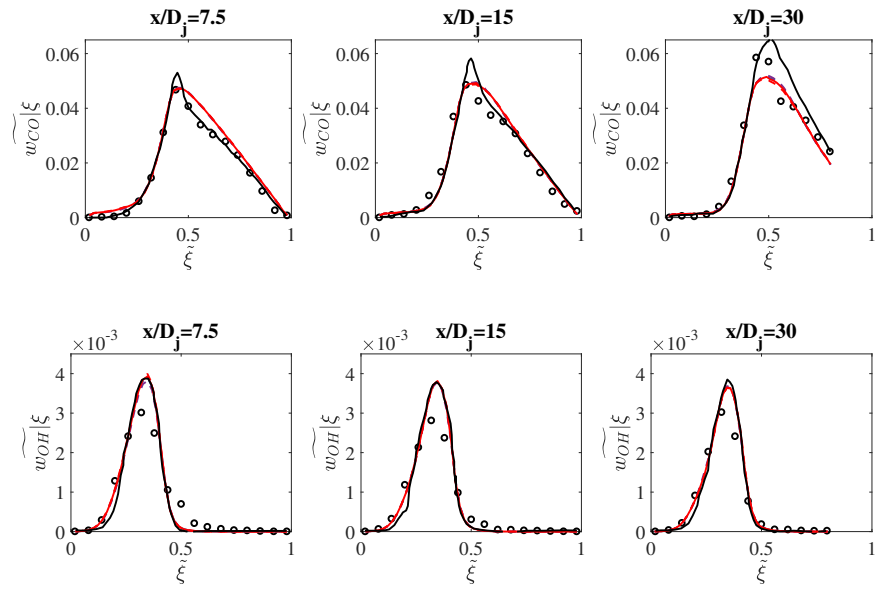


Figure 8.11: Conditional favre-averaged quantities over mixture fraction at three different locations for Sandia Flame D. Symbols: experimental results [6]. Black lines: results from [17]. Red dashed lines: using $\Pi_{Z_s}^\perp$ (GQL); Blue dashed lines: using $\Pi_{Z_s}^\perp$ (FGM); Purple dashed lines: $\Pi_{Z_s}^\perp$ (P&M). Red solid lines: Π_{TM}^\perp .

8.3.2 Sandia Flame E

Unlike Sandia Flame D in which most thermo-kinetic states are located within the stable flame regime and therefore with an extremely low degree of local extinction, in Sandia Flame E a moderate degree of local extinction can be observed at $x/D_j = 7.5$ and 15 (c.f. Fig.8.6) where a strong interaction between the mixing process and chemical reaction occurs. It can be clearly seen that the simulation using different projection strategies leads to different prediction on degree of local extinction. Especially at location $x/D_j = 7.5$ where strong interaction between mixing and reaction (and therefore occurrence of local extinction) takes place, it seems that simulation using projection strategy $\Pi_{Z_s}^\perp$ (P&M) (purple dashed line) predicts a higher burning index and therefore less degree of local extinction. This suggests that different prediction for conditional favre-averages can be observed using different projection strategies, which are summarized in Fig.8.13 and 8.14.

Conditional favre-averages at $x/D_j = 7.5$:

At position $x/D_j = 7.5$ where the highest degree of local extinction in Sandia Flame E can be observed, the conditional favre-averages are largely influenced by projection strategy used in the simulation. The results using $\Pi_{Z_s}^\perp$ (P&M) have the highest prediction values, indicating that a lower degree of local extinction can be predicted by using this projection strategy. The projection strategies $\Pi_{Z_s}^\perp$ (GQL) and $\Pi_{Z_s}^\perp$ (FGM) provide similar results and have over-prediction on H_2 , CO and OH. The best prediction is obtained using Π_{TM}^\perp (red solid lines), indicating that this projection strategy predicts the most realistic degree of local extinction.

Conditional favre-averages at $x/D_j = 15$:

At position $x/D_j = 15$ the local extinction can still be observed in a moderate degree but much less than in location $x/D_j = 7.5$. We observe that at this position both $\Pi_{Z_s}^\perp$ (FGM) and $\Pi_{Z_s}^\perp$ (P&M) predict more stable flame solutions and thus over-predict most conditional favre-averaged quantities. The projection strategies using $\Pi_{Z_s}^\perp$ (GQL) and Π_{TM}^\perp can still predict all conditional favre-averaged quantities with good accuracy, compared to simulation results using ISAT detailed chemistry and experimental measurement.

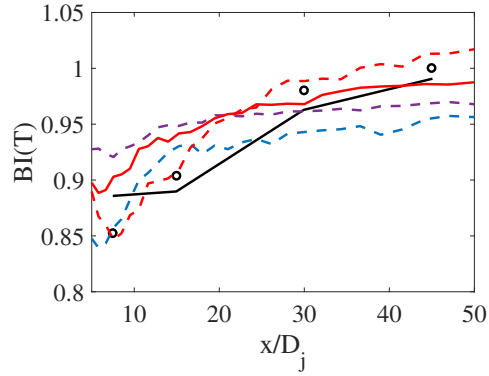


Figure 8.12: Burning index of temperature $BI(T)$ along the centerline for Sandia Flame E. Symbols: experimental results [6]. Black lines: results from [17]. Red dashed lines: using $\Pi_{Z_s}^\perp$ (GQL); Blue dashed lines: using $\Pi_{Z_s}^\perp$ (FGM); Purple dashed lines: $\Pi_{Z_s}^\perp$ (P&M). Red solid lines: Π_{TM}^\perp .

Conditional favre-averages at $x/D_j = 30$:

At location $x/D_j = 30$ flame has much less degree of local extinction and therefore most thermo-kinetic quantities are within the stable flame regime (c.f. temperature scatter plot in Fig.8.6). Therefore a good agreement between simulation results (regardless which projection strategies are used), simulation using ISAT detailed chemistry and experimental measurement can be observed.

8.3 SIMULATION OF SANDIA FLAME SERIES BASED ON GRI 3.0 AND UNITY LEWIS NUMBER ASSUM

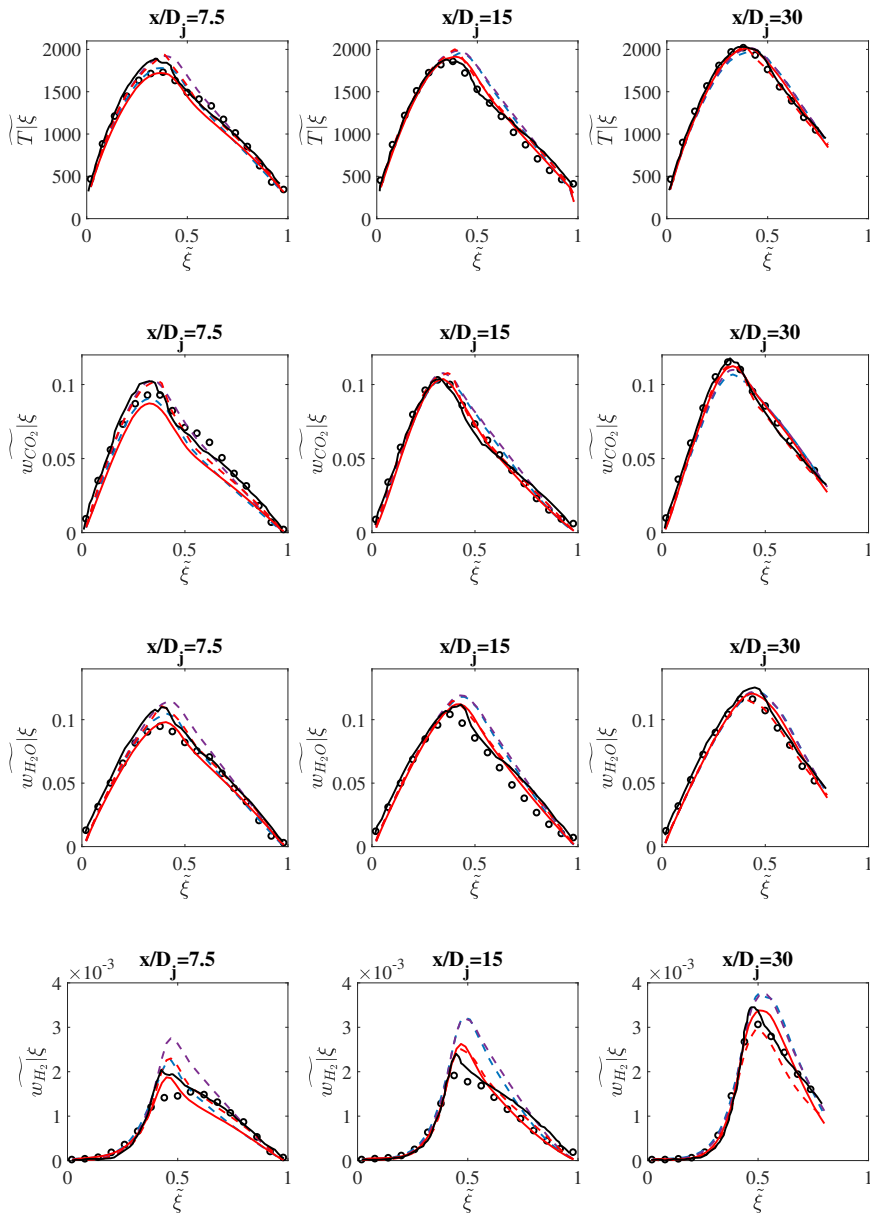


Figure 8.13: Conditional favre-averaged quantities over mixture fraction at three different locations for Sandia Flame E. Symbols: experimental results [6]. Black lines: results from [17]. Red dashed lines: using $\Pi_{Z_s}^\perp$ (GQL); Blue dashed lines: using $\Pi_{Z_s}^\perp$ (FGM); Purple dashed lines: $\Pi_{Z_s}^\perp$ (P&M). Red solid lines: $\Pi_{T_M}^\perp$.

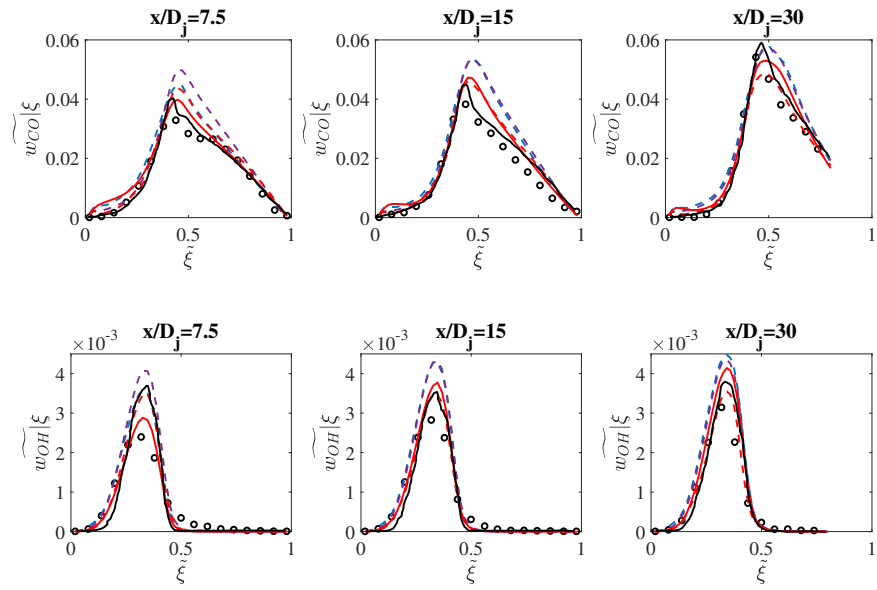


Figure 8.14: Conditional favre-averaged quantities over mixture fraction at three different locations for Sandia Flame E. Symbols: experimental results [6]. Black lines: results from [17]. Red dashed lines: using $\Pi_{Z_s}^\perp$ (GQL); Blue dashed lines: using $\Pi_{Z_s}^\perp$ (FGM); Purple dashed lines: $\Pi_{Z_s}^\perp$ (P&M). Red solid lines: Π_{TM}^\perp .

8.3.3 Sandia Flame F

Sandia Flame F is more challenging than Sandia Flames D and E due to its extremely high Reynolds number and therefore high degree of local extinction. Although typically Sandia Flame D and E can be predicted with good accuracy, prediction of thermo-kinetic quantities in Sandia Flame F still needs to be improved.

Different results have been published using different approaches, which are listed in Tab.8.2:

- In [17], RANS coupled with transported-PDF method is used for the flow field. In PDF model, the EMST mixing model and the ISAT detailed chemistry based on GRI 3.0 are used.
- In [28], LES coupled with filtered PDF is used for the flow field. In PDF model, conditional-moment-closure (CMC) as mixing model is used. The argumented reduced mechanism (ARM) deduced from GRI 3.0 [92] (ARM-1998) is applied for chemistry.
- In [29], LES coupled with filtered PDF is used for the flow field. In PDF model, multiple-mapping-conditioning (MMC) as mixing model is used. The detailed GRI 3.0 (NO_x excluded) chemistry is used.
- In [44], LES coupled with Eulerian stochastic field (ESF) is used for the flow field. IEM is used as mixing model. The argumented reduced mechanism deduced from GRI 3.0 [93] (ARM-2001) is applied for chemistry.

In Fig.8.2 examples of predicted conditional favre-averaged temperatures at positions $x/D_j = 7.5$ and $x/D_j = 15$ using different approaches listed in Tab.8.2 are compared. We notice that most approaches are not able to predict quantities with good accuracy at both positions at the same time. For example, LES-MMC (red lines) over-predicts conditional favre-averaged temperature at $x/D_j = 7.5$, indicating a lower predicted degree of local extinction than observed in experiments, while it has a better agreement at $x/D_j = 15$. For LES-CMC, it under-predicts at $x/D_j = 7.5$ and over-predicts at $x/D_j = 15$. The RANS-EMST is the only one that can predict quantities at both positions with good accuracy. This comparison shows that most published results (except at least RANS-EMST in [17]) have still large deviations for the prediction of thermo-kinetic quantities in Sandia Flame F.

The reason for the difficulty with prediction of Sandia Flame F can be attributed to its sensitivity to model parameters (mainly C_ϕ in mixing model),

	Approach	Mixing model	Chemistry	Ref.
RANS-EMST	RANS + TPDF	EMST	ISAT	[17]
LES-CMC	LES + FDF	CMC	ARM	[28]
LES-MMC	LES + FDF	MMC	full chemistry	[29]
LES-ESF	LES + ESF	IEM	ARM	[44]

Table 8.2: List of several different approaches as example used for simulation of Sandia Flame F. TPDF: transported-PDF method; FDF: filtered-PDF method; ESF: Eulerian stochastic field.

the set of boundary conditions (e.g. temperatures or species concentrations), complexity of chemistry (detailed or reduced chemistry) etc.

The most important novelty of this work is the improved prediction for Sandia Flame F. It will be shown below that with property projection process and higher dimension of REDIM, the thermo-kinetic quantities for Sandia Flame F can be largely improved for all positions.

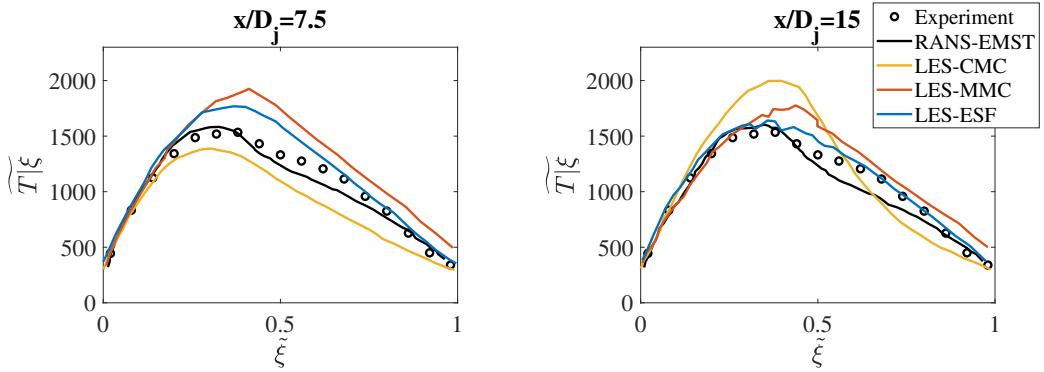


Figure 8.15: Conditional favre-averaged temperatures over mixture fraction at $x/D_j = 7.5$ (left) and $x/D_j = 15$ (right) for Sandia Flame F published using different approaches. Symbols: experimental results [6]. Black lines: RANS-EMST [17]; Yellow lines: LES-CMC [28]; Red lines: LES-MMC [29]; Blue lines: LES-ESF [44].

Burning index of temperature $BI(T)$

Figure 8.16 shows the predicted burning index of temperature for Sandia Flame F using different projection strategies. For positions far from jet exit (e.g. $x/D_j \geq 30$) where flame is re-ignited and a burning stable flame is observed, all projection strategies are able to capture this phenomenon, and

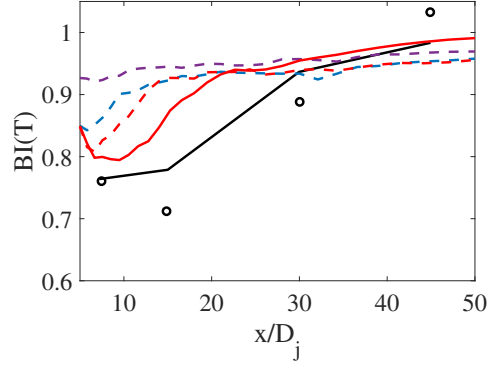


Figure 8.16: Burning index of temperature $BI(T)$ along the centerline for Sandia Flame F. Symbols: experimental results [6]. Black lines: results from [17]. Red dashed lines: using $\Pi_{Z_s}^\perp$ (GQL); Blue dashed lines: using $\Pi_{Z_s}^\perp$ (FGM); Purple dashed lines: $\Pi_{Z_s}^\perp$ (P&M). Red solid lines: Π_{TM}^\perp .

the burning index of temperature is predicted with similar quantities and agree with experiment measurement very well.

However, at positions $x/D_j = 7.5$ and $x/D_j = 15$ where a high degree of local extinction is observed in experiment, the predicted burning index is largely affected by projection strategy. For example, simulations using $\Pi_{Z_s}^\perp$ (P&M) provides the highest value of burning index, indicating a lower predicted degree of local extinction. Simulation using $\Pi_{Z_s}^\perp$ (GQL) provides the best among these three projection strategies in which thermo-kinetic states are projected back onto slow manifold in direction perpendicular to slow subspaces. A more better prediction is achieved by using Π_{TM}^\perp , which thermo-kinetic states are projected back onto manifold perpendicular to tangential subspace of manifold \mathcal{M} .

Noticeable different predictions of burning index indicate that especially at positions where high degree of local extinction occurs, projection strategy can largely affect the predicted degree of local extinction, and therefore conditional favre-averaged quantities (see below).

Conditional favre-averages at $x/D_j = 7.5$ and $x/D_j = 15$:

At both positions where high degree of local extinction takes place, simulations using $\Pi_{Z_s}^\perp$ strategy largely over-predict all quantities, as shown in Fig.8.17 and 8.18, although slow subspaces defined by using GQL approach (red dashed lines) allow the best prediction. Especially at $x/D_j = 15$ where the highest

degree of local extinction occurs (corresponding to the lowest value of burning index, c.f. Fig.8.16), some quantities (e.g. $\overline{w_{H_2}|\xi}$, $\overline{w_{CO}|\xi}$ and $\overline{w_{OH}|\xi}$) can be two times over-predicted.

A much better prediction can be achieved using projection strategy Π_{TM}^\perp , although at $x/D_j = 15$ quantities are still over-predicted.

Conditional favre-averages at $x/D_j = 30$:

At position $x/D_j = 30$ flame is re-ignited and a stable burning flame is obtained again. Therefore, it is observed from Fig.8.17 and 8.18 that prediction of most quantities agrees with results using ISAT detailed chemistry and is less sensitive to the definition of slow subspaces in projection strategy $\Pi_{Z_s}^\perp$. However, as also observed in results using ISAT and many other works such as [28, 29, 44, 76, 100], most quantities are over-predicted on the rich side ($\xi > 0.4$), which is still not fully understood and needs further investigation.

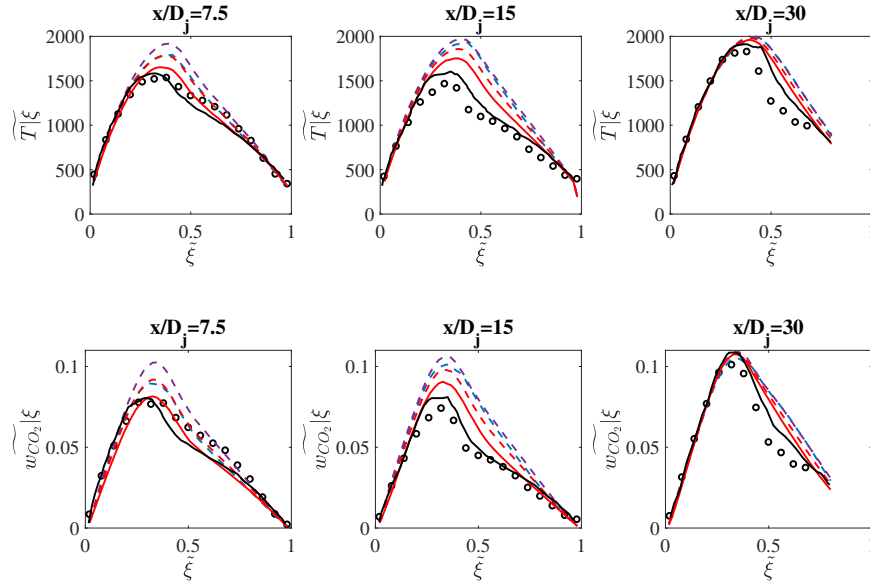


Figure 8.17: Conditional favre-averaged quantities over mixture fraction at three different locations for Sandia Flame F. Symbols: experimental results [6]. Black lines: results from [17]. Red dashed lines: using $\Pi_{Z_s}^\perp$ (GQL); Blue dashed lines: using $\Pi_{Z_s}^\perp$ (FGM); Purple dashed lines: $\Pi_{Z_s}^\perp$ (P&M). Red solid lines: Π_{TM}^\perp .

8.3 SIMULATION OF SANDIA FLAME SERIES BASED ON GRI 3.0 AND UNITY LEWIS NUMBER ASSUM

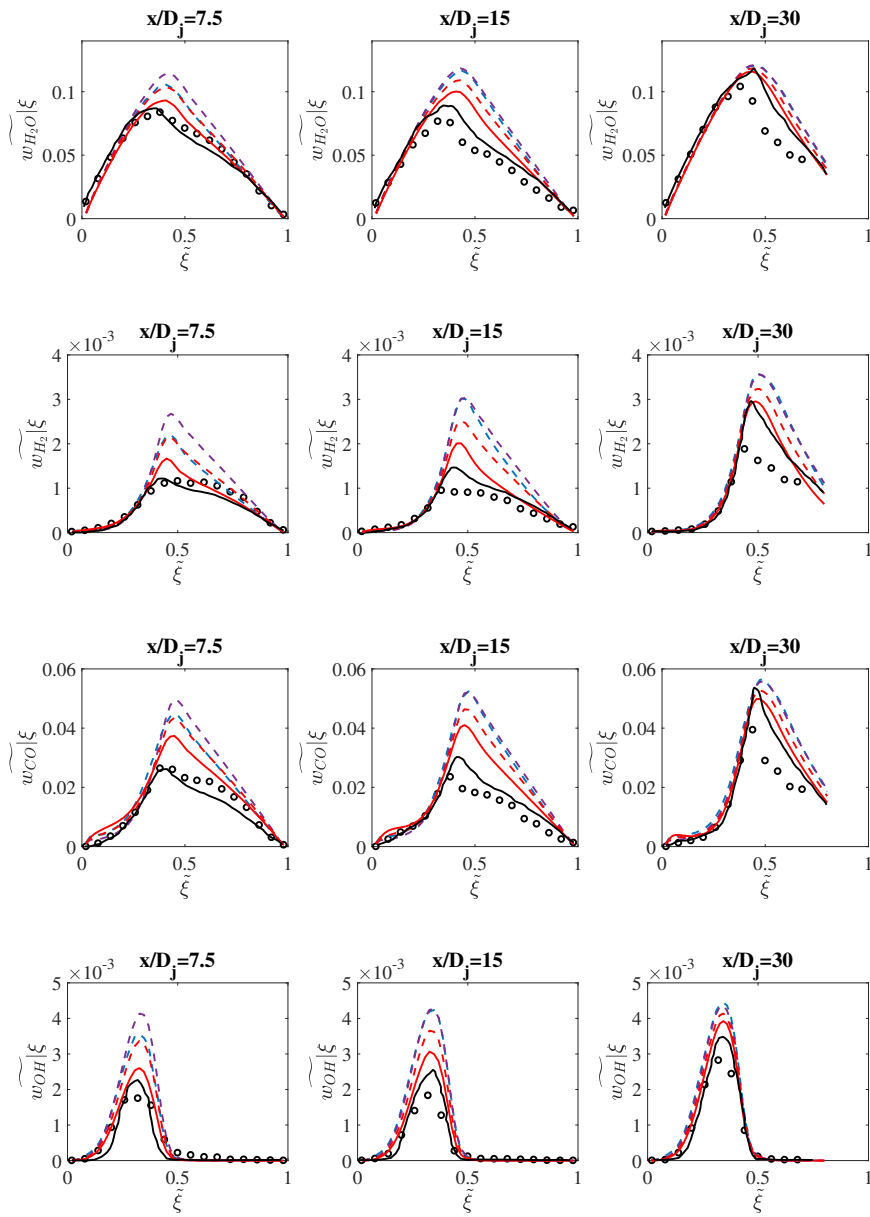


Figure 8.18: Conditional favre-averaged quantities over mixture fraction at three different locations for Sandia Flame F. Symbols: experimental results [6]. Black lines: results from [17]. Red dashed lines: using $\Pi_{Z_s}^\perp$ (GQL); Blue dashed lines: using $\Pi_{Z_s}^\perp$ (FGM); Purple dashed lines: $\Pi_{Z_s}^\perp$ (P&M). Red solid lines: Π_{TM}^\perp .

8.3.4 Discussion of the simulation results

To summarize the above results, it is shown that using an orthogonal projection Π_{TM}^\perp simulation results provide the best prediction. The reason why the orthogonal projection (Π_{TM}^\perp) yields good results can be explained by analyzing the mixing process and the reaction separately:

- The mixing model acts as a perturbation to the thermochemical states. However, diffusion processes pull the state back to the manifold in direction of the curvature vector, which is orthogonal to the manifold. The MP-projection performs an orthogonal projection.
- Concerning the chemical source term, it can be stated that the orthogonal vectors on the manifold (in an unscaled state space) point in the directions of the minor species. This means that an orthogonal back relaxation represents a good approximation for the fast relaxing chemical processes (which do not change the major species (slow variables)).

To summarize: both for physical perturbations and chemical perturbations an orthogonal projection back onto the manifold represents a good approximation.

However, although thermo-kinetic quantities for Sandia Flame D and E can be well predicted, large deviations can still be observed, especially at locations $x/D_j = 7.5$ and $x/D_j = 15$. Reason for this can be also observed from scatter plots. Figure 8.19 shows informations about how particles statistically distribute in the state space of $\xi - T$ -projection at position $x/D_j = 15$ as example. Two stable burning solutions of flame scenarios with very low (upper red lines) and extinction limit (lower red lines) strain rates are also shown. It is observed that for Sandia Flame D, most of scatter points are within stable burning scenarios, and 2D REDIM solution has a very good agreement with experimental measurement [6]. For Flame F, most of scatter points are scenarios below the extinction limit lines, indicating that a high degree of local extinction takes place. And 2D REDIM solution under-predicts local extinctions compared to experimental measurement. The reason for under-prediction of local extinction for Sandia Flame F can be explained through investigating physical and chemical time-scales.

Physical time scales can be approximately determined by the turbulent mixing time, which defined in Eq.8.24 as:

$$\tau_{\text{phy}} = \tau_\phi = \frac{1}{C_\phi} \cdot \frac{k}{\epsilon}. \quad (8.24)$$

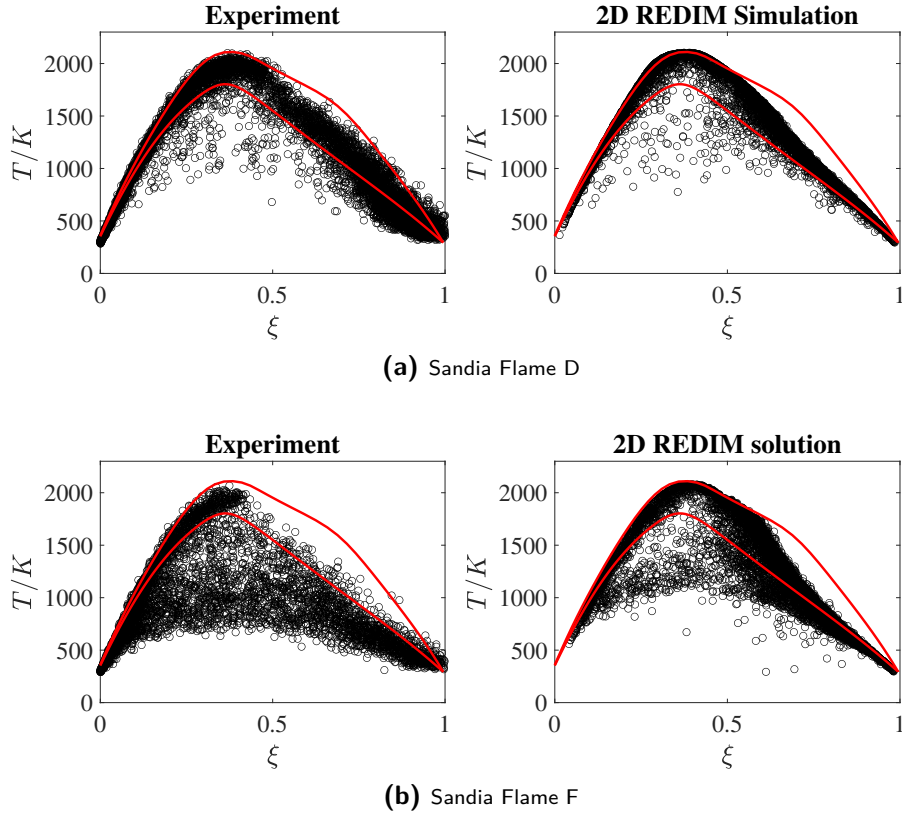


Figure 8.19: Scatter plots of temperature at $x/D_j = 15$ for Sandia Flame D (a) and F (b).

This physical time scale describes how fast scalar variance decays or, in other words, how fast scalars are mixed with each other under turbulence.

Chemical time scales describe how fast each chemical mode relaxes to equilibrium. As introduced above, the construction of manifold based simplified chemistry is based on the concept that all those chemical time-scales that are faster than physical time-scales can be decoupled from system. In other words, application of manifold based simplified chemistry is only valid, if the decoupled fast time-scales are indeed faster than physical time-scales, and the system is only governed by those time-scales which are in the similar or slower than physical time-scales. In order to investigate chemical time scale separation, the eigenvalues of local Jacobian matrix

$$\mathbf{S}_\Psi = \frac{\partial \mathbf{S}}{\partial \Psi} = \left(\frac{\partial \mathbf{S}_i}{\partial \Psi_j} \right)_{i,j} \quad (8.25)$$

of the chemical source term for time scales and dynamic decomposition are analysed on the REDIM manifold. It is found that the Jacobian matrix Eq. 8.25 on the REDIM has 6 eigenvalues exactly equal to zero, corresponding to the conserved quantities of the enthalpy, pressure and elements of C, H, O and N. The 7-th and 8-th eigenvalues correspond to two slow modes, and all other eigenvalues represent fast modes. However, the vector field of source term is not in the tangential subspace of slow manifold, one should project local Jacobian matrix in the tangential subspace of manifold

$$\Psi_{\theta}^{+} \cdot \mathbf{S}_{\Psi} \cdot \Psi_{\theta}$$

and normal subspace of manifold

$$(\Psi_{\theta}^{\perp})^{+} \cdot \mathbf{S}_{\Psi} \cdot \Psi_{\theta}^{\perp},$$

and calculate the corresponding eigenvalues. The eigenvalues obtained from the Jacobian matrix projected onto the normal space of manifold (λ_f) have two important meanings:

- If all these eigenvalues are negative $\lambda_f < 0$, then the manifold is an attracting stable manifold. This means, that all states that are located away from manifold will be attracted to the manifold.
- Their reciprocal values describe fast chemical time-scales $\tau_f = 1/|\lambda_f|$, indicating how fast states that are located away from manifold will be relaxed back onto manifold. If the absolute values of these eigenvalues are sorted in ascend way: $|\lambda_{f1}| > |\lambda_{f2}| > |\lambda_{f3}| > \dots$, then fast chemical time-scales are ordered as: $\tau_{f1} < \tau_{f2} < \tau_{f3} \dots$, indicating that τ_{f1} represents the slowest decoupled fast chemical time-scales for system to relax back onto manifold. Normally, $\tau_{f1} < \tau_{\text{phy}}$, ensuring that all fast chemical time-scales are faster than physical time-scales, so that these fast time-scales can be decoupled from systems.

In the following, physical and chemical time-scales are investigated at location $x/D_j = 15$ for Sandia Flame D and F. This position is selected because good agreement is observed for Sandia Flame D but large deviation for Sandia Flame F. Furthermore, at this position the highest degree of local extinction can be observed for Sandia Flame F. 6000 particles shown in Fig.8.19 are used for the investigation. For each particle its physical τ_{phy} and slowest decoupled fast chemical time-scales τ_{f1} are calculated. The PDF of τ_{phy} and τ_{f1} from these 6000 particles are determined.

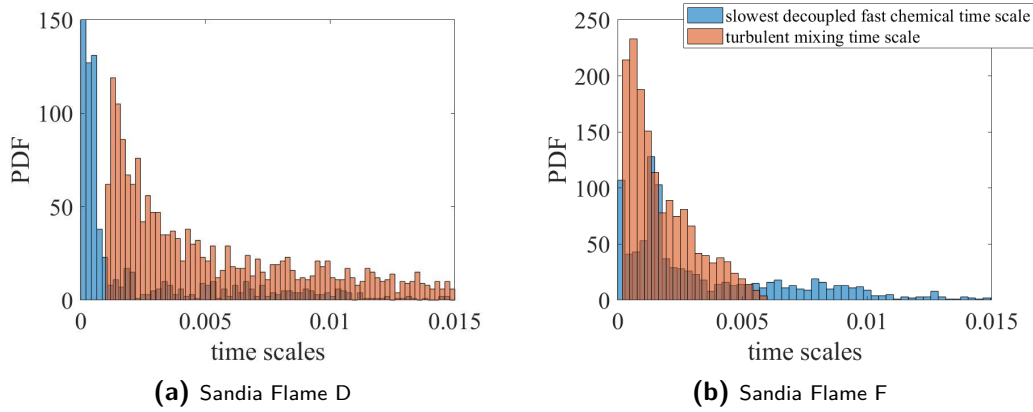


Figure 8.20: PDF of physical and chemical time-scales at $x/D_j = 15$.

Due to higher turbulence of Sandia Flame F, higher PDF (orange bar) of shorter turbulent mixing time scales is observed. Moreover, the PDF of slowest decoupled fast time scale τ_{f1} is also observed to be different for both flames. For Sandia Flame D, peak of PDF of τ_{f1} is located in order of magnitude $O(10^{-4})s$, which are mostly shorter than turbulent mixing time scales. Therefore, 2D REDIM is sufficient for simulation of Sandia Flame D. However, for Sandia Flame F, PDF of τ_{f1} ranges from order of magnitude $O(10^{-4})s$ to $O(10^{-3})s$, that are in the similar of turbulent mixing time scales. In this case, it is questionable whether τ_{f1} is reasonable to decouple from system. Therefore, it is necessary to construct a higher dimensional REDIM for the simulation of Sandia Flame F. Later in Sec.8.6 results using a 3D REDIM reduced chemistry for Sandia Flame F will be compared with those using a 2D REDIM reduced chemistry, and a significant improvement for the prediction of thermo-kinetic quantities using proper projection strategy can be obtained.

Mechanism	No. Species	Ref.
FFCM	38	[82]
SanDiego-2014	48	[106]
GRI 3.0	51	[81]

Table 8.3: Chemical mechanisms used in the calculation of Sandia Flame serie.

8.4 The influence of different detailed chemical mechanisms

Different detailed chemical mechanisms for one specific fuel can predict different flame structures and thermo-kinetic quantities such as temperatures and species concentrations. Although most of detailed mechanisms are intensively validated in homogeneous reactor and laminar flame calculation, their performance in modeling of turbulent flames is still of great interest. The main purpose of this section is to perform numerical simulation for Sandia Flame serie with different chemical mechanisms, studying the influence of different detailed mechanisms on thermo-kinetic quantities and re-ignition/extinction behaviors.

Besides the GRI 3.0 mechanism, two additional detailed mechanisms are used:

- The FFCM [82] is based on a comprehensive uncertainty quantification analysis and is validated against a large set of available combustion data over a wide range of conditions and phenomenon.
- The SanDiego-2014 mechanism [106] keeps the number of species and reactions as small as possible for the conditions relevant to flames, high temperature ignition and detonations.

Although these three detailed chemical mechanisms have been validated for ignition delay times, laminar flame speeds and so on, thermo-kinetic quantities such as temperatures and species concentrations can be predicted with different values. Therefore their performance in laminar counterflow diffusion flame will be first investigated and then in turbulent Sandia Flame, in order to answer the following two questions:

- Can the differences in the detailed chemistry also be represented by REDIM reduced chemistry?

8.4 THE INFLUENCE OF DIFFERENT DETAILED CHEMICAL MECHANISMS

- Are the differences of thermo-kinetic quantities such as temperatures and species concentrations in laminar diffusion flames consistent with those in turbulent diffusion flames?

To answer both questions, two 2D REDIM reduced chemistries are generated using FFCM and Sandiego-2014 at first, which will be used in the following numerical calculation.

Behavior for laminar counterflow diffusion flame

In order to relate the performance of these three mechanisms in turbulent flames to that in laminar flames, calculations have been performed for a steady laminar counter-flow diffusion flame, whose composition of the fuel steam is the same as that in the Sandia Flame [4], namely 25% methane and 75% air.

Figure 8.21 shows mass fractions of CO_2 , H_2 , CO and OH at position of stoichiometric mixture fraction in laminar counterflow diffusion flame for FFCM (red), SanDiego-2014 mechanism (yellow), and GRI 3.0 mechanism (blue). Symbols represent solutions using detailed chemical mechanisms, and lines using 2D REDIM reduced chemistry. The extinction strain rates are the right most points with numerical accuracy of $+10s^{-1}$. It is the last point for a stable flame, and a further increasement of $10s^{-1}$ for the strain rate will lead to extinction.

Several important issues can be observed:

- All these three have similar extinction strain rates.
- All these three chemical mechanisms predict CO_2 in similar quantities, while for other species shown here quantities are predicted in different manners. For example, FFCM predicts the highest value of OH , while GRI 3.0 mechanism the lowest value.
- 2D REDIM reduced chemistry has a very good agreement with detailed chemistry for all four mechanisms, showing that the differences in detailed chemistry can be actually captured by REDIM reduced chemistry.

Behavior for turbulent jet flames: Sandia Flame

The FFCM and Sandiego-2014 mechanisms are now performed for the simulation of Sandia Flame D, E and F. The projection perpendicular to tangential subspace (Π_{TM}^\perp) is used, and all model parameters are kept unchanged.

8 STUDY OF TURBULENT NON-PREMIXED CH₄-AIR FLAMES

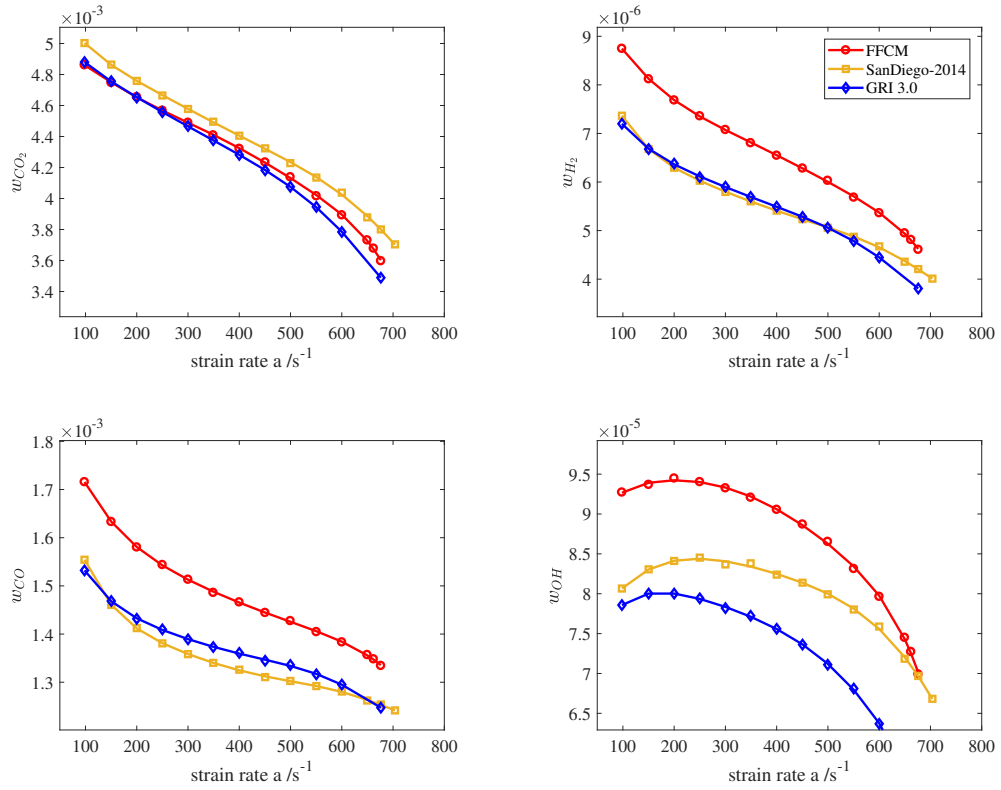


Figure 8.21: Mass fractions of different species at position of stoichiometric mixture fraction in laminar counterflow diffusion flame for FFCM (red), SanDiego-2014 mechanism (yellow), and GRI 3.0 mechanism (blue). Symbols: detailed chemistry; Lines: 2D REDIM reduced chemistry.

At first, the Burning Index (BI) for all three flames is compared in Fig.8.22. It is observed that the REDIM reduced chemistries of FFCM, SanDiego-2014 and GRI 3.0 mechanisms predict a similar trend of the burning index. This gives us the hint that all three mechanisms provide a similar degree of flame extinction. In other words, differences on predicted thermo-kinetics quantities from these three mechanisms are attributed to chemical mechanisms, but not to different predicted degree of flame extinction.

Figure 8.23 shows numerical prediction of species. Compared with results shown in Fig.8.21 for laminar calculations, a consistent prediction between laminar and turbulent simulation can be clearly observed. For CO₂ no large difference can be observed between different chemical mechanisms (compare Fig.8.21). For OH for example, FFCM predicts the highest values and GRI 3.0 the lowest values, which are consistent to prediction in laminar case (compare Fig.8.21).

8.4 THE INFLUENCE OF DIFFERENT DETAILED CHEMICAL MECHANISMS

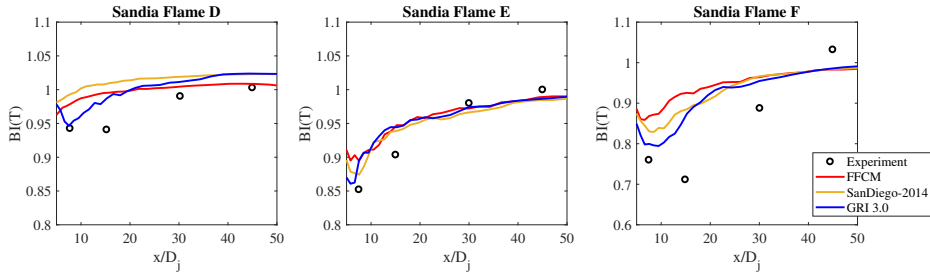


Figure 8.22: Predicted burning index of temperature $BI(T)$ using FFCM, Sandiego-2014 and GRI 3.0 mechanisms.

The results indicate that although different values of thermo-kinetic quantities can be predicted by different mechanisms, the REDIM reduction method is capable of capturing such differences. Furthermore, the differences of detailed chemistries can also be well observed in turbulent simulation by using REDIM reduced chemistry.

Another interesting thing to see is that since these mechanisms involve different numbers of species, how the computational efficiency will be affected if one uses 2D REDIMs generated from each mechanism. Here we define the normalized CPU time as the CPU time of each mechanisms normalized by the CPU time of mechanism with original lowest dimension (here FFCM mechanism with 38 dimension in original). We notice that the CPU time increases only linearly with increasing number of species of different mechanisms. It is because although a 2D REDIM (two progress variable) is used, in the calculation of evolution of composition state, we must evaluate the mixing process in full state space ($\varphi \rightarrow \Psi(\varphi)$) and then project onto the slow manifold based on $\Pi(\varphi) = \mathbf{C}_\varphi \cdot \Psi_\theta \cdot \Psi_\theta^+$. Therefore, an increased CPU time is caused by linear interpolation for these terms. However, we notice that the increasement of CPU is small, this is because REDIM reduced chemistry is stored using orthogonal and equi-distant mesh such that a point-by-point search is not required [10].

8 STUDY OF TURBULENT NON-PREMIXED CH₄-AIR FLAMES

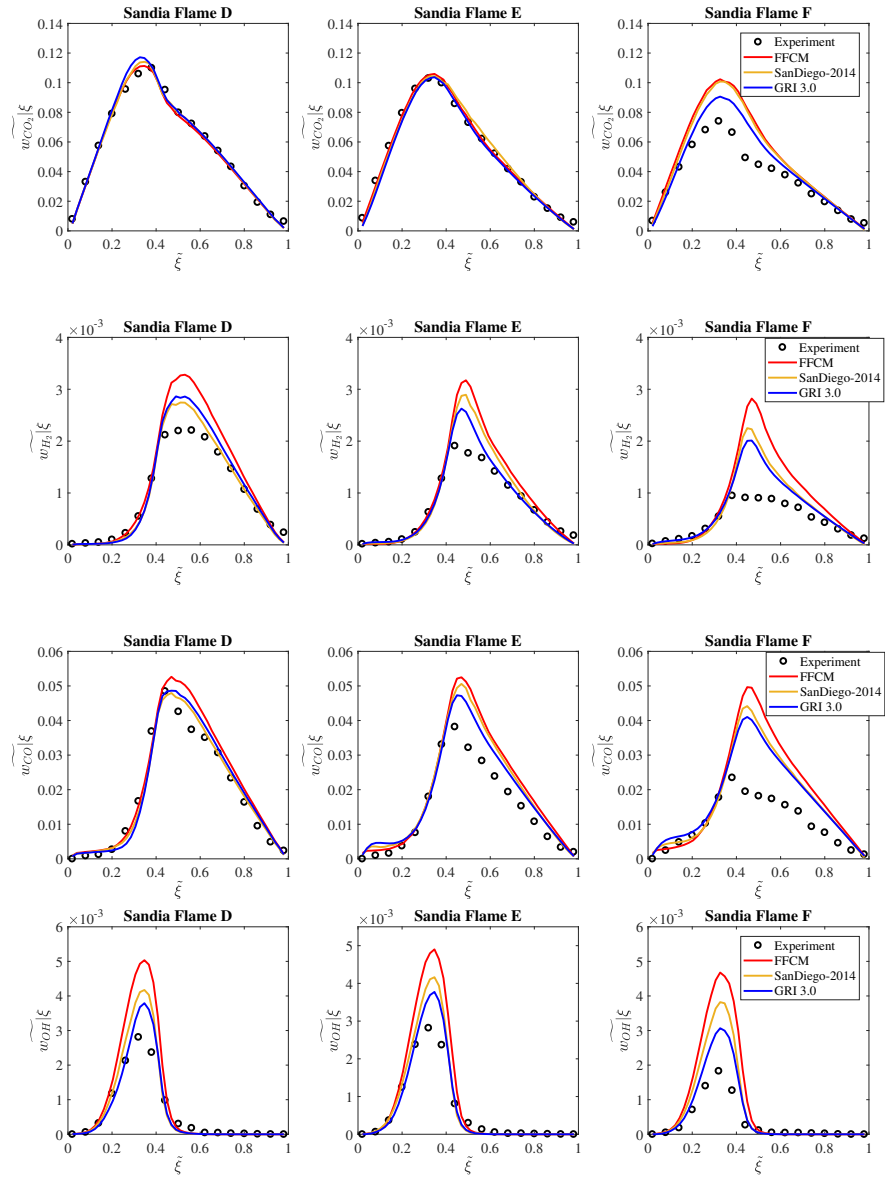


Figure 8.23: Conditional averaged values at position $r/D_j = 15$ for Sandia Flame D (left), E (middle) and F (right) based on FFCM mechanism (red lines), San Diego-2014 mechanism (yellow line) and GRI 3.0 mechanism (blue line).

8.4 THE INFLUENCE OF DIFFERENT DETAILED CHEMICAL MECHANISMS

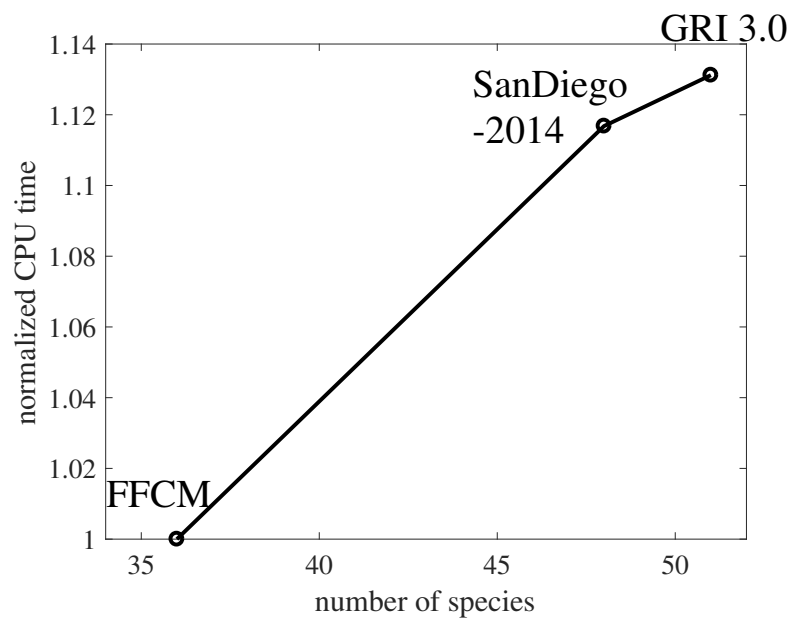


Figure 8.24: normalized CPU time against dimensions for FFCM, Sandiego-2014 and GRI 3.0 mechanisms.

8.5 The influence of molecular transport

Until now the equal-diffusivity assumption ($Le=1$) has been used in the numerical simulation. Although this unity-Lewis assumption is a suitable approximation for CH₄ flames, it is pointed out in [5] both from experiment and numerical calculations that this unity-assumption has some limitations, especially the over-prediction of H₂ concentrations. As studied in many works such as [68, 76, 101, 102], consideration of differential diffusion model can further improve the prediction of several species such as H₂ and OH. Therefore differential diffusion model as detailed transport including thermal diffusion in the generation of REDIM reduced chemistry is also tested. This model is based on the Curtiss-Hirschfelder approximation and the Soret effect is taken into account [39]. In [56] the numerical implementation of this differential diffusion model is described and investigated in details. In the following simulation, a 2D REDIM reduced chemistry based on differential diffusion transport model is generated and used for the numerical simulation.

Behavior for laminar counterflow diffusion flames

The influence of molecular transport is now first briefly investigated for laminar counterflow diffusion flame, whose composition of the fuel steam is again the same as that in the Sandia Flame [4], namely 25% methane and 75% air. Figure 8.25 shows the comparison of different species in mass fractions between using unity Lewis assumption (blue) and using differential diffusion transport model (red) for one strain rate $a = 300 \text{ s}^{-1}$ as an example. Symbols stand for detailed solutions, and lines for REDIM reduced solutions. We notice that for species like CO and CO₂, minor influence of molecular transport can be observed. However, for OH and especially for H₂, their behaviors are largely affected by transport model due to high diffusivity of light-weighted H and H₂, which are also confirmed in many other works such as [8, 20, 64, 80]. Therefore, from the observation in laminar flame calculation, it is expected that in the turbulent simulation noticeable influence should also be observed especially for H₂ species concentration.

Behavior for Sandia Flame

In this part, the REDIM generated using differential diffusion transport model is applied for the simulation of Sandia Flame D, E and F. Prediction of mass fractions of CO (Fig.8.26), OH (Fig.8.27) and H₂ (Fig.8.28) using 2D REDIM with unity-Lewis number (blue lines) and 2D REDIM with differential

8.5 THE INFLUENCE OF MOLECULAR TRANSPORT

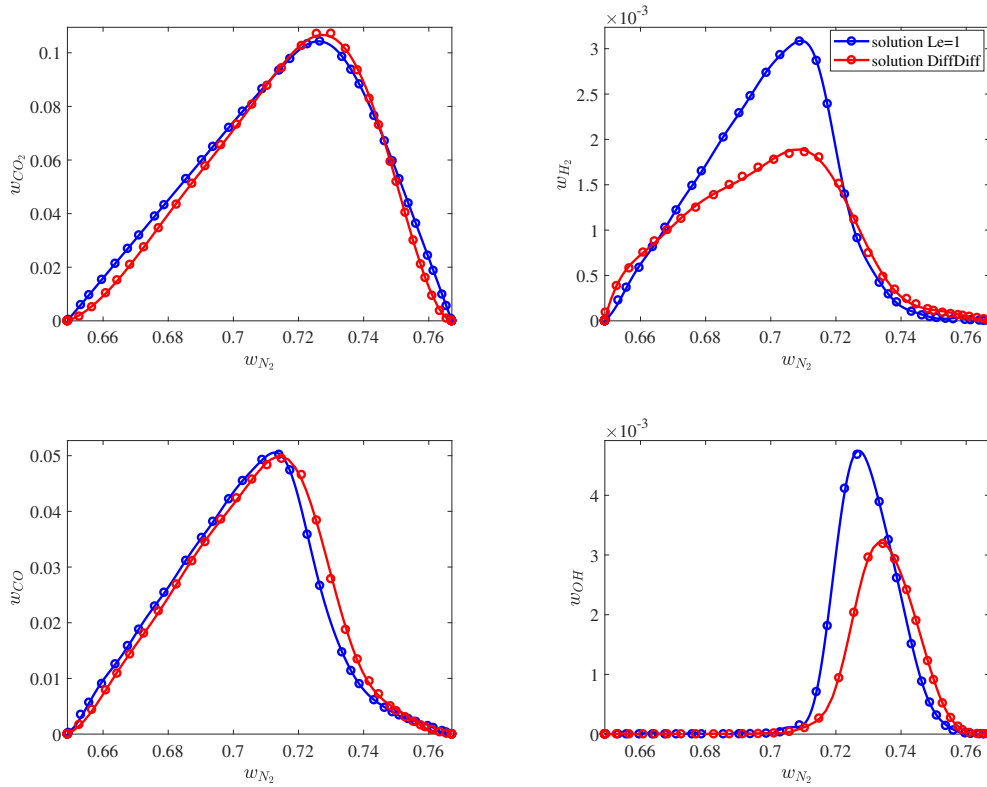


Figure 8.25: Mass fractions of different species over mass fraction of N_2 (w_{N_2}) in laminar counterflow diffusion flame under strain rate $a = 300 \text{ s}^{-1}$. Symbols: detailed chemistry; Lines: 2D REDIM reduced chemistry. Blue: transport model with $Le=1$; Red: differential diffusion (DiffDiff) transport model.

diffusion detailed transport model (red lines) are compared together with experimental measurements (symbols) [6].

Consistent with the observation in laminar flame calculation, the influence of molecular transport on CO is negligible small. While species OH are influenced moderately by molecular transport, species H is significantly affected by molecular transport due to its high diffusivity. However, it can be clearly observed that the mass fractions of H are largely over-predicted by using differential diffusion detailed transport model at lean sides. This can be attributed to the model parameter C_ϕ in the mixing model. Although in the generation of REDIM reduced chemistry differential diffusion detailed transport model is included, in the calculation of mixing model a constant C_ϕ is still used, which means that in the mixing model all thermo-kinetic states (enthalpy h and species concentrations) have the same scalar dissipation

rate [73, 101, 102]. Therefore in order to be consistent between REDIM and mixing models for differential diffusion effect, differential diffusion effect must also be introduced into the mixing models (one possible strategy is investigated in [101] showing good results for Sandia Flame simulation).

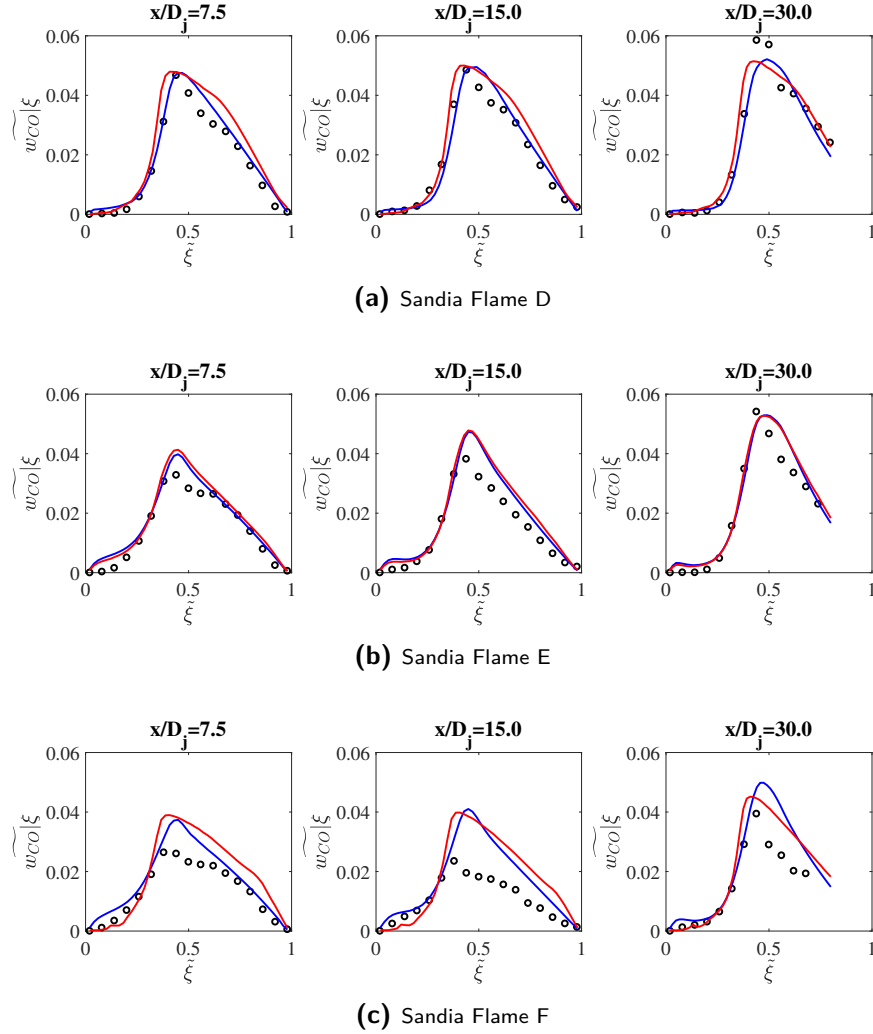


Figure 8.26: Conditional favre-averaged mass fractions of CO over mixture fraction at three different locations for Sandia Flame D, E and F. Symbols: experimental measurements [6]; Blue lines: solution using 2D REDIM with unity-Lewis number; Red lines: solution using 2D REDIM with differential diffusion detailed transport model.

8.5 THE INFLUENCE OF MOLECULAR TRANSPORT

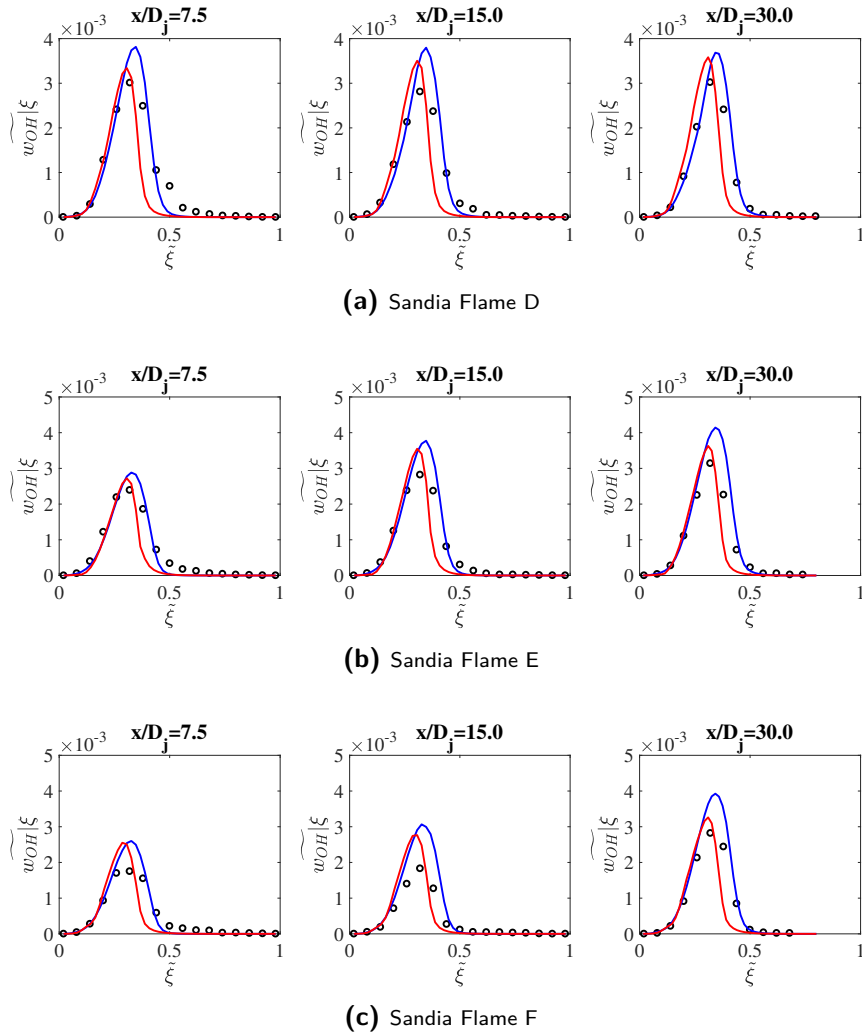


Figure 8.27: Conditional favre-averaged mass fractions of OH over mixture fraction at three different locations for Sandia Flame D, E and F. Symbols: experimental measurements [6]; Blue lines: solution using 2D REDIM with unity-Lewis number; Red lines: solution using 2D REDIM with differential diffusion detailed transport model.

8 STUDY OF TURBULENT NON-PREMIXED CH₄-AIR FLAMES

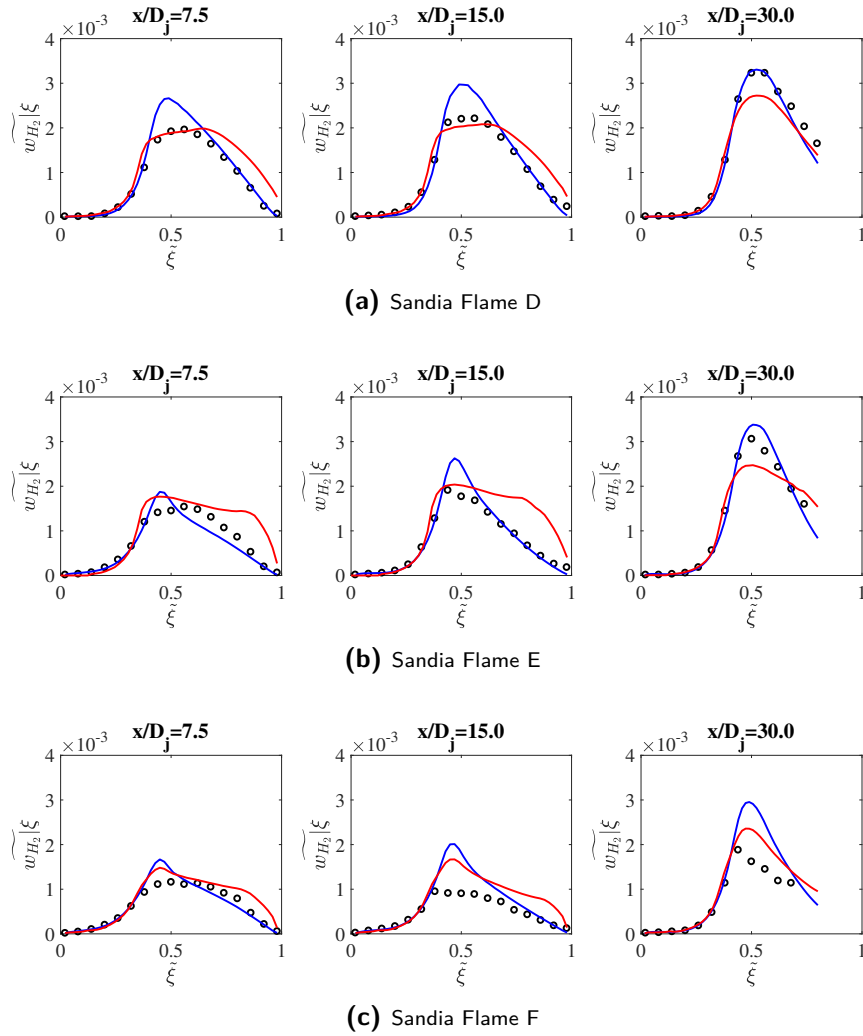


Figure 8.28: Conditional favre-averaged mass fractions of H₂ over mixture fraction at three different locations for Sandia Flame D, E and F. Symbols: experimental measurements [6]; Blue lines: solution using 2D REDIM with unity-Lewis number; Red lines: solution using 2D REDIM with differential diffusion detailed transport model.

8.6 The influence of dimension of REDIM reduced chemistry

The above numerical results showed that a 2D REDIM reduced chemistry is sufficient for the prediction of thermo-kinetic quantities for Sandia flame D and E (c.f. Fig.8.10 - 8.14), a two-dimensional state space (2D REDIM) can result in inaccuracies for flow with high turbulence (here Sandia Flame F), although the Π_{TM}^\perp projection strategy yields better results than the projection strategy using $\Pi_{\tilde{Z}_s}^\perp$.

In this section, a 3D REDIM reduced chemistry is generated and used for the simulation of Sandia Flame F. To discuss the results, the results using a 2D REDIM and a 3D REDIM reduced chemistry are compared. Different projection strategies are also shown together in the Fig.8.29 and 8.30.

For this comparison, the $\Pi_{\tilde{Z}_s}^\perp$ (FGM) is selected as candidate for the $\Pi_{\tilde{Z}_s}^\perp$ projection strategy. In the 3D REDIM, the third reduced coordinate $\theta = \phi_{\text{OH}}$ and the third progress variable $\varphi = \phi_{\text{OH}}$ are selected. Again, this means that using the $\Pi_{\tilde{Z}_s}^\perp$ projection strategy the system states are projected back onto the manifold in direction where all three reduced coordinates $(\theta_1, \theta_2, \theta_3)^\text{T} = (\phi_{\text{N}_2}, \phi_{\text{CO}_2} + \phi_{\text{H}_2\text{O}} + \phi_{\text{H}_2}, \phi_{\text{OH}})^\text{T}$ remain constant. When using Π_{TM}^\perp , the system states are projected back onto the slow manifold in directions normal to the tangential subspace of the slow manifold.

Figures 8.29 and 8.30 show two important observations:

- With the same projection strategy, results using the 3D REDIM reduced chemistry are much accurate than those using the 2D REDIM reduced chemistry.
- Consistent with the results observed in Sec. 8.3.1, 8.3.2 and 8.3.3, the Π_{TM}^\perp projection strategy (color solid lines) yields better results than the projection strategy using $\Pi_{\tilde{Z}_s}^\perp$ (color dashed lines) and agree with the ISAT detailed chemistry results very well for all three positions.

These results show clearly the use of a 3D REDIM reduced chemistry combined with Π_{TM}^\perp projection strategy is necessary for the accurate prediction of Flame F.

8 STUDY OF TURBULENT NON-PREMIXED CH₄-AIR FLAMES

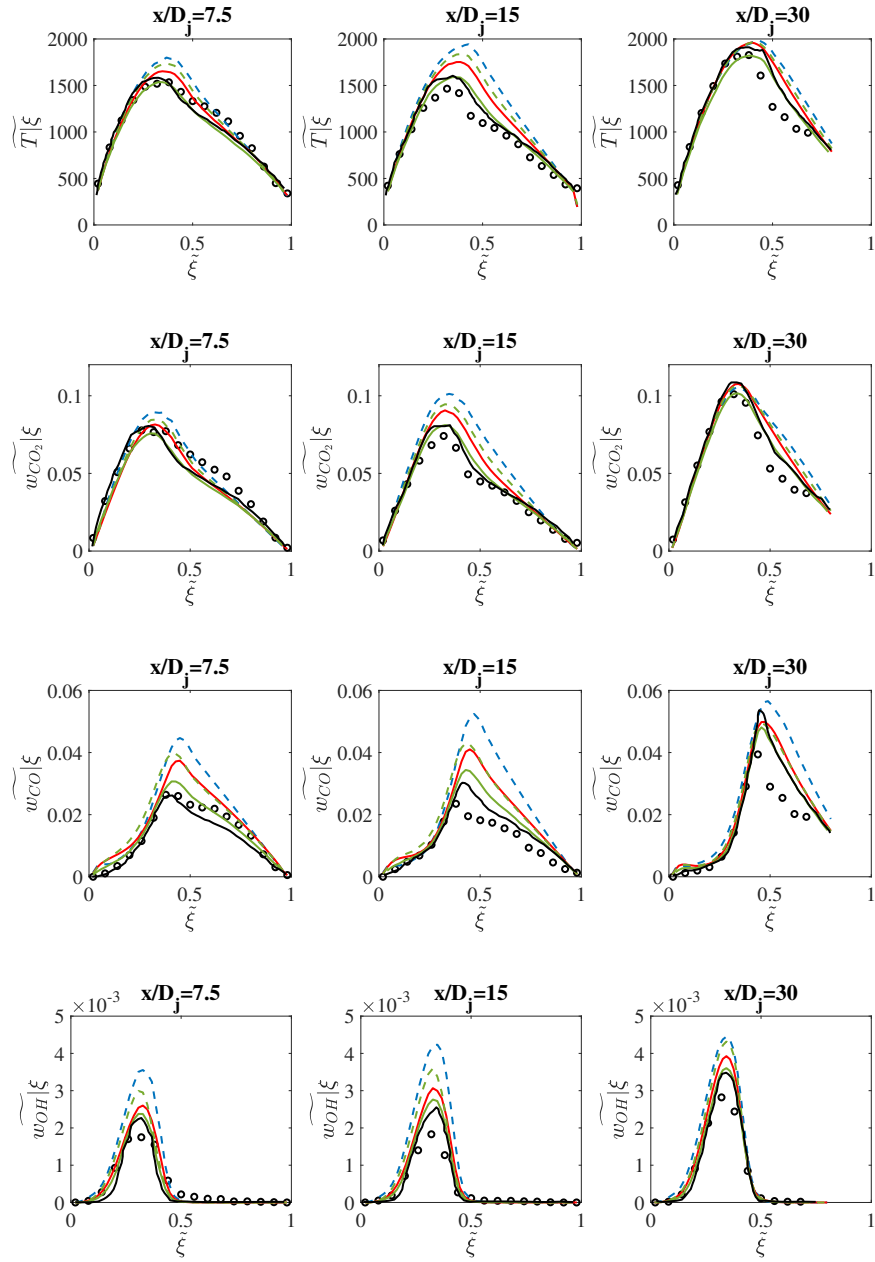


Figure 8.29: Conditional favre-averaged quantities over mixture fraction at three different locations for Sandia Flame F using 2D and 3D REDIM. Symbols: experimental results [6]. Black lines: results from [17]. Blue dashed lines: 2D REDIM using $\Pi_{Z_s}^\perp$ (FGM); Red solid lines: 2D REDIM using Π_{TM}^\perp ; Green dashed lines: 3D REDIM using $\Pi_{Z_s}^\perp$ (FGM); Green solid lines: 3D REDIM using Π_{TM}^\perp .

8.6 THE INFLUENCE OF DIMENSION OF REDIM REDUCED CHEMISTRY

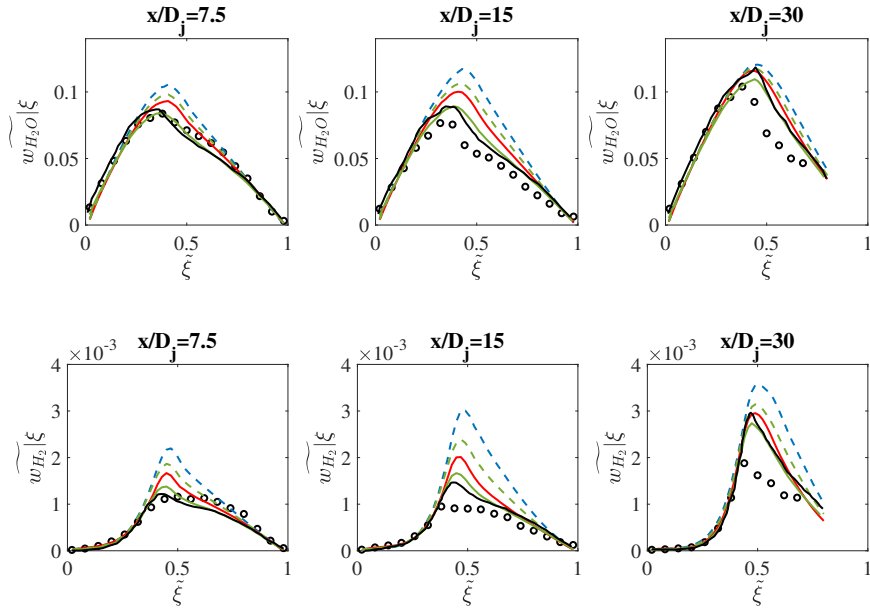


Figure 8.30: Conditional favre-averaged quantities over mixture fraction at three different locations for Sandia Flame F using 2D and 3D REDIM. Symbols: experimental results [6]. Black lines: results from [17]. Blue dashed lines: 2D REDIM using $\Pi_{Z_s}^\perp$ (FGM); Red solid lines: 2D REDIM using Π_{TM}^\perp ; Green dashed lines: 3D REDIM using $\Pi_{Z_s}^\perp$ (FGM); Green solid lines: 3D REDIM using Π_{TM}^\perp .

9 Conclusion and Outline

This dissertation focuses on the numerical simulation of turbulent reacting flows based on a hybrid FVM/transported-PDF method. REDIM reduced chemistry is used as an efficient tool to solve the complex chemistry modeling. The main contribution of this thesis is the investigation of coupling between turbulent mixing processes and reduced chemistry.

Both turbulent mixing and reduced chemistry are studied and developed separately, and there are few studies involving coupling problem between both processes. Despite of limited studies, these studies show clearly that an over-simplification for coupling of both processes would lead to qualitative and quantitative errors, and thus inaccuracy of numerical prediction. Because of this reason, a systematic investigation of coupling between turbulent mixing and reduced chemistry is conducted and its influence on numerical accuracy has been validated through a turbulent non-premixed jet piloted CH_4 flame (Sandia Flame D, E and F).

The importance of coupling between turbulent mixing and reduced chemistry originates from the fact that the thermo-kinetic states are restricted to the slow manifold while turbulent mixing causes these state departure from the slow manifold. Therefore, thermo-kinetic states that are away from manifold must be projected back onto manifold. The most significant question is that how thermo-kinetic states are projected back onto manifold. In other words, along which direction these states are projected. In this thesis, two strategies are proposed:

- One way is to project thermo-kinetic states back onto slow manifold in direction that certain components of the state vector do not change. The most suitable way to define this direction is to find out slow subspaces which are compatible with the fast and slow decomposition of system dynamics. The Global Quasi-linearization (GQL) approach is suggested to define this slow subspaces that are based on time-scales analysis.
- The other way is to project thermo-kinetic states back onto slow manifold in direction that are perpendicular to tangential subspaces of manifold (orthogonal projection). Compared to the first variant, this

9 CONCLUSION AND OUTLINE

orthogonal projection requires no additional information, and projection direction is determined merely by manifold itself.

Both projection strategies have been performed for the simulation of Sandia Flame D, E and F, whose degree of local extinction varies from low to high. For reduced chemistry, a two-dimensional (2D) REDIM is applied. Sandia Flame D has a low degree of local extinction and thus a stable turbulent flame, numerical simulation is not sensitive to the choice of projection strategies. With increasing degree of local extinction, projection strategies for the coupling of turbulent mixing process and reduced chemistry become important and significant. Numerical simulations show that an optimized slow subspaces for the definition of projection can improve accuracy, while the best results are achieved by using orthogonal projection.

Although an orthogonal projection strategy can enhance numerical accuracy, it is observed that thermo-kinetic quantities in Sandia Flame F are still over-predicted. The reason for that can be explained by investigating physical and chemical time-scales. For Sandia Flame D where low degree of low extinction occurs, fast chemical time-scales are much shorter than physical time scales (turbulent mixing time scales). Hence, 2D REDIM is sufficient for the simulation of Sandia Flame D and E. However, for Sandia Flame F, the longest fast time-scales are in the similar order of magnitude of turbulent mixing time-scales. This indicates that a higher dimensional REDIM (at least 3D REDIM) is necessary. The results using an orthogonal projection for Sandia Flame F based on a 3D REDIM reduced chemistry shows indeed good accuracy compared to ISAT detailed chemistry results and experimental measurement.

Futhermore results concern investigating of differential diffusion effect on the flame structure. A 2D REDIM is generated using detailed transport model. It is observed that light molecules such as H_2 are very sensitive to the applied diffusion transport model. REDIM generated from detailed transport model brings much better results for the prediction of H_2 concentration than REDIM generated using unity Lewis number assumption.

Bibliography

- [1] Anderson, J.D. and Wendt, J., *Computational fluid dynamics*. New York: McGraw-Hill, 1995.
- [2] Attili, A., Bisetti, F., Mueller, M. E., and Pitsch, H., "Formation, growth, and transport of soot in a three-dimensional turbulent non-premixed jet flame". In: *Combustion and flame*, 161.7, 1849-1865, 2014.
- [3] Balje, O. E., "A Study on Reynolds Number Effects in Turbomachines". In: *ASME. Journal of Engineering for Gas Turbines and Power*, 86.3, 227-235, 1964.
- [4] Barlow, R. S., and Frank, J.H., "Effects of turbulence on species mass fractions in methane/air jet flames". In: *Symposium (International) on Combustion*, 27.1, 1087-1095, 1998.
- [5] Barlow, R. S., Frank, J. H., Karpetis, A. N., and Chen, J. Y., "Piloted methane/air jet flames: Transport effects and aspects of scalar structure". In: *Combustion and Flame*, 143.4, 433-449, 2005.
- [6] Barlow, R. S., "International workshop on measurement and computation of turbulent nonpremixed flames". <http://www.ca.sandia.gov/TNF/abstract.html>, 2003. accessed April 01, 2016.
- [7] Bender, R., Blasenbrey, T. and Maas, U., "Coupling of detailed and ILDM-reduced chemistry with turbulent mixing". In: *Proceedings of the Combustion Institute*, 28.1, 101-106, 2000.
- [8] Bell, J. B., Cheng, R. K., Day, M. S., and Shepherd, I. G., "Numerical simulation of Lewis number effects on lean premixed turbulent flames". In: *Proceedings of the Combustion Institute*, 31.1, 1309-1317, 2007.
- [9] Bodenstein, M., "Eine theorie der photochemischen reaktionsgeschwindigkeiten". In: *Zeitschrift für physikalische Chemie*, 85.1, 329-397, 1913.

BIBLIOGRAPHY

- [10] Bykov, V., and Maas, U., "The extension of the ILDM concept to reaction–diffusion manifolds". In: *Combustion Theory and Modelling*, 11.6, 839-862 2007.
- [11] Bykov, V., Goldshtein, V. and Maas, U., "Simple global reduction technique based on decomposition approach", In: *Combustion Theory and Modelling*, 12.2, 389-405, 2008.
- [12] Bykov, V. and Maas, U., "Investigation of the hierarchical structure of kinetic models in ignition problems". In: *Zeitschrift für Physikalische Chemie*, 223.4-5, 461-479, 2009
- [13] Bykov, V. and Goldshtein, V., "Fast and slow invariant manifolds in chemical kinetics". In: *Computers and Mathematics with Applications*, 65.10, 1502-1515, 2013.
- [14] Bykov, V., Neagos, A. and Maas, U., "On transient behavior of non-premixed counter-flow diffusion flames within the REDIM based model reduction concept". In: *Proceedings of the Combustion Institute*, 34.1, 197-203, 2013.
- [15] Cengel, Y. A., and Boles, M.A., *Thermodynamics: An Engineering Approach 4th Edition in SI Units*. Singapore (SI): McGraw-Hill, 2002.
- [16] Cant, R. S., and Mastorakos, E., *An introduction to turbulent reacting flows*, London: Imperial College Press, 2008.
- [17] Cao, R.R. and Pope, S.B., "The influence of chemical mechanisms on PDF calculations of nonpremixed piloted jet flames". In: *Combustion and Flame*, 143.4, 450-470, 2005.
- [18] Celis, C. and da Silva, L.F.F., "Lagrangian mixing models for turbulent combustion: review and prospects". In: *Flow, Turbulence and combustion*, 94.3, 643-689, 2015.
- [19] Chapman, D. L. and Underhill, L. K., "The interaction of chlorine and hydrogen. The influence of mass". In: *Journal of the Chemical Society, Transactions*, 103, 496-508, 1913.
- [20] Chen, Z., "Effects of hydrogen addition on the propagation of spherical methane/air flames: a computational study". In: *International journal of hydrogen energy*, 34.15, 6558-6567, 2009.

- [21] Cleary, M. J. and Klimenko, A.Y., "A generalised multiple mapping conditioning approach for turbulent combustion". In: *Flow, turbulence and combustion*, 82.4, 477, 2009.
- [22] Curl, R. L., "Dispersed phase mixing: I. Theory and effects in simple reactors". In: *AIChE journal*, 9.2, 175-181, 1963.
- [23] De Meester, R., Naud, B. Maas, U. and Merci, B., "Transported scalar PDF calculations of a swirling bluff body flame ('SM1') with a reaction diffusion manifold". In: *Combustion and Flame*, 159.7, 2415–2429, 2012.
- [24] Deuffhard, P., Bornemann, F. *Numerische Mathematik. Band 2: Gewöhnliche Differentialgleichungen*. 2. vollständige überarbeitete und erweiterte Auflage. Berlin: de Gruyter 2002.
- [25] Dopazo, C. and O'Brien E.E., "An approach to the autoignition of a turbulent mixture". In: *Acta Astronautica*, 1.9-10, 1239-1266, 1974.
- [26] Ferziger, J. H., Peric, M. and Street, R.L. *Computational methods for fluid dynamics*. 3. Berlin: Springer, 2002.
- [27] Fox, R.O., and Stiles, H.L., *Computational models for turbulent reacting flows*. Vol. 1. Cambridge: Cambridge university press, 2003.
- [28] Garmory, A. and Mastorakos, E., "Sensitivity analysis of LES–CMC predictions of piloted jet flames". In: *International journal of heat and fluid flow*, 39, 53-63, 2013.
- [29] Ge, Y., Cleary, M. J. and Klimenko, A. Y., "A comparative study of Sandia flame series (D–F) using sparse-Lagrangian MMC modelling". In: *Proceedings of the Combustion Institute*, 34.1, 1325-1332, 2013.
- [30] Ghorbani, A., Steinhilber, G., Markus, D., and Maas, U., "Numerical investigation of ignition in a transient turbulent jet by means of a PDF method". In: *Combustion Science and Technology*, 186.10-11, 1582-1596, 2014.
- [31] Giaquinta, M. and Modica, G., *Mathematical analysis: functions of one variable*. New York: Springer Science & Business Media, 2012.
- [32] Gicquel, O., Darabiha, N. and Thevenin, D., "Liminar premixed hydrogen/air counterflow flame simulations using flame prolongation of ILDM with differential diffusion". In: *Proceedings of the Combustion Institute*, 28.2, 1901-1908, 2000.

BIBLIOGRAPHY

- [33] Golda, P., Blattmann, A., Neagos, A., Bykov, V., and Maas, U., "Implementation problems of manifolds-based model reduction and their generic solution". In: *Combustion Theory and Modelling*, 2019. DOI:<https://doi.org/10.1080/13647830.2019.1682198>.
- [34] Golub, G.H. and van Loan, C.F., *Matrix computation*, Baltimore, London: The Hopkins University Press, 1989.
- [35] Goussis, D. A. and Maas, U., "Model reduction for combustion chemistry". In: *Turbulent combustion modeling*, 193-220, Dordrecht: Springer, 2011.
- [36] Gorban, A. N. and Karlin, I. V., "Method of invariant manifold for chemical kinetics". In: *Chemical Engineering Science*, 58.21, 4751-4768, 2003.
- [37] Hack, M.L., *Joint probability density function (PDF) closure of turbulent premixed flames*. Dissertation. ETH Zurich, 2011.
- [38] Haworth, D.C., "Progress in probability density function methods for turbulent reacting flows". In: *Progress in Energy and Combustion Science*, 36.2, 168-259, 2010.
- [39] Hirschfelder, J. O., Curtiss, C. F., Bird, R. B., and Mayer, M. G., *Molecular theory of gases and liquids*, Vol. 165. New York: Wiley, 1964.
- [40] Ihme, M., Cha, C. M. and Pitsch, H., "Prediction of local extinction and re-ignition effects in non-premixed turbulent combustion using a flamelet/progress variable approach". In: *Proceedings of the Combustion Institute*, 30.1, 793-800, 2005.
- [41] Jameson, A., "Analysis and design of numerical schemes for gas dynamics, 1: artificial diffusion, upwind biasing, limiters and their effect on accuracy and multigrid convergence". In: *International Journal of Computational Fluid Dynamics*, 4.3-4, 171-218, 1995.
- [42] Janicka, J., Kolbe, W. and Kollmann, W., "Closure of the transport equation for the probability density function of turbulent scalar fields". In: *Journal of Non-Equilibrium Thermodynamics*, 4.1, 47-66, 1979.
- [43] Jenny, P., Pope, S. B., Muradoglu, M., and Caughey, D. A., "A hybrid algorithm for the joint PDF equation of turbulent reactive flows". In: *Journal of Computational Physics*, 166.2, 218-252, 2001.

- [44] Jones, W. P. and Prasad, V. N., "Large Eddy Simulation of the Sandia Flame Series (D–F) using the Eulerian stochastic field method". In: *Combustion and Flame*, 157.9, 1621-1636, 2010.
- [45] Karpetsis, A. N. and Barlow, R. S., "Measurements of flame orientation and scalar dissipation in turbulent partially premixed methane flames". In: *Proceedings of the Combustion Institute*, 30.1, 665-672, 2005.
- [46] Klimenko, A.Y. and Pope, S.B., "The modeling of turbulent reactive flows based on multiple mapping conditioning". In: *Physics of Fluids*, 15.7, 1907-1925, 2003.
- [47] Kronenburg, A. and Papoutsakis, A.E., "Conditional moment closure modeling of extinction and re-ignition in turbulent non-premixed flames". In: *Proceeding of the Combustion Institute*, 30, 759-766, 2005.
- [48] Battin-Leclerc, F., Simmie, J. M., and Blurock, E. *Cleaner combustion. Developing Detailed Chemical Kinetic Models. Series: Green Energy and Technology*. London: Springer Verlag, 2013.
- [49] Lipp, S., *Numerische Simulation turbulenter reaktiver Strömungen mit einem hybriden CFD/transported PDF Modell*. Dissertation. Karlsruhe, Karlsruhe Institut für Technologie (KIT), KIT Scientific Publishing, 2014.
- [50] Lu, T., and Law, C. K., "A directed relation graph method for mechanism reduction". In: *Proceedings of the Combustion Institute*, 30.1, 1333-1341, 2005.
- [51] Maas, U. and Pope, S.B., "Simplifying chemical kinetics: intrinsic low-dimensional manifolds in composition space". In: *Combustion and Flame*, 88.3, 239-264, 1992.
- [52] Maas, U. and Pope, S.B., "Implementation of simplified chemical kinetics based on intrinsic low-dimensional manifolds". In: *Symposium (International) on Combustion*, in Australia, 24.1, 103-112, 1992.
- [53] Maas, U. and Pope, S.B., "Laminar flame calculations using simplified chemical kinetics based on intrinsic low-dimensional manifolds". In: *Symposium (International) on Combustion*, in United States, 25.1, 1349-1356, 1994.

BIBLIOGRAPHY

- [54] Maas, U., "Efficient calculation of intrinsic low-dimensional manifolds for the simplification of chemical kinetics". In: *Computing and Visualization in Science*, 1.2, 69-81, 1998.
- [55] Maas, U., and Thevenin, D., "Correlation analysis of direct numerical simulation data of turbulent non-premixed flames". In: *Symposium (International) on Combustion*, in United States, 27.1, 1183-1189, 1998.
- [56] Maas, U., and Bykov, V., "The extension of the reaction/diffusion manifold concept to systems with detailed transport models". In: *Proceedings of the Combustion Institute*, 33.1, 1253-1259, 2011.
- [57] Maas, U. and Tomlin, A.S., "Time-scale splitting-based mechanism reduction." In: *Cleaner Combustion*, 467-484, London: Springer 2013.
- [58] Matsunuma, T., "Effects of Reynolds number and freestream turbulence on turbine tip clearance flow". In: *ASME. Journal of Turbomachinery*, 128.1, 166-177, 2006.
- [59] Magagnato, F., "KAPPA - Karlsruhe parallel program for aerodynamics". In: *TASK Quarterly 2*, 215-270, 1998.
- [60] Mehl, M., Pitz, W.J., Westbrook, C.K., and Curran, H.J., "Kinetic Modeling of Gasoline Surrogate Components and Mixtures Under Engine Conditions". In: *Proceedings of the Combustion Institute*, 33, 193-200, 2011.
- [61] Minuzzi, F., Yu, C. and Maas, U., "Simulation of methane/air non-premixed turbulent flames based on REDIM simplified chemistry". In: *Flow, Turbulence and Combustion*, 103.4, 963-984, 2019.
- [62] Moukalled, F., Mangani, L. and Darwish, M., *The finite volume method in computational fluid dynamics*. Berlin, Germany: Springer, 2016.
- [63] Neagos, A. *Adaptive Generierung von Reaktions-Diffusions-Mannigfaltigkeiten fuer die reduzierte Beschreibung chemisch reagierender Strömungen*, Dissertation, Karlsruhe, Karlsruher Institut für Technologie (KIT), KIT Scientific Publishing, 2017.
- [64] Okafor, E. C., Hayakawa, A., Nagano, Y., and Kitagawa, T., "Effects of hydrogen concentration on premixed laminar flames of hydrogen-methane-air". In: *International Journal of Hydrogen Energy*, 39.5, 2409-2417, 2014.

- [65] Peters, N., "Laminar diffusion flamelet models in non-premixed turbulent combustion". In: *Progress in energy and combustion science*, 10.3, 319-339, 1984.
- [66] Peters, N. and Rogg, B., "Reduced kinetic mechanisms for applications in combustion systems". Vol. 15. Berlin, Heidelberg: Springer Science and Business Media, 2008.
- [67] Pierce, C. D. and Moin, P., "Progress-variable approach for large-eddy simulation of non-premixed turbulent combustion". In: *Journal of fluid Mechanics*, 504, 73-97, 2004.
- [68] Pitsch, H., "Unsteady flamelet modeling of differential diffusion in turbulent jet diffusion flames". In: *Combustion and Flame*, 123(3), 358-374, 2000.
- [69] Pitsch, H. and Steiner, H., "Large-eddy simulation of a turbulent piloted methane/air diffusion flame (Sandia flame D)". In: *Physics of fluids*, 12(10), 2541-2554, 2000.
- [70] Poinso, T., and Veynante, D. *Theoretical and numerical combustion*. Philadelphia: RT Edwards, Inc., 2005
- [71] Pope, S. B., "Computationally efficient implementation of combustion chemistry using in situ adaptive tabulation". In: *Combustion Theory and Modeling*, 1.1, 41-63, 1997.
- [72] Pope, S.B., *Turbulent Flows*. Cambridge: Cambridge University Press, 2001.
- [73] Pope, S.B., "PDF methods for turbulent reactive flows". In: *Progress in energy and combustion science*, 11.2, 119-192, 1985.
- [74] Porras, S., Bykov, V., Goldshtein, V. and Maas, U., "Joint characteristic timescales and entropy production analyses for model reduction of combustion systems". In: *Entropy*, 19.6, 264, 2017.
- [75] Press, W. H., Flannery, B. P., Teukolsky, S. A. and Vetterling, W. T., *Numerical recipes*, Vol. 3. Cambridge: Cambridge University Press, 1989.
- [76] Ramaekers, W. J. S., Van Oijen, J. A., and De Goey, L. P. H., "A priori testing of flamelet generated manifolds for turbulent partially premixed methane/air flames". In: *Flow, turbulence and combustion*, 84.3, 439-458, 2010.

BIBLIOGRAPHY

- [77] Rembold, B. and Jenny, P., "A multiblock joint pdf finite-volume hybrid algorithm for the computation of turbulent flows in complex geometries". In: *Journal of Computational Physics*, 220.1, 59-87, 2006.
- [78] Ren, Z.Y., Subramaniam, S. and Pope, S.B., "Implementation of the EMST mixing model." URL: <http://tcg.mae.cornell.edu/emst> (2002). accessed Mai 08, 2017.
- [79] Ren, Z.Y. and Pope, S.B., "Transport-chemistry coupling in the reduced description of reactive flows". In: *Combustion Theory and Modelling*, 11.5, 715-739, 2007.
- [80] Richardson, E. S., Granet, V. E., Eyssartier, A., and Chen, J. H., "Effects of equivalence ratio variation on lean, stratified methane-air laminar counterflow flames". In: *Combustion Theory and Modelling*, 14.6, 775-792, 2010.
- [81] Smith, G. P., Golden, D. M., Frenklach, M., Moriarty, N. W., Eiten-
eer, B., Goldenberg, M., ··· , and Lissianski, V. V., GRI-Mech 3.0. URL: <http://combustion.berkeley.edu/gri-mech/>, 1999. accessed Mai 22, 2016.
- [82] Smith, G. P., Tao, Y. and Wang, H., "Foundational fuel chemistry model version 1.0 (FFCM-1)". URL: <http://web.stanford.edu/group/haiwanglab/FFCM1/pages/FFCM1.html>, accessed July 12, 2019.
- [83] Skinner, Lindsay A. *Singular perturbation theory*. New York: Springer Science & Business Media, 2011.
- [84] Sheikhi, M.R.H., Drozda, T.G., Givi, P., Jaber, F.A. and Pope, S.B., "Large eddy simulation of a turbulent nonpremixed piloted methane jet flame (Sandia Flame D)". In: *Proceedings of the Combustion Institute*, 30.1, 549-5562, 2005.
- [85] Singh, S., Powers, J. M. and Paolucci, S., "On slow manifolds of chemically reactive systems". In: *The Journal of chemical physics*, 117.4, 1482-1496, 2002.
- [86] Spalding, D. B., "Mixing and chemical reaction in steady confined turbulent flames". In: *Symposium (International) on Combustion*, in United States, 13.1, 649-657, 1971.

- [87] Spalding, D.B., "Concentration fluctuations in a round free jet". In: *Chemical engineering sciences*, 26, 95-107, 1971.
- [88] Spalding, D. B., "Mathematical models of turbulent flames; a review". In: *Combustion Science and Technology*, 13.1-6, 3-25, 1976.
- [89] Steinhilber, G., *Numerische Simulation turbulenter Verbrennungsprozesse mittels statistischer Verfahren und REDIM reduzierter Kinetik*. Dissertation. Karlsruhe, Karlsruhe Institut für Technologie (KIT), KIT Scientific Publishing, 2015.
- [90] Strassacker, C., Bykov, V. and Maas, U., "Parametrization and projection strategies for manifold based reduced kinetic models". In: *Proceedings of the Combustion Institute*, 37.1, 763-770, 2019.
- [91] Subramaniam, S. and Pope, S.B., "A mixing model for turbulent reactive flows based on Euclidean minimum spanning trees". In: *Combustion and Flame*, 115.4, 487-514, 1998.
- [92] Sung, C. J., Law, C.K. and Chen, J-Y., "An augmented reduced mechanism for methane oxidation with comprehensive global parametric validation". In: *Symposium (International) on Combustion*, in United States, 27.1., 295-304, 1998.
- [93] Sung, C. J., Law, C. K. and Chen, J-Y., "Augmented reduced mechanisms for NO emission in methane oxidation". In: *Combustion and Flame*, 125.1-2, 906-919, 2001.
- [94] Tavoularis, S. and Corrsin, S., "Effects of shear on the turbulent diffusivity tensor". In: *International journal of heat and mass transfer*, 28.1, 265-276, 1985.
- [95] Turanyi, T. and Tomlin, A.S., *Analysis of kinetic reaction mechanisms*, Berlin: Springer Berlin Heidelberg, 2014.
- [96] Turns, S. R., *Introduction to combustion*, New York: McGraw-Hill Companies, 1996.
- [97] Van Oijen, J.A. and De Goey, L. P.H., "Modelling of premixed laminar flames using flamelet-generated manifolds". In: *Combustion Science and Technology*, 161.1, 113-137, 2000.

BIBLIOGRAPHY

- [98] Van Oijen, J. A. and De Goey, L. P. H., "Modelling of premixed counterflow flames using the flamelet-generated manifold method". In: *Combustion Theory and Modelling*, 6.3, 463-478, 2002.
- [99] Van Slooten, P. R., Jayesh, and Pope, S., "Advances in PDF modeling for inhomogeneous turbulent flows". In: *Physics of Fluids*, 10.1, 246-265, 1998.
- [100] Wang, H.F., and Chen, Y.L., "PDF modelling of turbulent non-premixed combustion with detailed chemistry". In: *Chemical engineering science*, 59.16, 3477-3490, 2004.
- [101] Wang, H.F. and Kim, K., "Effect of molecular transport on PDF modeling of turbulent non-premixed flames". In: *Proceedings of the Combustion Institute*, 35.2, 1137-1145, 2015.
- [102] Wang, H.F., "Consistent flamelet modeling of differential molecular diffusion for turbulent non-premixed flames". In: *Physics of Fluids*, 28.3, 035102, 2016.
- [103] Wang, P., Zieker, F., Schiessl, R., Platova, N., Froehlich, J. and Maas, U., "Large eddy simulations and experimental studies of turbulent premixed combustion near extinction". In: *Proceeding of the Combustion Institute*, 34.1, 1269-1280, 2013.
- [104] Warnatz, J., Maas, U. and Dibble, R. W., *Combustion: Physical and Chemical Fundamentals, Modeling and Simulation, Experiments, Pollutant Formation*, Berlin: Springer, 1996.
- [105] Wild, M. A., *General purpose PDF solution algorithm for reactive flow simulations in OpenFOAM*. Dissertation. ETH Zurich, 2013.
- [106] Williams, F. A., "Chemical-kinetic mechanisms for combustion applications. University of California, San Diego". URL: <http://maeweb.uscd.edu/combustion/cermech/>, accessed August 08, 2018.
- [107] Xu, J., and Pope, S.B., "PDF calculations of turbulent nonpremixed flames with local extinction". In: *Combustion and flame*, 123.3, 281-307, 2000.
- [108] Yang, Zhiyin, "Assessment of unsteady-RANS approach against steady-RANS approach for predicting twin impinging jets in a cross-flow". In: *Cogent Engineering*, 1.1, 936995, 2014.

- [109] Yu, C., Bykov, V. and Maas, U., "Global quasi-linearization (GQL) versus QSSA for a hydrogen–air auto-ignition problem". In: *Physical chemistry chemical physics*, 20.16, 10770-10779, 2018.
- [110] Yu, C., Minuzzi, F., Bykov, V., and Maas, U., "Methane/Air Auto-Ignition Based on Global Quasi-Linearization (GQL) and Directed Relation Graph (DRG): Implementation and Comparison". In: *Combustion Science and Technology*, 192.9, 1802-1824, 2020.
- [111] Yu, C., Bykov, V., and Maas, U., "Coupling of simplified chemistry with mixing processes in PDF simulations of turbulent flames". In: *Proceedings of the Combustion Institute*, 37.2, 2183-2190, 2019.
- [112] Yu, C., Minuzzi, F. and Maas, U., "REDIM reduced chemistry for the simulation of counterflow diffusion flames with oscillating strain rates". In: *Combustion Theory and Modelling*, 24.4, 682-704, 2020.
- [113] You, J., Yang, Y. and Pope, S.B., "Effects of molecular transport in LES/PDF of piloted turbulent dimethyl ether/air jet flames". In: *Combustion and Flame*, 176, 451-461, 2017.
- [114] Zhang, Y. Z., and Haworth, D.C., "A general mass consistency algorithm for hybrid particle/finite-volume PDF methods". In: *Journal of Computational Physics*, 194.1, 156-193, 2004.
- [115] Ren, Z., and Pope, S. B., "Transport-chemistry coupling in the reduced description of reactive flows". In: *Combustion Theory and Modelling*, 11.5, 715-739, 2007.

List of publications

Yu, C., Breda, P., Pfitzner, M. and Maas, U., 2020. Coupling of mixing models with manifold based simplified chemistry in PDF modeling of turbulent reacting flows. *Proceedings of the Combustion Institute*, accepted for publication. Online available, DOI: <https://doi.org/10.1016/j.proci.2020.06.132>.

Minuzzi, F., Yu, C. and Maas, U., 2020. Numerical simulation of laminar and turbulent methane/air flames based on a DRG-derived skeletal mechanism. *Eurasian Chemico-Technological Journal*, 22.2, pp. 69-80.

Yu, C., Minuzzi, F. and Maas, U., 2020. REDIM reduced chemistry for the simulation of counterflow diffusion flames with oscillating strain rates. *Combustion Theory and Modelling*, 24.4, pp.682-704.

Yu, C., Minuzzi, F., Bykov, V. and Maas, U., 2020. Methane/air auto-ignition based on global quasi-linearization (GQL) and directed relation graph (DRG): implementation and comparison. *Combustion Science and Technology*, 192.9, pp. 1802-1824.

Minuzzi, F., Yu, C. and Maas, U., 2019. Simulation of methane/air non-premixed turbulent flames based on REDIM simplified chemistry. *Flow, Turbulence and Combustion*, 103.4, pp.963-984.

Bykov, V., Yu, C., Gol'dshtein, V. and Maas, U., 2019. Model reduction and mechanism comparison of hydrogen/oxygen auto-ignition. *Proceedings of the Combustion Institute*, 37.1, pp.781-787.

Yu, C., Bykov, V. and Maas, U., 2019. Coupling of simplified chemistry with mixing processes in PDF simulations of turbulent flames. *Proceedings of the Combustion Institute*, 37.2, pp.2183-2190.

Koksharov, A., Yu, C., Bykov, V., Maas, U., Pfeifle, M. and Olzmann, M., 2018. Quasi-Spectral Method for the Solution of the Master Equation for

BIBLIOGRAPHY

Unimolecular Reaction Systems. *International Journal of Chemical Kinetics*, 50.5, pp.357-369.

Yu, C., Minuzzi, F. and Mass, U., 2018. Numerical simulation of turbulent flames based on a hybrid RANS/Transported-PDF method and REDIM method. *Eurasian Chemico-Technological Journal*, 20.1, pp.23-31.

Yu, C., Bykov, V. and Maas, U., 2018. Global quasi-linearization (GQL) versus QSSA for a hydrogen–air auto-ignition problem. *Physical chemistry chemical physics*, 20.16, pp.10770-10779.

List of Acronyms

CMC	Conditional Mapping Closure
CFD	Computational Fluid Dynamic
DAE	Differential Algebraic Equations
DNS	Direct Numerical Simulation
DRG	Directed Relation Graph
EBU	Eddy Break-up
EDC	Eddy Dissipation Concept
EMST	Euclidean Minimum Spanning Trees
FGM	Flamelet Generated Manifold
FPI	Flame Prolongation ILDM
FPV	Flamelet/progress variable
FVM	Finite Volume Method
GQL	Global Quasi-linearization
IEM	Interaction by Exchange with the Mean
ILDM	Intrinsic Low-Dimensional Manifold
ISAT	In-situ Adaptive Tabulation
LES	Large Eddy Simulation
MCM	Modified Curl's Model
MIM	Method of Invariant Manifold
MMC	Multiple Mapping Conditioning
ODE	Ordinary Differential Equation
PaSR	Partially Stirred Reactor
PDE	Partial Differential Equation
PDF	Probability Density Function
PEA	Partial Equilibrium Approximation
QSSA	Quasi-steady State Approximation
RANS	Reynolds-averaged Navier-Stokes
REDIM	Reaction-Diffusion Manifolds
SDE	Stochastic Differential Equation
SLIP	Symmetric Limited Positive
SLM	Simplified Langevin Model
SLFM	Steady Laminar Flamelet Model